Journal of Applied Physics

PERSPECTIVE | AUGUST 13 2025

Perspectives of active Si photonics devices for data communication and optical sensing

Xiaoxin Wang ; Tianshu Li ; Juejun Hu ; Jifeng Liu

J. Appl. Phys. 138, 060901 (2025)
https://doi.org/10.1063/5.0263644
CHORUS

AIP Publishing

Journal of Applied Physics PERSPECTIVE pubs.aip.org/aip/jap

Perspectives of active Si photonics devices for data communication and optical sensing

Cite as: J. Appl. Phys. 138, 060901 (2025); doi: 10.1063/5.0263644
Submitted: 5 February 2025 · Accepted: 18 July 2025 ·
Published Online: 13 August 2025

Xiaoxin Wang,[1,a)] Tianshu Li,[2] Juejun Hu,[3] and Jifeng Liu[1,a)]

AFFILIATIONS

[1]Thayer School of Engineering, Dartmouth College, Hanover, New Hampshire 03755, USA
[2]Department of Civil Engineering, George Washington University, Washington, DC 20052, USA
[3]Department of Materials Science and Engineering, Massachusetts Institute of Technology, Cambridge, Massachusetts 02139, USA

[a)]**Authors to whom correspondence should be addressed:** Xiaoxin.Wang@Dartmout.edu and Jifeng.Liu@Dartmouth.edu

ABSTRACT

Si photonics has made rapid progress in research and commercialization in the past two decades. While it started with electronic–photonic integration on Si to overcome the interconnect bottleneck in data communications, Si photonics has now greatly expanded into optical sensing, light detection and ranging (LiDAR), optical computing, and microwave/RF photonics applications. From an applied physics point of view, this perspective discusses novel materials and integration schemes of active Si photonics devices for a broad range of applications in data communications, spectrally extended complementary metal–oxide–semiconductor (CMOS) image sensing, as well as 3D imaging for LiDAR systems. We also present a brief outlook of future synergy between Si photonic integrated circuits and Si CMOS image sensors toward ultrahigh capacity optical I/O, ultrafast imaging systems, and ultrahigh sensitivity lab-on-chip molecular biosensing.

I. INTRODUCTION

Si photonics is a disruptive technology that synergistically integrates the advantages of photons in communication and sensing with those of electrons in data processing. Leveraging the mature complementary metal–oxide–semiconductor (CMOS) technology, silicon photonics is an attractive and highly scalable solution to the interconnect bottleneck[1] in order to achieve functionality extension beyond Moore's law. Analogous to electronic integrated circuits (ICs), Si photonic integrated circuits (PICs) comprise a variety of building blocks on a single chip to achieve complex functions, including photon generation, modulation, routing/switching, filtering, detection, and processing. From its inception, a wealth of innovations in Si photonic devices have made their debut, such as high refractive index single-crystal Si waveguides,[2] tensile-strain-enhanced[3]/waveguide-integrated Ge/Si photodiodes,[4] Ge/Si avalanche photodiodes,[5] high-speed Si free-carrier modulator[6] and GeSi electroabsorption modulators (EAMs),[7] heterogeneously integrated III–V quantum well (QW)[8] and monolithic quantum dot (QD) lasers on Si,[9] and monolithic band-engineered Ge[10–12] and GeSn lasers on Si.[13,14] The key performance milestones of passive photonic devices [waveguides, splitters, couplers, (de)multiplexers], active photonic devices (lasers, modulators, and detectors), and system integration for Si PIC have been reviewed recently.[15] Mature Si photonics components, such as silicon-on-insulator (SOI) and silicon nitride waveguides, high-speed Si modulator, and Ge-on-Si photodetectors (PDs), have already been included in the process design kits (PDKs) of photonics foundries exemplified by the American Institute for Manufacturing Photonics (AIM Photonics)[16] and Interuniversity Micro-Electronics Center (IMEC),[17] the latter also incorporating GeSi EAMs. The trend of fabless Si photonics enables an emerging ecosystem with PDKs, testing equipment, and foundries.[18] In a similar fashion to electronics, shuttle-based multi-project wafer (MPW) services entitle designers to share the same mask and fabrication process, and cost, which facilitates proof-of-concept research and rapid shift from research prototype to product development.[18]

The innovation and breakthrough in Si photonics also sped up its successful commercialization. In 2014, Acacia demonstrated the first coherent Si transceiver for long haul.[19] Intel debuted its 100 G pluggable transceivers up to 10 km in 2016, 400 G (4 × 100 G) transceivers in 2020,[20] and a 224 Gb/s per channel optical sub-system in 2023 toward 800 G Data center Reach 4-lane (DR4).[21] In 2024, Intel further demonstrated the first optical

compute interconnect (OCI) co-packaged with CPU with bidirectional 4 Tbps data communication capability.[22] This was implemented using eight on-chip lasers in the O-band for wavelength division multiplexing (WDM), each carrying eight channels at 64 Gb/s data rate. In recent years, Si PICs have also been extending to other important applications. For example, Si-based phase shifters and antennas have been applied to optical phase arrays (OPAs) for beam steering without moving parts,[23] leading to prototype frequency-modulated continuous wave (FMCW) light detection and ranging (LiDAR) systems at eye-safe 1550 nm wavelength being commercialized by Analog Photonics, Inc.[24] The same platform has also been applied to optical computing, including quantum computing.

In parallel, fundamental research has been focusing on novel materials and device-level technologies for emerging applications. Si photonics is now broadly referred as PICs on Si platform regardless of materials or integration methods. Recent advances in the active devices aim at a higher performance level, i.e., higher speed and efficiency at lower loss and power consumption. Therefore, the scope of Si photonics is already far beyond monolithic integration based on group IV elements (Si, Ge, and Sn) or CMOS dielectrics (e.g., SiO_2 and Si_3N_4). It has been extended to oxides, e.g., transparent conductive oxides (TCOs), $LiNbO_3$ (LN), $BaTiO_3$ (BTO), and 2D materials (e.g., graphene) for photonic modulation as well as heterogeneous integration with III–V compounds for lasers and semiconductor optical amplifiers. The wavelengths of interest also extend from ~1310/1550 nm used in data communication and telecommunication to short-wave infrared (SWIR) and mid-wave infrared (MWIR) range for optical spectral and image sensing. Another trend is the integration of nonlinear optical (NLO) components. For example, Si_3N_4 NLO platform is emerging thanks to the low loss at high-power density, which allows on-chip frequency comb generation for WDM.[25] The combination of Si_3N_4 on SOI platform can also benefit from the relatively large refractive index contrast and small device footprint of SOI.[18,26] Active material platforms are also utilized to ensure high film crystallinity and good device performance, such as Ge on insulator (GeOI), GeSn on insulator (GeSnOI),[27,28] and thin film LN (TFLN) on insulator (TFLNOI).[29] Therefore, Si photonics technology is tremendously expanding its library of materials, devices, standard design rules and integration approaches, which will speed up the development of Si PICs for various applications in the next decade, such as photonic computing,[30,31] optical sensing,[32] and integrated microwave photonics for wireless communication and photonics-enhanced radar sensing.[33]

The aim of this Perspective is to provide an assessment and new visions toward emerging active photonic device technologies for Si PICs, especially from an applied physics point of view. In Sec. II, we will start with recent progress in enriching active photonic materials and integration schemes for Si PICs, which can greatly enhance the device performance and bring in new functionalities. In Sec. III, we will discuss recent progress and emerging trends in active Si photonics devices, including lasers, modulators, photodetectors, and image sensors. The challenges and visions of future Si photonics technologies will also be discussed. In Sec. IV, we will present a brief outlook on the future synergy between Si CMOS image sensors (CIS) and Si PICs that could mutually benefit the development of each other. We then project a roadmap of Si active photonic devices in Sec. V before concluding this Perspective in Sec. VI.

II. ENRICHING ACTIVE PHOTONIC MATERIALS AND INTEGRATION SCHEMES FOR Si PICS

This section will discuss recent progress and discoveries in active photonic materials and integration schemes for Si PICs. In Sec. II A, we will focus on atomic ordering as a newly discovered physical mechanism and degree of freedom to engineer the band structures of SiGeSn alloys on Si for short-wave and mid-wave infrared (SWIR and MWIR) photonic sensing and LiDAR applications. Other novel materials platform, such as TCOs, BTOs, AlN, thin film LN, and InAs quantum dots (QDs), will be discussed later in Sec. III under modulators and laser sections. Section II B will present new back-end-of-line (BEOL) processing schemes to better incorporate emerging active photonic materials into Si PICs toward high-volume photonic manufacturing.

A. Emerging active photonic materials for SWIR/MWIR Si photonics

In the past two decades, epitaxial Ge/Si photodetectors have become a standard component in Si PIC.[16,17] As a natural extension, in recent years, GeSn and SiGeSn materials and devices have been investigated toward monolithic SWIR/MWIR photonics on Si. Two major motivations are: (1) transformation into direct gap semiconductors with significantly enhanced optoelectronic properties and (2) bandgap shrinkage for spectral extension into the SWIR and MWIR regimes for imaging and optical spectral sensing. While electrically pumped GeSn lasers[14,34–36] and Franz–Keldysh (FK) electro-absorption effect[37] have been demonstrated in recent years, a key limiting factor is the lack of lattice-matched heterostructures with sufficient band offset (>0.1 eV) to effectively confine the carriers up to room temperature, in contrast to their high-performance III–V counterparts. This issue severely limits the performance of SiGeSn/GeSn quantum well (QW) lasers and quantum-confined Stark effect (QCSE) electro-absorption modulators. For example, the barrier heights in the GeSn QW lasers[14,35,36] were too small to confine carriers effectively, limiting the operation temperature to <150 K so far. Therefore, new physical mechanisms are needed to achieve a large band offset under the constraint of lattice matching in SiGeSn systems.

To realize lattice-matched heterostructures/QWs for high-performance SiGeSn SWIR/MWIR active photonic devices, engineering atomic short-range order (SRO) in SiGeSn has recently emerged as a new degree of freedom for band engineering, beyond chemical composition and strain. Atomic SRO refers to the preference or avoidance of neighboring atomic species, especially in the first, second, and third nearest neighbor (1NN, 2NN, and 3NN) shells. For example, a Sn atom may prefer to have a Ge atom as its first nearest neighbor rather than another Sn atom in order to minimize the local lattice distortion. This is in contrast to random alloys, where all the atoms distribute randomly on the lattice sites without any preference of neighboring atomic species. SRO in GeSn was first discovered in 2020 through first-principles computational modeling,[38] where Sn–Sn 1NN was considered energetically

unfavorable due to the large local lattice distortion induced by Sn atoms (~15% larger than Ge atoms). Consequently, Sn–Sn 1NN is strongly depleted in more thermodynamically stable SRO GeSn alloys compared to random alloys, while Sn–Sn 3NN is strongly enhanced correspondingly. Effectively, Sn–Sn 1NN are "repelled" to the 3NN shells in order to minimize the local strain induced by Sn atoms. This factor induces a notable difference between the bandgaps of SRO vs random GeSn alloys as the Sn composition increases above 15 at. %. While the random alloy model predicts a vanishing bandgap in GeSn at ~22 at. % Sn, this semiconductor–semimetal transition has not occurred even at 35 at. % Sn when taking into account SRO,[38] which is consistent with the experimental results.[39]

Furthermore, first-principles theoretical modeling found even more significant impact of SRO on SiGeSn ternary alloys. Since Si atoms are ~4% smaller than Ge while Sn atoms are ~15% larger, the interplay between Si and Sn atoms leads to a more sophisticated SRO that compensates the lattice distortion induced by each other. Jin *et al.* found that two different types of SRO can co-exist in $Si_{0.125}Ge_{0.625}Sn_{0.25}$ alloys due to nearly identical Gibbs free energies, one called regular SRO (R-SRO) and the other called enhanced SRO (E-SRO), as shown in Fig. 1.[40] R-SRO predominantly features Sn–Sn 1NN repulsion similar to GeSn alloys [Fig. 1(a), left panels], as well as some degree of preference for Si–Si 1NN. This suggests the formation of Si–Si–Sn neighboring configurations to compensate the local strain. E-SRO, in contrast, is an even more ordered structure featuring strong repulsions between Sn–Sn, Si–Si, and Si–Sn 1NN and attraction between Ge–Sn and Ge–Si 1NN [Fig. 1(a), right panels], indicating a dominance of Si–Ge–Sn neighboring configuration to dissipate the strain induced by the large Sn atoms. While E-SRO is slightly more effective in reducing the lattice distortion induced by Sn atoms than R-SRO, it also has lower configuration entropy due to more ordered motifs. Therefore, overall their Gibbs free energies are almost degenerate, leading to their coexistence.

Strikingly, such differences in atomic SRO can lead to dramatically different bandgaps of the same SiGeSn alloy composition [Fig. 1(b)]. For example, the modeled bandgaps for the identical composition of random, R-SRO, and E-SRO $Si_{0.125}Ge_{0.625}Sn_{0.25}$ alloys are 0.25 eV (direct), 0.5 eV (direct), and 0.75 eV (indirect), respectively, differing by as much as three times.[40] These results further suggest that lattice-matched SiGeSn heterostructures/QWs with large band offset could potentially be implemented based on differences in SRO rather than composition, offering a new degree of freedom for band engineering. These lattice-matched SRO heterostructures have been modeled very recently by Jin *et al.*[41] Figure 2 shows a few examples. In particular, E-SRO and random $Si_{0.125}Ge_{0.625}Sn_{0.25}$ alloys form a type-I heterostructure with

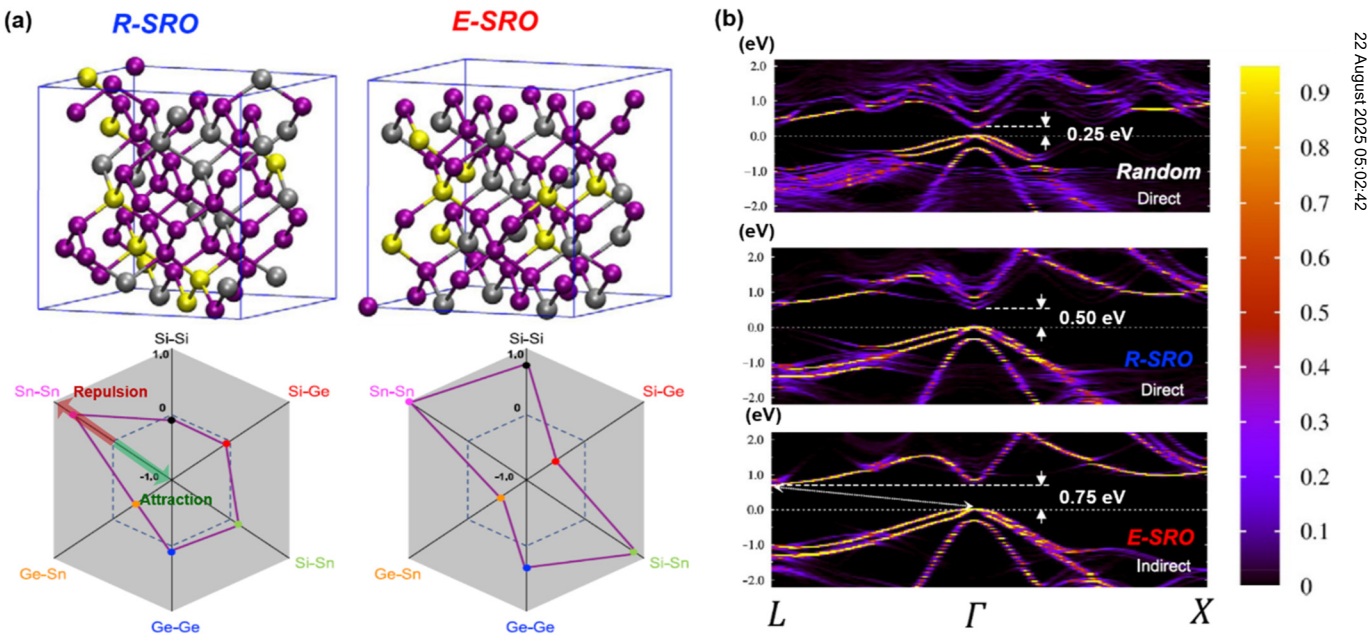

FIG. 1. (a) Atomic configurations of exemplary R-SRO and E-SRO $Si_{0.125}Ge_{0.625}Sn_{0.25}$ supercells from Monte Carlo sampling upon energy minimization. Si, Ge, and Sn atoms are represented by yellow, purple, and silver, respectively. The corresponding SRO polygons (lower panels) show the average Warren–Cowley SRO parameters of different atomic pairs, defined as $(1 - P_{AB}^{KNN})/x_B$, where P_{AB}^{KNN} is the occupation probability of B atoms in A atoms' KNN shells, and x_B is the composition of B in the alloy. The dashed-line hexagon indicates the Warren–Cowley SRO parameters of random alloys. Data points within the hexagons indicate attraction/preference of the corresponding atomic pairs as 1NN, while those outside the dashed-line hexagon indicate repulsion/avoidance. (b) The corresponding band structures of random, R-SRO, and E-SRO $Si_{0.125}Ge_{0.625}Sn_{0.25}$ alloys. The color bar indicates the Bloch spectral weight. Adapted with permission from Xiaochen Jin, Shunda Chen, and Tianshu Li, Commun. Mater **3**, 66 (2022). Copyright 2022 Author(s), licensed under a Creative Commons Attribution (CC BY) license.

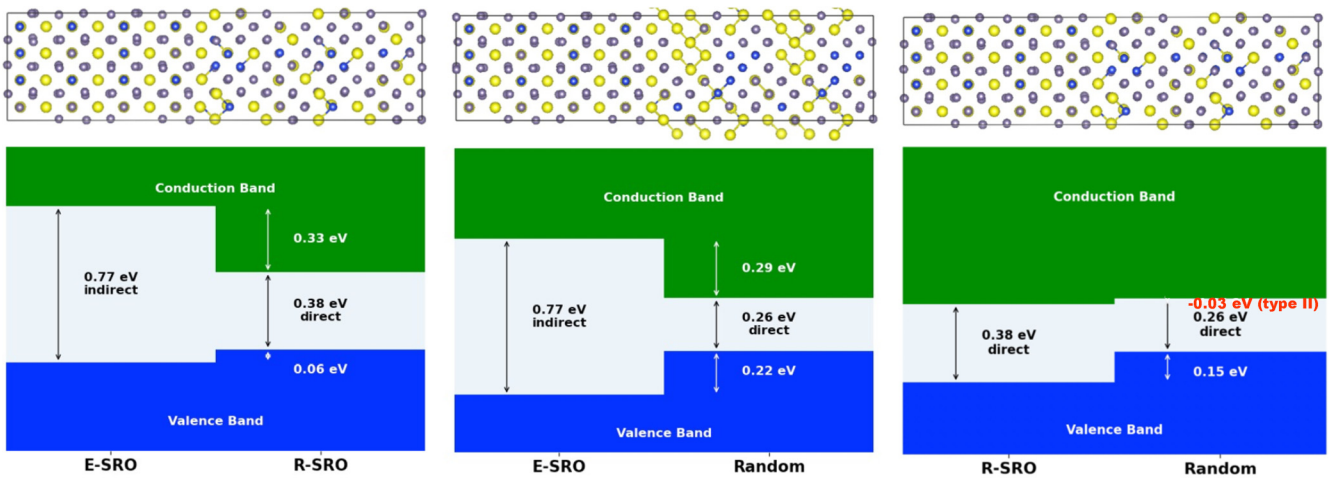

FIG. 2. Calculated band offsets in lattice-matched, iso-compositional $Si_{0.125}Ge_{0.625}Sn_{0.25}$ SRO heterostructures based on differences in atomic ordering from first-principles modeling. The gray, blue, and yellow atoms represent Ge, Si, and Sn, respectively. Heterojunctions between enhanced short-range order (E-SRO) and regular SRO (R-SRO) and E-SRO/Random lead to type I band alignment, where the bandoffsets are >0.2 eV for both the conduction and valence bands in the latter case. By comparison, R-SRO/random yields Type-II heterojunctions.

>0.2 eV band offset in both conduction and valence bands. Other E-SRO and SRO supercells show tunable Type I band offsets between 0.1 and 0.3 eV,[41] similar to the case of AlGaAs/GaAs QWs for high-performance electrically pumped lasers at room temperature. This will be further discussed in Sec. III.

Experimentally, SRO in GeSn has been verified through two independent extended x-ray absorption fine structure (EXAFS) studies. Lenz *et al.* studied Sn–Sn SRO in GeSn nanowires (NWs) with ~10 at. % Sn and found that the occurrence of Sn–Sn 1NN is only ~60% that of random alloys.[42] Independently, we investigated the EXAFS data of nearly relaxed 800 nm-thick GeSn thin films grown by chemical vapor deposition (CVD)[43] with ~18 at. % Sn composition. We found that fitting the experimental EXAFS data in Fig. 3(a) essentially does not need to include Sn–Sn 1NN scattering paths. Therefore, we reached a small average Sn–Sn 1NN coordination number (C.N.) of 0.08 [Fig. 3(b)], in good agreement with the theoretical value of 0.10 for SRO GeSn with 18.75 at. % Sn.[38] Even the upper limit of Sn–Sn 1NN C.N. of 0.26 from the EXAFS data fitting is still much lower than that of the random GeSn alloy of the same composition, i.e., 4 1NN in diamond cubic structure times 18% probability of having a Sn atom in the 1NN shell for random alloys = 0.72. This result strongly supports the theoretical prediction of SRO in GeSn: Sn–Sn 1NN is unfavorable thermodynamically due to the large local lattice distortion. For SiGeSn alloys, very recent analyses of atom probe tomography (APT) experimental data using a physics informed Poisson-Kth Nearest Neighbor (KNN) statistical method[44] have also confirmed the theoretically predicted SRO in SiGeSn with a clear preference of Si–Si 1NNs.[45] The Si–Si 1NN SRO parameters also quantitatively agree with the theoretical predictions after considering the atomic position perturbations in practical APT measurements induced by laser pulse and electric field evaporation of the atoms. Furthermore, the SiGeSn atomic SRO is supported by four-dimensional scanning transmission electron microscopy (4D-STEM) studies, showing energy-filtered diffuse diffraction patterns highly consistent with theoretically modeled SiGeSn supercells featuring Si–Ge–Sn motifs.[46,47]

In terms of further controlling the SRO in (Si)GeSn alloys toward implementing lattice-matched iso-compositional SiGeSn SRO heterostructures and QWs shown in Fig. 2, our recent studies have identified two feasible approaches for *in situ* and *ex situ* control, respectively:

(1) *In situ* control during the epitaxial growth by engineering surface chemistry[45] and/or surface termination.[48] This approach helps us to implement SRO heterostructures in the growth direction, i.e., normal to the surface. For example, we found that SiH_2Cl_2 precursor in CVD growth leads to a stronger preference of Si–Si 1NN than Si_2H_6 precursor in SiGeSn alloys.[45] Considering that R-SRO exhibits some preference of Si–Si 1NN while E-SRO exhibits repulsion, as discussed earlier, these preliminary results imply that SiH_2Cl_2 might favor R-SRO while Si_2H_6 may favor E-SRO. Indeed, recent Raman studies on the latter case also suggest strong depletion of Sn–Sn and Si–Sn 1NN that are consistent with the features of E-SRO.[49] Further considering that we also have several choices for Ge and Sn precursors in SiGeSn CVD process, SRO in SiGeSn can potentially be controlled conveniently by switching growth precursors to modify the band structure while maintaining the same composition and lattice constant, thereby achieving lattice-matched SRO heterostructures and QWs modeled in Fig. 2. Across different growth methods, we also found that GeSn thin films grown by molecular beam epitaxy (MBE) have a stronger preference for Sn–Sn 1NN than their CVD counterparts of similar composition.[48] First-principles

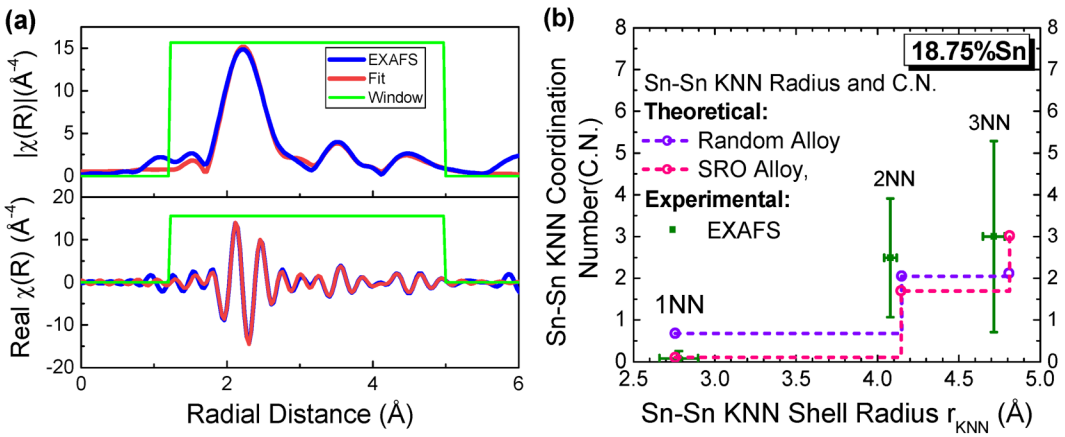

FIG. 3. (a) An example of fitting the Fourier transform of EXAFS data on Sn K-edges, including the magnitude (upper panel) and the real part of the x-ray absorption fine structure parameter χ (lower panel). (b) Comparison between experimentally measured (from EXAFS fitting) and theoretically modeled Sn–Sn 1NN, 2NN, and 3NN coordination number (C.N.) vs shell radius. The depletion of 1NN from EXAFS is a strong evidence of SRO in epitaxial GeSn thin films.

computational modeling shows that this is likely due to the atomic H surface termination in CVD vs surface reconstruction under ultrahigh vacuum in MBE. This fundamental difference in surface termination modifies the formation energy of Sn–Sn 1NN at the growth front, where H surface termination increases the formation energy of Sn–Sn 1NN by ∼35 meV, thereby suppressing Sn–Sn 1NN at the growth front. Interestingly, atomic H termination has been reported in SiGe alloys growth to induce Si surface clustering,[50] opposite to the impact on Sn–Sn 1NN observed in this case. Therefore, engineering surfactants during the growth could provide another possible approach for *in situ* SRO control especially for MBE SiGeSn.

(2) *Ex situ* control via ion beam modification. This approach helps us to further implement SRO heterostructures in the lateral direction. Recently, Vogl *et al.*[46] have discovered that He^+ radiation on the order of tens of keV could be utilized to modify atomic SRO in SiGeSn alloys without introducing crystallographic defects. Due to the small mass of He^+ ions, most of them simply pass through the SiGeSn thin film without strong interaction. Only a small fraction (<10%) of He^+ ions transiently create atomic recoils or vacancies, which allows atoms to swap positions with their nearest neighbors and thus modify the SRO. Depending on the dose of the He^+ ions, the SRO in SiGeSn can be reduced or even enhanced based on the corresponding diffuse diffraction patterns in *in situ* 4D-STEM analyses. Combined with nanolithography, this approach offers the flexibility of implementing lateral SRO QWs wherever needed, or combined with vertical heterostructures to define nanowires.

Interestingly, these *in situ* and *ex situ* SRO control methods are very much analogous to the case of implementing doping profiles in semiconductor devices, where *in situ* doping during the growth and *ex situ* doping via ion implantation are both applied to achieve sophisticated device structures. Therefore, further developing these SRO control methods will establish a complete toolset toward SRO-based band engineering not only in the vertical growth direction but also lateral directions, offering new degrees of freedom for designing and fabricating high-performance SiGeSn SWIR and MWIR active integrated photonic devices.

Beyond SRO engineering in (Si)GeSn alloys, very recent first-principles computational modeling by Liang *et al.*[51] also discovered that more drastic band engineering could be implemented using GeSn digital alloys (Das) incorporating Sn mono/bilayers, potentially decreasing the direct bandgap all the way down to a few meV at an average Sn composition <10 at. % to cover the entire IR spectrum. Note that these structures are different from commonly used III–V superlattices[52] and digital alloys[53] for avalanche photodiodes in that they embed Sn atoms into (111) atomic bilayers with a thickness of $\sim \left(\frac{\sqrt{3}}{12}\right)a$, where a is the lattice constant (see Fig. 4). Therefore, we call it "δ digital alloy" (δ-DA) and label them as $Ge_nSn_1(111)$, indicating superlattices comprising repeating units of n atomic layers of Ge and 1 atomic layer of Sn along the [111] direction. While conventional DAs are mostly short-period superlattices engineering the envelope wavefunction, δ-DA directly modifies the atomic orbitals between nearest neighbors, thereby enabling a more dramatic modification of the band structure inaccessible to conventional DAs.

Due to the significantly larger atomic size of Sn, in addition to the local dilation of the lattice induced by the Sn monolayer, the lattice relaxation also leads to an elongation along the vertical [111] growth direction (since the top surface is free to expand) and a lateral contraction on the (111) plane compared to a perfect diamond cubic structure. This type of lattice distortion induced by the Sn monolayer not only reduces the bandgap but also enhances the inversion between the conduction and valence bands. The direct bandgap is decreased to 2 meV at n = 11, while regular GeSn alloys at the same composition (i.e., 8.3% Sn) would be a semiconductor with a direct gap of ∼0.55 eV.[38,54] Theoretical modeling also shows that intermixing of Ge and Sn atoms within each bilayer would further decrease the bandgap due to formation of Sn–Sn

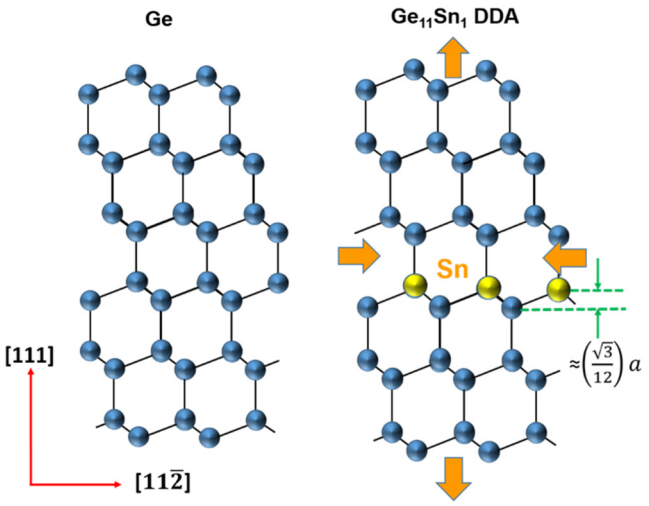

FIG. 4. Schematics showing the lattice distortion induced by a Sn monolayer in GeSn δ digital alloys (δ-DAs).

1NN that enlarges the lattice distortion. This comparison indicates that concentrating the Sn atoms into a 2D mono/bilayer induces a much larger impact on the band structure than randomly dispersing them into the lattice of GeSn alloys. It offers a highly effective approach to tune the bandgap of GeSn from 0.55 eV to 2 meV by controlling atomic ordering, without changing the chemical composition or inducing further lattice mismatch, to cover the entire IR spectral regime. Further reducing n below 11 will lead to topological Dirac semimetals for integrated quantum materials and devices on Si.[51] For similar δ-DAs on (001) substrates, i.e., $Ge_nSn_1(100)$, the distortion of the tetrahedral diamond cubic structure is different, but notable bandgap shrinkage compared to random alloys is still predicted.

Interestingly, while Ge/Sn phase separation due to the solubility limit has been a concern for regular GeSn alloys, the δ-DA deliberately creates monolayer Sn phase separation. Within each Sn monolayer, Sn–Sn form 2NN instead of energetically unfavorable 1NN. Therefore, both factors help to stabilize the δ-DA for practical implementation. We also noted early efforts in growing $Ge_{20}Sn_2(001)$ superlattices by MBE in the early 1990s with bilayers of Sn atoms,[55] which can be refined and extended to grow these Ge_mSn_1 δ-DAs in future experimental studies.

To summarize this section, we envision that these new theoretical and experimental discoveries on (Si)GeSn SROs and Ge_mSn_1 δ-DAs will be promising to boost the performance of future SWIR/MWIR lasers, modulators, and photodetectors monolithically integrated on the Si platform for LiDAR and optical sensing applications.

B. Emerging BEOL processing for high-volume, active photonic device integration

So far, active photonic devices in Si PICs are mostly based on monolithically integrated Si and epitaxial Ge-on-Si materials (e.g., Si modulators and Ge photodetectors), as well as hybrid integrated III–V lasers. The former has limitations in optoelectronics properties and device performance, while the latter faces challenges in wafer-scale integration. As an example, for electro-optical (EO) modulators in RF integrated photonics, LN and BTO are far superior to Si in terms of insertion loss (IL), optical power density, and linearity of modulation, thanks to nearly zero two-photon absorption (TPA) at telecom wavelengths and the large linear EO coefficients (LEO, i.e., Pockels effect). However, these high-performance materials are difficult to integrate directly into Si CMOS processing flow in standard foundries due to exotic crystal structures (e.g., LN) or lattice match in heteroepitaxy (e.g., BTO). Furthermore, currently heteroepitaxy of Ge photodetectors requires high-temperature growth (650–750°C) on Si CMOS layer, which competes with transistors for real estate and complicates the fabrication process. Therefore, BEOL processing becomes an ideal approach to integrate these high-performance photonic materials above the electronics layers without perturbing standard CMOS processing. BEOL processed photonic layers may also lead to 3D photonic integration to boost the density and functionality of Si photonics. There are two emerging solutions for BEOL processing of active photonic devices, as summarized below.

1. High-throughput heterogeneous integration (HI)

Currently, parallel transfer of multiple III–V chips and wafer-scale HI on Si photonic platform are being investigated to enhance the throughput for high-volume photonic integration. Parallel transfer printing of multiple III–V coupons on Si using elastomer stamps has been reviewed recently in Ref. 56. Furthermore, we also note recent progress in "grafting" heterojunctions to address the lattice mismatch challenge for active photonic devices. A major difference of "grafting" from other HI techniques is that it forms III–V/tunneling oxide/Group IV abrupt heterojunctions with high-quality interfaces, rather than simply transferring III–V active devices on Si (Fig. 5).[57] The thin tunneling oxide, usually deposited by atomic layer deposition (ALD), not only enables BEOL low-temperature bonding process at <500 °C after layer transfer but also well passivates the surfaces of both III–V and group IV semiconductors.[58,59] The heterojunction diode performance is notably improved from direct heteroepitaxy or more conventional bonding methods for lattice mismatched systems. For example, p-Si/Al_2O_3/n-GaAs heterojunction diodes achieved an ideality factor of 1.07, a low dark current density of 10 nA/cm^2, and an on-off current ratio (+1 V vs −1 V) as high as 7.9×10^9, representing orders of magnitude improvements from previous surface-activated bonding[60] or direct heteroepitaxy of III–V on Si.[61] This approach potentially enables integrating the best of III–V and Si, e.g., high-performance avalanche photodiodes (APDs) based on III–V near infrared absorbers and Si multiplication layer with high-quality interfaces, compared to highly dislocated interfaces in the current Ge/Si APDs.

For wafer-scale HI approaches, we will discuss recent progress in wafer-scale HI of InAs QD lasers in Sec. III, which involves QD growth on 300 mm Si wafers. Another emerging wafer-scale photonic HI approach is the Substrate-inverted Multi-Material Integration Technology (SuMMIT),[62] which can integrate a large

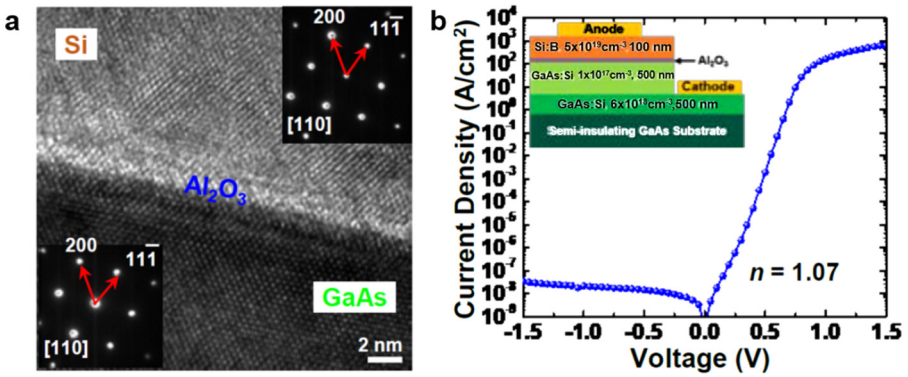

FIG. 5. (a) Cross-sectional high-resolution transmission electron microscopy (HRTEM) image and selected area diffraction patterns; (b) I–V characteristics at room temperature for a grafted p-Si/Al_2O_3/n-GaAs abrupt heterojunction diode. Reproduced with permission from Dong Liu, Sang June Cho, Jung-Hun Seo, Kwangeun Kim, Munho Kim, Jian Shi, Xin Yin, Wonsik Choi, Chen Zhang, Jisoo Kim, Mohadeseh A. Baboli, Jeongpil Park, Jihye Bong, In-Kyu Lee, Jiarui Gong, Solomon Mikael, Jae Ha Ryu, Parsian K. Mohseni, Xiuling Li, Shaoqin Gong, Xudong Wang, and Zhenqiang Ma, arXiv:1812.10225 (2018). Copyright 2018 Zhenqiang Ma.

variety of photonic materials on the Si platform. Similar to the concept of back-side illuminated (BSI) CMOS image sensors, the SuMMIT approach inverts a standard Si PIC wafer and bond its front side to the CMOS wafer using a direct-bond interconnect (DBI) wafer embedded with through-silicon/glass vias (TSVs/TGVs), as schematically shown in Fig. 6. The substrate of the Si PIC is then removed. This way, the photonic devices are exposed to the backside surface, similar to the manner Si pixels are exposed in BSI CMOS image sensors. Therefore, one could further process these photonic devices from the backside for BEOL HI of a variety of novel photonic materials such magneto-optical garnets for photonic isolators, electro-optical BTO and other oxides for modulators, GeSn for IR spectral extension, as well as phase change materials (PCMs) for photonic neuromorphic computing, etc. Local heating with resistive micro-heaters, which is already widely used in Si PICs for microring resonator and phase shifter tuning, can be conveniently adapted for thermal tuning of PCM, or further extended to crystallize magneto-optical/electro-optical materials without affecting devices nearby,[62] therefore compatible with BEOL processing. The concept of post-deposition thermal processing via on-chip micro-heaters to lower the global thermal budget of HI has recently been validated using garnet magneto-optical crystals as an example.[63] In addition, SuMMIT architecture can also leverage standard BEOL metal layers as back-reflectors to enhance optical coupling efficiency for grating couplers.

Furthermore, infrared semiconductors such as (Si)GeSn can be "retrofit" into Si modulators or Ge photodetector regions in the SuMMIT architecture. An example is shown in Figs. 6(b)–6(d). Here, the starting structure is a lateral Si p-n modulator with a Ge block grown on top. After PIC substrate removal, a trench is etched in the Si p-n junction and further into the Ge block. The etch depth is chosen to completely remove the initial Ge seed layer at the Ge–Si interface (~50 nm thick), which tends to contain more defects, leaving high-quality Ge as the virtual substrate. GeSn is then embedded into the trench either through MBE or CVD selective growth or Ge-templated crystallization via rapid thermal annealing (RTA), which will be further discussed in Sec. II B 2. Now the device can be turned into a SWIR photodetector or an EAM depending on the reverse bias. Figure 6(c) plots the modeled I–V curve of the device, with a dark current density of several mA/cm^2 at −1 V reverse bias. This is on the same order as epitaxial Ge/Si photodetectors and consistent with our previous work on crystallized p-GeSn/n-Si photodiodes.[27] Figure 6(d) further shows the band diagram at a small reverse bias of −1 V. Here, we assume a residual hole density of 10^{17} cm^{-3} in GeSn due to point defects, a realistic condition based on existing studies. Despite not having a truly intrinsic GeSn region, we can see that the GeSn region gets depleted from the p-GeSn/n-Si interface. There is a narrow barrier at the p^+-Si/p-GeSn interface, which can be tunneled through under reverse bias. Therefore, the device structure is suitable for waveguide-coupled photodetector or Franz–Keldysh modulator in SWIR regime for integrated photonic sensing applications.

2. Monolithic BEOL integration through low-temperature epitaxy or crystallization

In terms of BEOL monolithic integration, current work mostly focuses on Ge/Si photodetectors, especially low-temperature (<450 °C), high-quality Ge/Si epitaxy to accommodate BEOL thermal budget. Using a gradient p-doped epitaxial Ge layer on p-Si/n^+-Si grown by CVD at 400 °C, Marzen *et al.*[64] have achieved a very low dark current density of 0.27 mA/cm^2 and ~40% internal quantum efficiency at 1310 nm for surface-normal incidence Ge/Si photodetectors. It is expected that waveguide integration can significantly enhance the responsivity by increasing the optical absorption path length.[65] To minimize the real estate of the single-crystal Si CMOS layer needed for Ge epitaxy, we envision that this low-temperature growth approach can also potentially be combined with aspect ratio trapping (ART)[66–68] to further improve the material quality simultaneously, where treading dislocations are terminated within the ART channels.

Considering that the CVD growth temperature range of (Si)GeSn alloys is typically 250–350 °C, similar approaches can be

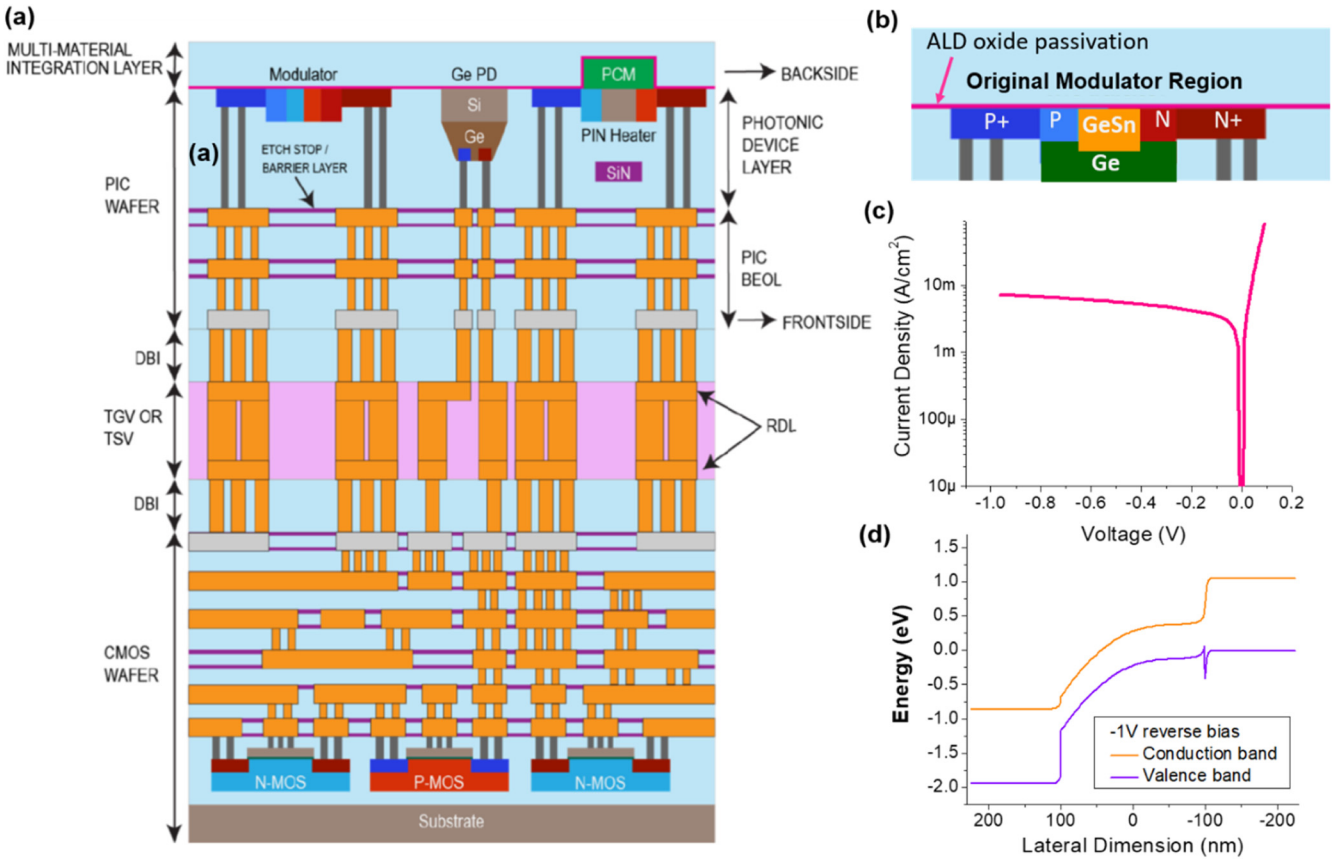

FIG. 6. (a) Schematics of SuMMIT architecture. Reproduced and slightly adapted with permission from Luigi Ranno, Jia Xu Brian Sia, Khoi Phuong Dao, and Juejun Hu, Opt. Mater. Express **13**, 2711–2725 (2023). Copyright 2023 Optica Publishing Group under the terms of the Optica Open Access Publishing Agreement. (b) Cross section of a GeSn integration architecture leveraging a Si modulator region as the template. (c) Modeled I–V curve of a lateral p+ Si/$Ge_{0.9}Sn_{0.1}$/n+ Si photodiode with a 200 nm wide GeSn region. (d) The corresponding energy diagram at −1 V reverse bias.

readily transferred to BEOL integration of (Si)GeSn SWIR/MWIR active photonic device integration on Si. Conventionally, GeSn has been grown on a high temperature annealed Ge buffer layer (>780 °C) to achieve good quality. With the most recent progress in Ref. 64, it is expected that both the Ge buffer and (Si)GeSn could be implemented at <450 °C compatible with the BEOL process. We also note that GeSn can be directly crystallized on Si using rapid thermal annealing at <450 °C,[27] or directly grown on Si using remote-plasma-enhanced CVD.[69] Further engineering atomic ordering in SiGeSn alloys and Ge_mSn_1 δ-DAs, as discussed in Sec. II A, will potentially allow us to implement full-spectral SWIR/MWIR/LWIR monolithic active photonic devices on Si using BEOL processing.

A limitation of epitaxial growth for scalable 3D photonic integration, though, is that it will be expensive and low throughput to repeat it multiple times to achieve multilayers of active photonic devices. It would be much more efficient if high crystallinity semiconductor photonic devices could be fabricated directly on interlayer dielectrics (ILDs) without epitaxy, just like passive photonic devices. McComber *et al.* first investigated BEOL growth of single-crystalline Ge on ILD using geometrically confined selective growth in a lateral channel etched into SiO_2 dielectrics, with a lithographically defined a-Si at one end of the channel as the seed for nucleation.[70] While multiple Ge nuclei may start to form on the a-Si seed initially, the one having the fastest growth ⟨110⟩ direction aligned with the channel will eventually prevail and leads to single-crystal Ge growth outside the channel. Metal–semiconductor–metal (MSM) Ge photodetectors have been fabricated based on this method for facile BEOL integration without the need for ion implantation and high-temperature activation annealing. A relatively low dark current density of 21 mA/cm^2 was demonstrated with >300% internal quantum efficiency under 980 nm illumination.[71] The exact gain mechanism is unclear in this case, but photoconductive gain and trapped carrier induced gain have been observed in other MSM systems.[72]

Interestingly, growing GeSn on ILD is actually more facile than Ge, thanks to the low eutectic temperature of the Ge–Sn binary system. We have demonstrated that co-evaporated amorphous

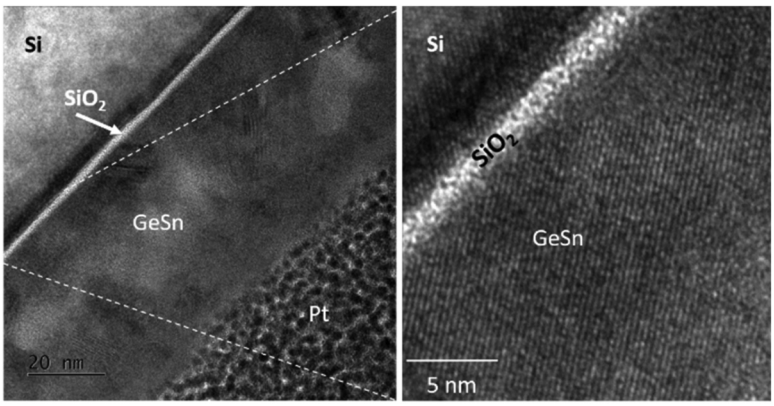

FIG. 7. Cross-sectional TEM images of $Ge_{0.74}Sn_{0.26}$ directly crystallized on a thin SiO_2 layer using the NICE method.

GeSn (a-GeSn) can be directly crystallized on SiO_2,[54,73] glass or even polyimide via RTA at <450 °C,[27] based on eutectically enhanced crystallization with large grain sizes on the order of tens to hundreds of μm.[73] Seeded by a nanotip in a tapered micropattern, which also facilitates optical coupling with waveguides, pseudo-single-crystalline GeSn can also be achieved on dielectrics. Furthermore, high Sn composition GeSn has been implemented on SiO_2 by dissolving Sn nanodots below the critical size of nucleation into the Ge matrix using a "nucleation reversal process." This method is called Sn nanodot induced composition enhancement (NICE).[27] As shown in the cross-sectional TEM image in Fig. 7, high crystallinity GeSn with clear lattice images is grown on a thin SiO_2 on Si. The GeSn thin film is clearly different in crystallographic orientation from Si, indicating that the GeSn crystal did not rely on epitaxy but occurred via nucleation and lateral growth. These GeSn thin films on ILDs can be readily fabricated into MSM photodetectors. To achieve PN junction structures for p-i-n photodiodes or electro-absorption modulators, we envision two possible approaches: (1) Use TCOs as n-type electrodes. Since defects in GeSn tend to make it p-type with a residual carrier density of the order of 10^{17} cm^{-3}, n-type TCO such as sputtered indium tin oxide (ITO) can be used to form an n-ITO/p-GeSn heterojunction structure, which is fully compatible with BEOL processing. (2) Our very recent studies found that As implantation into GeSn can be activated through rapid thermal annealing at ~400 °C with a peak dopant concentration up to 5×10^{18} cm^{-3},[74] thereby forming a p-n junction using BEOL processing. Overall, we envision that it is promising to achieve GeSn photodetectors and modulators on ILDs toward facile monolithic photonic integration.

Figure 8 compares device performance of surface-normal incidence free-space BEOL Ge and GeSn photodetectors vs their counterparts fabricated using the conventional approach, i.e., incorporating high-temperature Ge (buffer) layer growth and/or annealing to remove threading dislocations, with data from Refs. 3 and 15 (Chap. 4) and Refs. 75 and 76. Part of the reason for the lower external quantum efficiency (EQE) of BEOL Ge photodetectors is due to the limited absorber layer thickness. For example, in Ref. 64,

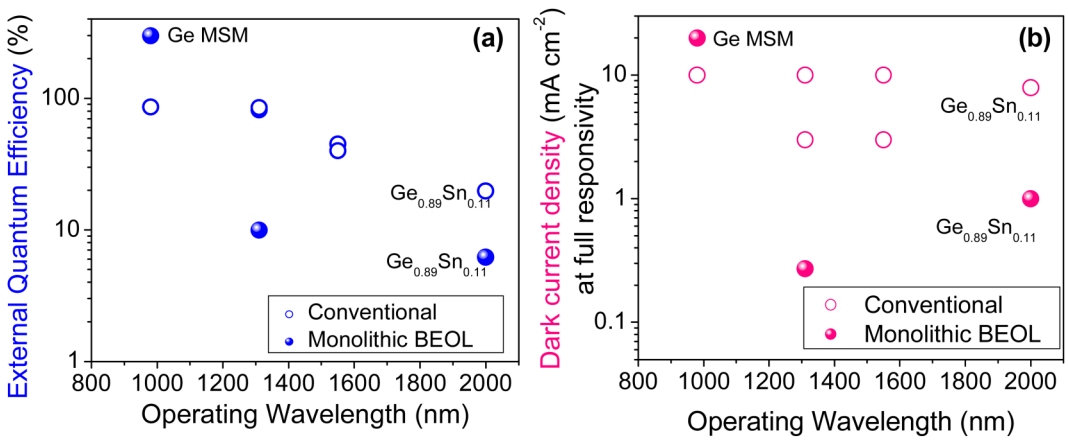

FIG. 8. Comparison of BEOL processed vs conventional I Ge and GeSn photodetectors: (a) external quantum efficiency; and (b) dark current density at full responsivity. The data points are Ge/Si photodiodes by default unless otherwise labeled on the figures.

the Ge absorber was only 0.6 μm thick, while their high responsivity counterparts in Refs. 3 and 74 exceeded 2 μm in thickness. We expect that this difference can be eliminated using waveguide coupling to effectively enhance the absorption in BEOL Ge. By comparison, the difference in EQE between BEOL and conventional GeSn photodetectors is smaller, possibly due to the unique nucleation and lateral growth process of GeSn. In terms of dark current density, both BEOL Ge and GeSn photodetectors compare favorably to their conventional counterparts [Fig. 4(b)]. A possible reason is that both Ge and GeSn are p-type instead of being intrinsic as in conventional Ge/Si p-i-n photodiodes. In the latter case, the depletion region is completely in Ge, so all defects in Ge contribute to the dark current. This promising progress suggests that future development of BEOL integration of Ge and GeSn photonic devices may open the path to 3D monolithic photonic integration for silicon photonics. For photonic interconnects, the next step will be demonstrating high-speed BEOL Ge and GeSn photodetectors. For other applications such as IR imaging or photonic sensing, 10–100 GHz bandwidth is not necessary, while the lower dark current as well as facile large-scale integration of BEOL p-Ge/p-Si/n-Si or p-GeSn/Si device structures may offer advantages over conventional epitaxial devices.

III. EMERGING TRENDS OF ACTIVE Si PHOTONIC DEVICES

This section will discuss recent progress and emerging technologies in lasers, modulators, and photodetectors for Si PICs, as well as spectrally extended and 3D image sensors on Si platform. We will also provide insights into further improvement of device performance from a materials and device physics point of view.

A. Lasers for Si PICs

In this section, we will first start with a brief discussion on off-chip vs on-chip laser sources, including wall-plug efficiency (WPE) considerations. We will then discuss monolithic III–V/Si QD lasers in O-band for photonic datalinks, as well as GaSb-based and SiGeSn/Si SWIR laser sources for infrared imaging and sensing.

1. Off-chip vs on-chip lasers

The first question under debate over the past two decades is whether to utilize external off-chip lasers or integrated on-chip lasers for Si PICs. It has often been suggested that a laser is the optical equivalence of an electrical power source. Since we put the electrical power supply off-chip, why not an off-chip laser, too? An external laser also saves the trouble of elaborate on-chip thermal management considering that the WPE of O-band and C-band lasers are usually below 50%, i.e., they generate more heat than light. Pluggable remote laser modules (RLMs) for 51.2 Tbps co-packaged optics (CPO) ethernet switching have been demonstrated by Broadcom recently using 8 × 100 mW uncooled lasers operating at case temperatures up to 50 °C, with a total power dissipation of ~8 W.[77,78] On the other hand, further scaling the number of external lasers for DWDM may be limited by the laser coupling loss typically at ~2–3 dB per interface (laser-to-fiber, fiber splitters/combiners, fiber-to-chip, etc.), which could drastically increase the power budget. Therefore, WDM by coupling multiple external lasers on-chip would not be an efficient solution for scaling.

Instead, we envision that a high-efficiency, high-power off-chip laser coupled with on-chip resonators for frequency combing would be a better choice in future development.[79–81] While currently such demonstration often requires further optical amplification,[79,82] recent progress in high-power single-mode photonic crystal surface emitting lasers (PCSELs)[83] and broad-band, low-loss free-form couplers[84] may offer low-loss coupling to further improve WDM Si PICs based on frequency comb generation. We also note that the pump-to-frequency comb conversion efficiency has been greatly improved and exceeded 50% in recent years by introducing interferometric feedback to a microring[82] or a controlled frequency shift using two coupled microring resonators.[85]

By comparison, on-chip laser diodes benefit from low coupling loss due to more precise alignments offered by lithography. They are also ideal solutions for wearable lab-on-chip integrated photonic sensors, which is now limited to benchtop systems with fiber coupling to external lasers. FMCW LiDAR systems could also greatly benefit from on-chip lasers and amplifiers due to more sophisticated device integration and functionalities on Si PICs. Considering the challenges of heat dissipation on-chip, it is interesting to first consider the optimal wavelength for short-distance optical interconnects for on-board optics (OBOs) or chip-to-chip/chip-to-memory communications. Figure 9 plots the WPE of currently available laser diodes from the visible spectrum[86,87] to 1550 nm. The maximal WPE of ~75% at room temperature has been achieved at $\lambda \sim 980$ nm using InGaAs QW lasers,[88] which exceeds 80% when cooled to 0 °C.[89] The corresponding distributed feedback (DFB) laser also shows a high efficiency close to 60%.[90] Similar to the wavelength-dependent efficiencies of LEDs,[91] the laser diode efficiency generally decreases at shorter wavelength $\lambda < 980$ nm due to materials constraints and at longer wavelength $\lambda > 980$ nm due to Auger recombination

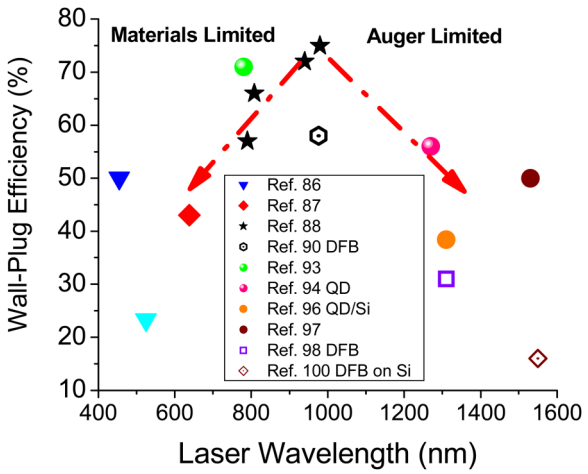

FIG. 9. Laser diode WPE vs wavelength at 300 K. All devices are QW lasers with Fabry–Pérot cavity unless otherwise indicated. Quantum dot lasers are labeled as "QD." Open symbols are DFB lasers.

constraints as the bandgap decreases.[92] For example, for wavelengths between 780 and 850 nm, the laser performance is usually limited by the stability of the AlGaAs barrier. A recent work demonstrated that changing the barrier from AlGaAs to GaAsP can drastically improve the WPE of 780 nm lasers to 71%.[93] On the other hand, as the wavelength increases to O-band and C-band, these efficiencies drop to maximal 56% around 1300 nm[94–96] and 50% at 1530 nm[97] for Fabry–Pérot cavity lasers, compared to maximal 30% at 1310 nm[98,99] and ~20% at 1550 nm for DFB lasers.[100]

Based on Fig. 9, in principle, one would select the most efficient laser sources emitting at 780–980 nm with WPE > 70% for on-chip applications in order to minimize the extra heat dissipation. However, for photonic interconnect applications, this is not compatible with the most commonly used Si modulators due to the optical absorption of Si. To overcome this issue, one could consider heterogeneous integration of III–V modulators and lasers together[101,102] or incorporate BTO/TFLN modulators in microwave photonic applications. Both could achieve better performance than existing III–V laser + Si modulator system, but they also trade-off scalability to some extent. Therefore, to best utilize the existing PIC platform, O-band (1260–1310 nm) is an ideal choice for data communication applications. We note that currently the highest WPE achieved for InAs QD on Si is ~38.4% (double-side; single-side WPE ~ 24%)[96] while those on native GaAs substrates had achieved close to 60% WPE[94] at a slightly shorter wavelength of 1270 nm (Fig. 9). This comparison indicates that there is still plenty of margin to improve the WPE of for QD/Si on-chip lasers for optical interconnects.

For on-chip photonic sensing applications, one could well consider using more efficient and less expensive 780–980 nm laser sources. On one hand, the wavelength of 780 nm is one of the standard wavelengths for benchtop Raman systems, which is well applicable for waveguide-enhanced Raman spectroscopy (WERS).[103] On the other hand, another great advantage is that high-sensitivity Si photodetectors can now be applied to integrated photonic sensing, with noise level down to sub-electron regime at room temperature for single-photon detection[104] in WERS and fluorescence spectroscopy.[105] Currently, benchtop tunable lasers in C-band dominate mainstream refractive biosensing, i.e., measuring refractive index change using microring resonators on Si PICs. This is mainly due to the wide availability of tunable laser sources around 1550 nm for telecommunication. In contrast, for on-chip refractometry, we envision that low-noise, tunable-integrated III–V QD lasers in O-band[106] are more preferred due to notably higher WPE and temperature/reflection insensitivity.

For LiDAR applications, eye-safe 1550 nm laser is desirable, and flip-chip attached hybrid lasers have already been utilized in some products.[107] They are especially relevant for coherent LiDAR systems utilizing local oscillators to measure the phase shift of reflected signals, e.g., in FMCW systems. Moving to longer wavelength could further extend the functionality of LiDAR systems, e.g., the SWIR regime for better penetration through haze/fog or further into MWIR to reach the atmospheric window.[108,109] However, they would suffer from trade-offs in both lower laser efficiency and lower detectivity for photodetectors at longer wavelengths. Therefore, 1550 nm wavelength will still be optimal for LiDAR systems in the near future.

In terms of practical implementation of laser sources for Si PICs, the research has been evolving from hybrid integration to heterogeneous integration (including intermediate approaches such as transfer printing), then to monolithic integration. Monolithic III–V QD/Si lasers in O-band for photonic datalinks,[110] together with monolithic GaSb-based[111] and SiGeSn SWIR laser sources on Si for infrared imaging and sensing,[35,112] represent a major technical advance in this aspect in the past decade. We will discuss these monolithic on-chip laser technologies in Secs. III A 2 and III A 3.

2. III–V lasers on Si

a. InAs QD lasers on Si for data communications. III–V QD lasers epitaxially grown on Si through various buffer layers have been demonstrated as efficient on-chip light sources, with the advantages of more discrete quantum states, better carrier confinement, and less defects in the active QD region compared to QW lasers. These features also notably achieved temperature and reflectance insensitive performance.[113] They represent the best-performance semiconductor lasers integrated on Si to date. This monolithic integration strategy is challenged by a combination of large lattice mismatch, dissimilar polarity (polar III–V grown on nonpolar group IV), and thermal mismatch between III–V materials and Si substrates. These hurdles have been circumvented by a two-step epitaxial growth strategy, where high-quality III–V seed layers free of antiphase domains, e.g., GaAs/GaP, are first prepared by metal-organic chemical vapor deposition (MOCVD) on planar or patterned Si wafers. This is followed by the GaAs buffer layer, InGaAs dislocation filters, and QD stack growth using MBE. An example is shown in Fig. 10 for integrating InAs/GaAs QD lasers on 300 mm diameter Si wafers.[110] In this case, micro-patterned pockets are defined on Si wafers to facilitate butt coupling with dielectric waveguides, as well as preventing crack formation due to the thermal mismatch between III–V layers and Si, which occurs in wafer-scale blanket film deposition.

The threading dislocation (TD) density of III–V on Si can be reduced to the order of low $10^6/cm^2$,[114] e.g., by using InGaAs asymmetric graded filters[115] [see Figs. 10 and 11(a)], comparable to that of Ge on Si.[116] The impact of defects is further reduced by using QDs instead of QWs as the gain media, where the probability for TDs to penetrate into the active gain regions is much reduced due to the discreteness of the QDs. More discrete energy states in strongly confined QDs also enhance the temperature-insensitivity of threshold and efficiency. In recent years, it was further discovered that post-growth misfit dislocation (MD) formation in the active QD layers acted as another important source of device degradation upon aging. These MDs are largely induced by the thermal mismatch between III–V and Si as the stress state changes from compressive to tensile upon cooling.[115,117]

To displace the MDs away from the QDs and mitigate their detrimental impact, solid solution hardening has been implemented by incorporating fully strained thin InGaAs/InAlAs layers [<10 nm QWs as trapping layers (TLs)] above and below the active region[115,117] blocking 95% of the MDs away from the QD layers. As shown in Figs. 11(c) and 11(d), laser diodes incorporating these solution-hardened TL layers successfully achieved 1200 h operation at 80 °C without degradation in the L–I curves at a constant

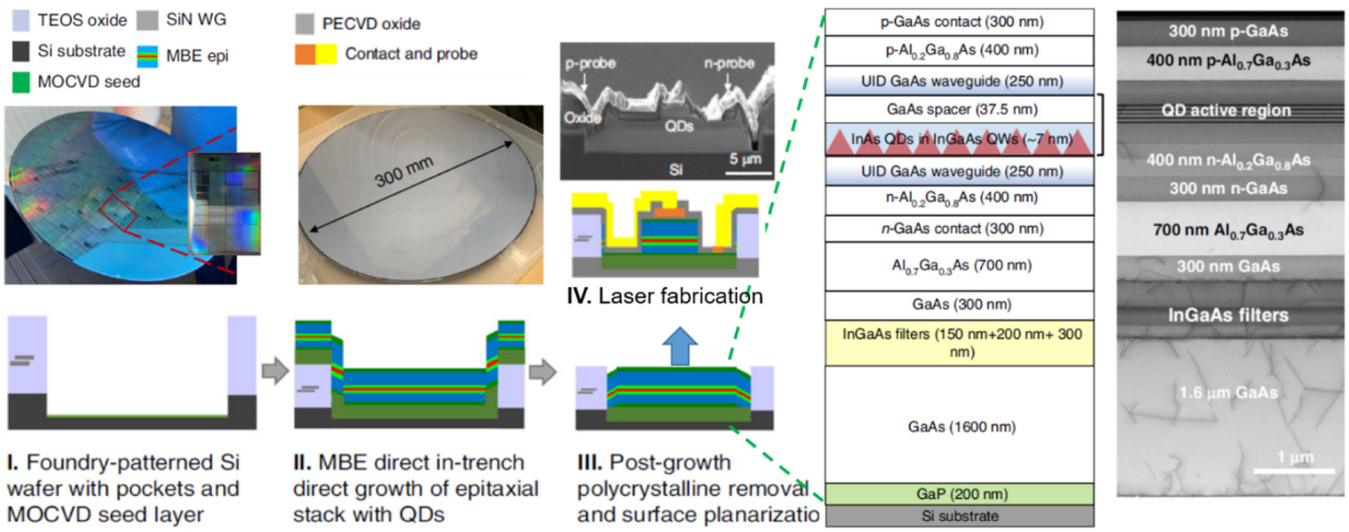

FIG. 10. Schematics of processing steps and the corresponding photos or electron microscopy images at each stage for InAs QD laser integration on 300 mm diameter Si wafers. Reproduced and adapted with permission from C. Shang, K. Feng, E. T. Hughes *et al.*, Light Sci. Appl. **11**, 299 (2022). Copyright 2022 Author(s), licensed under a Creative Commons Attribution (CC BY) license.

injection current 2× that of the threshold. The progressive improvement in managing TD and MDs in InAs QD/Si lasers enables low-threshold current density (~100 A/cm^2 at room temperature), high output powers (>50 mW), high direct modulation rate (12.5 Gb/s), high reliability (10×10^6 h extrapolated to room temperature), and high CW working temperature (up to 100 °C).[118,119] As shown previously in Fig. 9, the WPE reaches as high as 38% for InAs QD/Si Fabry–Pérot cavity lasers (counting emission from both facets),[96]

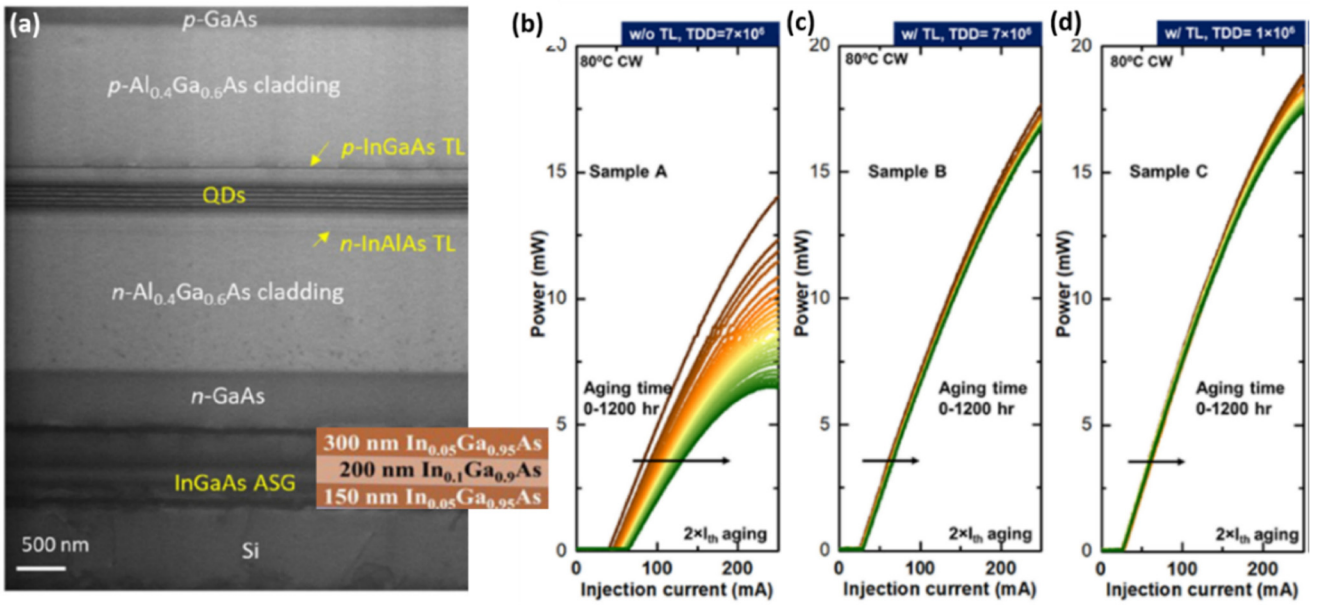

FIG. 11. (a) Cross-sectional TEM image of an optimized InAs QD/Si laser structure. TL = Dislocation trapping layers; ASG = asymmetric graded filter, as shown in the schematic inset. (b)–(d) compared the L–I curves of samples with and without TL at different dislocation densities, where (d) corresponds to the structure in (a). Reused and adapted with permission from C. Shang, E. Hughes, Y. Wan, M. Dumont, R. Koscica, J. Selvidge, R. Herrick, A. C. Gossard, K. Mukherjee, and J. E. Bowers, Optica **8**, 749–754 (2021). Copyright 2021 Optical Society of America under the terms of the OSA Open Access Publishing Agreement.

compared to 9.4% for their DFB counterparts.[119] In addition to the Si substrate, III–V QD lasers on SOI substrate have also demonstrated.[120] The thermal dissipation issue of SOI-based lasers was addressed using p-type active layer and double-side heat dissipation design.[121,122] Furthermore, optically pumped InAs quantum dash (QDash) CW lasers on Si emitting in C- and L-band have also been demonstrated in recent years, with the highest operation temperature reaching 50 °C.[123]

In addition to QD lasers, recently, IMEC has demonstrated nano-ridge InGaAs/GaAs multiple QW (MQW) laser diodes based on an adapted ART approach on a 300 mm CMOS pilot line.[124] An advantage of the ART growth is that thick buffer layers are no longer needed, and a low TD density of 10^5 cm^{-2} was achieved. A disadvantage, though, is less effective heat dissipation since the active region is essentially wrapped around by oxides, only with a line contact to the substrate along the bottom of the "V" groves. CW lasing at $\lambda = 1020$ nm was demonstrated up to 55 °C. The device can operate at room temperature for 500 h, with ~20% increase in threshold current. The high current density in the sparse metal contacts seems to be the limiting factor for the lifetime. While similar growth techniques could be transferred to MOCVD QDash lasers, the key for further improvement will be thermal management.

b. GaSb-based SWIR and MWIR lasers on Si for photonic sensing. In terms of further spectral extension into SWIR and MWIR for sensing applications, the first report of efficient GaSb-based QW laser diodes on Si achieved lasing at $\lambda \sim 2300$ nm at a threshold current density of 400–500 A/cm^2 and a maximal output power ~10 mW, and the characteristic temperatures are comparable to those grown on GaSb substrates.[111] Furthermore, GaInSb/InAs interband cascade lasers (ICLs) grown on Si based on Type-II band alignment have also demonstrated remarkable tolerance to dislocations and achieved CW MWIR lasing at $\lambda \sim 3500$ nm for 3800 h at 40 °C, with an extrapolated lifetime >300 000 h.[125] The key idea is that electrons and holes are separately confined in the conduction and valence bands on either side of a Type-II interface (see Fig. 12), such that the mid-gap defect state in the hole-confinement layer now approaches or even reaches above the conduction band edge of the electron-confinement layer. Correspondingly, the mid-gap state in the electron-confinement layer approaches or even resides below the valence band edge of the hole-confinement layer. Since the light emission is due to interband transition across the Type-II interface, this configuration effectively transforms the deep-level states in the electron and hole-confinement layers into shallow defect states or totally renders them irrelevant for the Type-II light emission, thereby effectively mitigating their adverse impacts. The Type-II transition also leads to lasing at photon energy much lower than the bandgaps of the constituent materials. Therefore, the ICL device structure provides another approach besides QD lasers to address the lattice mismatch between III–V and Si, especially for MWIR laser sources. In fact, similar ICL structures could potentially be extended to SiGeSn based on the different band alignments between SRO heterostructures shown in Fig. 2 and Ref. 41.

c. Challenges and perspectives for future development. With all the exciting progress discussed above, challenges still remain for wafer-scale integration of high-efficiency, III–V QD lasers on Si. In terms of device performance, the first 300 mm wafer-scale demonstration using a combination of MOCVD and MBE growth (see Fig. 10) achieved a WPE of ~9% at room temperature,[110] compared to 38% for those grown on smaller substrates completely by MBE.[96] Obviously, surface treatment upon transfer as well as the process integration still has plenty of margin to improve. An important reason to switch growth methods is that, despite of being the mainstream industrial growth technique offering high throughput and growth uniformity, MOCVD is not yet able to produce high-quality QDs compared to MBE.[126] That said, very recently, InAs QD CW lasers on GaAs substrates operating up to 75 °C have been demonstrated by MOCVD growth.[127] Recent progress in MOCVD QDash lasers on Si may also further extend the emission wavelength to C and L bands.[123] These advances in MOCVD QD/QDash lasers could

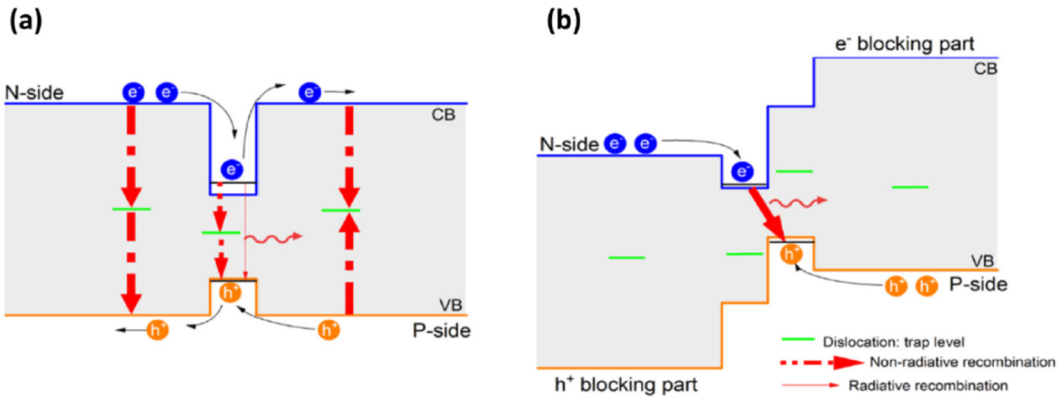

FIG. 12. Schematics showing the radiative vs non-radiative recombination in (a) regular Type-I QWs; (b) Interband transition in Type-II quantum wells. Reused and with permission from Laurent Cerutti, Daniel A. Díaz Thomas, Jean-Baptiste Rodriguez, Marta Rio Calvo, Gilles Patriarche, Alexei N. Baranov, and Eric Tournié, Optica **8**, 1397–1402 (2021). Copyright 2021 Optical Society of America under the terms of the OSA Open Access Publishing Agreement.

potentially avoid switching growth tools and maximize the throughput for large-scale Si photonic integration.

Another opportunity and challenge is TD control in pocket growth. While the initial demo in Ref. 110 showed a TD density ~10× greater than the optimized conditions shown in Fig. 11(d), thereby limiting the WPE, in principle growths in pocket windows of the order of 10 μm in lateral dimensions should facilitate TD mitigation upon annealing compared to blanket films. This is because most of the TDs can be eliminated by gliding to the edge of the mesas, as has been demonstrated in selective area growths for both GaAs and Ge on Si.[128,129] The fact that the pockets reached a higher temperature than the surroundings[110] actually facilitates such TD annealing in photonic integration as the devices nearby are less affected. The challenge, though, is that the sidewalls will require effective passivation in order to benefit from the TD reduction in small mesas, which requires further optimization. For dielectric passivation layers deposited by plasma-enhanced chemical vapor deposition (PECVD) or atomic layer deposition (ALD), a major mechanism is dangling bond termination by atomic hydrogen.[130] Moderate annealing temperatures around 400 °C could help passivate semiconductor surfaces, which has been utilized to drastically reduce the dark current in Ge/Si photodiodes.[131] *In situ* atomic hydrogen radiation has also been reported to greatly enhance dislocation annihilation in epitaxial GaAs/Si upon low-temperature growth at <400 °C,[132] since it generally enhances dislocation velocity. Furthermore, ALD as well as MOCVD Al_2O_3 has been investigated for GaAs metal–oxide–semiconductor field-effect transistors (MOSFETs), where an interfacial Ga_2O_3 layer was found to reduce midgap states induced by Ga vacancies.[133] These passivation techniques can be transferred and further optimized for III–V QD/Si laser integration.

ART and related adaptations, such as nano-ridge engineering (NRE) demonstrated in Ref. 124, can also be transferred to QDash laser growths by MOCVD. In these structures, though, thermal management will be another key factor to address on top of the surface and sidewall passivation, since the active region is surrounded by oxides and hardly has any thermal conduction path to the Si substrate.

In summary, with consistent improvement of material quality, device performance, and wafer-scale integration, we expect that monolithic III–V QD/QDash lasers will be widely applied to Si PICs in the near future for photonic data communications. The applications will start with O-band optical I/O for data centers and photonic chiplets and will potentially extend to C- and L-band with further technology development. Integration of GaSb-based SWIR and MWIR lasers has also achieved notable progress in recent years, potentially offering light sources for on-chip photonic sensing applications.

3. Group IV lasers on Si

Compared to monolithic III–V QD lasers on Si, monolithic Group IV lasers potentially offers better materials compatibility for wafer-scale electronic–photonic integration, especially considering that Ge/Si waveguide-coupled photodetectors have already become standard components in Si PICs. However, they also face two fundamental challenges: (1) conversion from indirect gap to direct gap semiconductors, which requires tensile strain and/or Sn alloying; and (2) development of new approaches to achieve lattice-matched heterostructures and QWs with sufficient band offset, as has been discussed extensively in Sec. II A. In this section, we will briefly overview existing methods to address these challenges and then evaluate the current status in reference to the early studies of GaAs lasers to find future directions of improvement. We will also summarize possible solutions based on the knowledge learnt so far, including atomic ordering of SiGeSn systems discussed in Sec. II A.

a. Current status and challenges of band-engineered Ge lasers. Since the demonstration of electrically pumped Ge lasers[11,12] using a moderate tensile strain and heavy n-type doping to bridge the gap between indirect L valleys and direct Γ valley, the research focus has evolved to further increasing the tensile strain and reducing doping level in order to minimize free-carrier absorption and inter-valence band absorption (IVBA)[134] losses. Diverse routes have been developed to enhance tensile strain on Ge membranes, micro-bridges or micro-disks. Uniaxial tensile strain as high as 6% has been achieved using Ge microbridges, enabling a direct bandgap of ~0.33 eV ($\lambda = 3.7\,\mu$m). A Ge micro-bridge laser operating up to 100 K has been demonstrated under optical pumping.[135] However, implementing electrical pumping into these suspended Ge microbridges is challenging, and the heat dissipation is poor compared to structures grown on Si substrate (which offers high thermal conductivity). The mechanical stability of these highly strained Ge microbridges also poses a significant issue in fabrication and long-term laser operation.

A second method to achieve truly direct gap Ge is based on separate electron barriers in Ge/AlGaAs multiple QWs (MQWs), in which the AlGaAs barriers provide strong quantum confinement in the indirect L valleys, but weak confinement in the direct Γ valley of Ge QWs. Therefore, the energy levels of indirect L valleys increase much faster than those in Γ valley as quantum confinement effect gets stronger in narrower Ge QWs,[136] eventually leading to indirect-to-direct semiconductor transition. An example is shown in Fig. 13(a), where a 3 nm wide Ge QW confined by $Al_{0.13}Ga_{0.87}As$ barriers in ⟨001⟩ direction leads to a direct gap ~0.1 eV lower than the indirect gap. With discrete density of states and reduced IVBA between strongly confined subbands of Ge, the carrier density required for population inversion and net material gain is reduced. Figure 13(b) shows an example of 2 nm Ge/3 nm $Al_{0.13}Ga_{0.87}As$ MQWs achieving net material gain in the Ge region in O-band, based on 8-band $k \cdot p$ simulation. Furthermore, our simulation of five pairs of 4 nm Ge/6 nm $Al_{0.13}Ga_{0.87}As$ MQWs in Fig. 13(c) using coupled Schrödinger–Poisson-current (Nextnano++ package[137]) further unveils that a laser threshold <1000 A/cm^2 can potentially be obtained for longer wavelength emission in C-band. However, it is still challenging to deposit AlGaAs/Ge MQWs with high quality due to dissimilar interfaces and very thin Ge layers required. Nucleation of III–V on Ge or vice versa is not trivial, and annealing is often needed to observe photoluminescence (PL) from Ge grown on GaAs even though the lattice mismatch is <0.1%.[138]

A third approach to convert Ge into direct gap semiconductor is to change the cubic phase into hexagonal phase, as first demonstrated by growing Ge or SiGe shells on hexagonal wurtzite GaAs nanowires (NWs) cores.[139] Very recently, material gain and

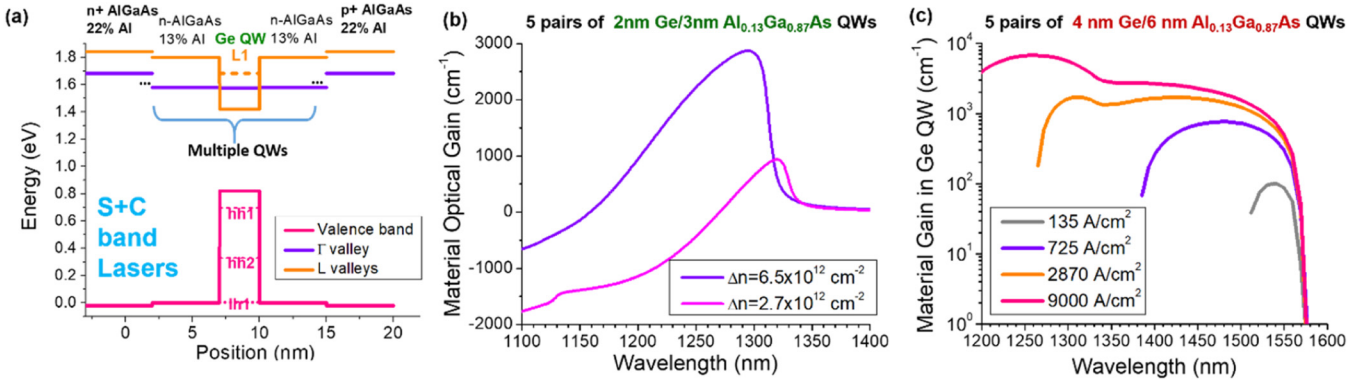

FIG. 13. (a) An exemplary band diagram of lattice-matched direct gap AlGaAs/Ge MQW laser design for S + C-band operation. The conduction band offset between AlGaAs and Ge forms a very deep potential well (~0.4 eV) for the indirect L valleys, pushing the indirect gap above the direct gap of Ge QWs. Simulated gain spectra at different carrier injection densities/current density for (b) five pairs of 2 nm Ge/3 nm $Al_{0.13}Ga_{0.87}As$ QWs and (c) five pairs of 4 nm Ge/6 nm $Al_{0.13}Ga_{0.87}As$ QWs.

amplified spontaneous emission under optical pumping has been demonstrated from hexagonal $Ge_{0.8}Si_{0.2}$ NWs at 6 K with emitted photon energy around 0.6 eV.[140] Demonstrating optical gain at a higher temperatures with low threshold would be the next step. Another practical challenge is how to transfer hexagonal SiGe growth directly onto Si substrates, which is the whole purpose of using band-engineered Ge and SiGe as optical gain media. Since it is hard to make wurtzite Si templates for this purpose, other creative approaches need to be considered.

In summary, while Ge band engineering is attractive and intriguing due to its simplicity and compatibility with CMOS electronics, so far achieving low-threshold, room-temperature lasing remains an unresolved issue despite of attempts based on different approaches. New insights and perspectives toward further improvement will be discussed later in Sec. III A 3 c.

b. Current status and challenges of GeSn lasers. As discussed in Sec. II A, alloying Ge with Sn leads to an indirect-to-direct bandgap transition. Since the first demonstration of optically and electrically pumped GeSn lasers in 2015[13] and 2020,[14] respectively, the threshold current density of pulsed GeSn laser diodes has been reduced to 0.76 kA/cm^2 at 77 K, the maximal operation temperature improved to 140 K, and the emission wavelength extended to >2700 nm (at 140 K) by increasing the Sn composition to 13 at. % and relaxing the compressive strain (i.e., making GeSn more direct gap) in a double heterojunction (DH) structure.[35,36] Very recently, CW GeSn MQW microdisk lasers have been demonstrated up to 35 K at a threshold current density of 9 kA/cm^2.[141] Under pulse injection, lasing can be observed up to 70 K.

Figure 14(a) summarizes the recent progress of GeSn lasers in terms of lasing wavelength and maximum operating temperature,

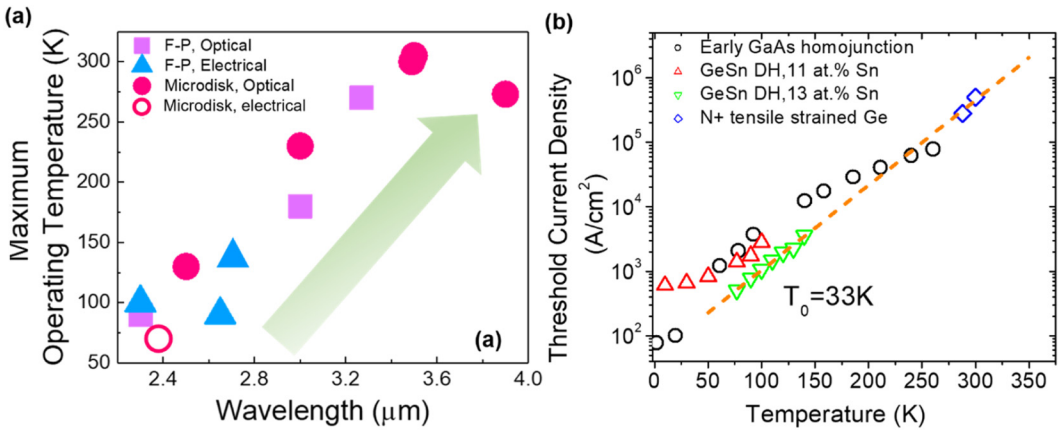

FIG. 14. (a) Maximum operating temperatures vs emission wavelengths of GeSn lasers, showing a general trend of higher maximal lasing temperature with longer emission wavelength due to the more directness of the GeSn bandgap. F–P = Fabry–Pérot cavity. (b) Logarithmic plot of threshold current density vs temperature for GeSn DH lasers in comparison with GaAs homojunction lasers and band-engineered Ge DH lasers.

using the data from Refs. 13, 14, 35, 36, and 141–150. It is clear that, irrespective of optical vs electrical pumping or Fabry–Pérot (F–P) vs microdisk cavity, GeSn lasers emitting at a longer wavelength are also capable of operating at a higher temperature. This trend indicates that a more directness of GeSn bandgap, due to a larger Sn content and/or more compressive strain relaxation, is beneficial to improve the maximal lasing temperature. However, large Sn content in GeSn or enhanced compressive strain relaxation inevitably introduces a higher density of TDs and, thus, deteriorates the epitaxial GeSn film quality. For example, with GeSn-on-insulator microdisk resonators incorporating 17 at. % Sn, Bjelajac *et al.*[149] achieved optically pumped lasing at room-temperature, yet the optically pumped lasing threshold density was also as high as 240 kW/cm^2 at 273 K, due to a higher defect density.

Unlike thermodynamically stable Ge or III–V buffer layers on Si, GeSn cannot be cyclically annealed at high temperatures to remove TDs and point defects due to Sn segregation. In particular, TDs serve as shortcuts for Sn outdiffusion and surface segregation. As TDs glide across the film, Sn also diffuses out through these channels and dumps on the sample surface along the ⟨110⟩ dislocation gliding directions.[74,151] The highest annealing temperature without segregation is ∼400 °C for relaxed GeSn thin films[74] and strained Ge/GeSn QWs[152] at ∼11 at. % Sn, while a higher Sn composition has an even lower annealing temperature limit. Therefore, this issue becomes a dilemma for further improving the material quality of GeSn with higher Sn composition and more direct bandgaps. We will further discuss strategies to address this issue in Sec. III A 3.

To evaluate the progress of electrically pumped GeSn lasers so far, it is also instructive to benchmark their threshold current densities against early homojunction GaAs laser diodes,[153] similar to the way new photovoltaic materials are benchmarked against early development of Si solar cells. For this purpose, we compare F–P cavity lasers only, as shown in Fig. 14(b). There are two intriguing observations:

(1) While the threshold of GeSn DH lasers is much higher than that of GaAs homojunctions F–P lasers at <50 K, the values are comparable for 11 at. % Sn composition at 50–100 K.[14] At 13 at. % Sn composition,[36] the threshold current densities at 77–140 K are nearly an order lower than that of GaAs homojunction lasers, reflecting the benefits of DH structures in carrier confinement at <140 K. This comparison suggests that, despite of all the defects in GeSn, 13 at. % Sn composition already achieves sufficient directness in the bandgap. SiGeSn and Ge barriers also implement sufficient carrier confinement at <140 K (i.e., for thermal excitation energy <12 meV), yet not at >150 K. Therefore, *further enhancing carrier confinement in GeSn* will be critical to achieve higher lasing temperature.
(2) The logarithmic plot of threshold current density vs temperature for 13 at. % Sn GeSn lasers[36] almost exactly aligns with that of tensile strained n$^+$ Ge DH laser diodes[11,12] (with Si barriers). Linear fitting in Fig. 14(b) indicates a common characteristic temperature of $T_0 = 33$ K, which is also similar to those of 11 at. % Sn lasers at >60 K.[14] Considering that the characteristic temperature model is based upon thermal activation of defect states that creates non-radiative recombination channels, this analysis indicates that GeSn lasers suffer from similar types of defects as band-engineered Ge lasers. In fact, n$^+$ Ge lasers cannot undergo high-temperature annealing for TD and point defect removal, either, due to out-diffusion of n-type dopants at high temperatures.[154] This comparison points to the importance of *alternative defect mitigation approaches beyond high-temperature cyclic annealing*.
(3) Furthermore, the band diagram in Ref. 36 suggests that injected carriers may well be confined in the defective n$^+$ GeSn buffer region initially because of bandgap narrowing induced by n$^+$ doping, which tends to increase the threshold and limit the operation temperature. It could also explain similar temperature-dependent threshold behavior compared to n$^+$ Ge lasers as discussed in (2). Further improving the doping profile of the device may help address this issue.

The analyses above also point to the major challenges in achieving room-temperature GeSn lasers: i.e., *carrier confinement, material quality improvement* (under the constraint of thermal stability), and *doping profile optimization*. We will discuss potential routes for future development in Sec. III A 3 toward room-temperature Group IV SWIR and MWIR lasers.

c. Perspectives of future development of monolithic Group IV lasers. Based on the aforementioned discussions in this section, we can see that the key to the success of Group IV lasers is inducing indirect-to-direct bandgap transitions with minimal defects and thermodynamic instability. Therefore, in retrospect, it is instructive to discuss the mechanism of such transitions by comparing tensile strained Ge with GeSn. As shown in Table I, it is well acknowledged that that Ge would transform to a direct gap semiconductor at ∼8 at. % Sn composition or ∼2% dilatational tensile strain. Strikingly, the corresponding lattice constants at the indirect-to-direct gap transition are almost identical. This comparison clearly indicates that Ge lattice expansion is the key to the indirect-to-direct gap transition, whether achieved by mechanical strain or alloying with larger atoms such as Sn.

It comes that *globally* stretching the Ge lattice either by large tensile strain or Sn alloying would induce inherent thermodynamic instability, which is exactly the source of Sn segregation at elevated temperatures. Therefore, a better approach would be sporadically introducing *strong but localized* lattice expansion that are more effective in inducing direct gap transitions at nanoscale, similar to the formation of QDs in terms of band structures, except that these quasi-QDs are defined by local strain. This way, the system is more

TABLE I. Lattice constants at indirect-to-direct gap transition by introducing tensile strain or Sn alloying to Ge lattice. The lattice constants are displayed in bold letters for a clear comparison.

	Indirect/direct transition
Sn composition needed	∼8 at. %
Corresponding GeSn lattice constant	$\boldsymbol{a = 0.573}$ **nm**
Dilatational tensile strain needed	∼2%
Corresponding tensile strained Ge lattice constant	$\boldsymbol{a = 0.577}$ **nm**

stable globally while the localized strain-induced "QDs" are stabilized by interfacial energy, thereby benefiting from stronger carrier confinement from the matrix material.

In the light of this insight, we can also consider engineering atomic ordering of SiGeSn alloys as an even more effective approach to induce such localized dilatational strain distortion, as discussed in Sec. II A. In other words, what really matters is not only the average Sn composition but to a great extent *the distribution of Sn atoms in terms of their atomic neighboring environment*. In particular, concentrating Sn atoms into mono/bilayers in GeSn (111) δ-DAs, instead of distributing them randomly/evenly, shows an exemplary case of enhancing local lattice distortion for the most effective band engineering at the same overall Sn composition. As discussed in Sec. II A, $Ge_{11}Sn_1$(111) δ-DAs leads to ∼2 meV direct bandgap, compared to 0.55 eV bandgap for random alloys at the same average composition of 8.3 at. % Sn. Further considering lattice-matched Type-I alignment enabled by SRO,[41] we suggest that engineering atomic ordering in (Si)GeSn is an effective new approach to achieve direct bandgap transition with minimal lattice mismatch and stronger carrier confinement simultaneously, overcoming the trade-off between Sn composition and lattice mismatch/material quality discussed in Sec. III A 3 b.

In the light of the same insight, we could also consider other "local stressors" to expand the lattice of Ge lattice besides atomic ordering in (Si)GeSn alloys. For example, instead of introducing 6% strain to an entire Ge microstructure, dispersing stressors (e.g., SiN_x) at nanoscale would be more effective to achieve strain-defined quasi-QDs mentioned earlier. Injected carriers are funneled to these highly strained regions due to smaller bandgaps. Furthermore, inspired by Ge volume expansion in lithiation as Li battery anodes, recent first-principles computational modeling studied "strain-doped" Ge, where interstitial dopants introduce strong local lattice expansion for indirect-to-direct gap transition.[155] Using hybrid functional (HSE06) that is known to produce bandgaps more consistent with experiments, they found that other than Li, filling tetrahedral interstitial sites of Ge lattice with inert gas atoms (He, Ne, Ar, etc.) can also achieve a similar effect. This result also confirmed that the indirect-to-direct gap transition is mostly due to lattice expansion. Although Li is not compatible with CMOS, while inert gas implantation is hard to control for defect recovery annealing, other interstitial atoms such as C could be interesting candidates to achieve a similar strain-dopant effect. This would be a different mechanism from the hypothesized band-crossing in substitutional GeC alloys investigated recently.[156] In fact, interstitial C would also be more stable in Ge lattice, considering the large atomic size difference between C and Ge.

In contrast to indirect-to-direct gap transition induced by lattice expansion, hexagonal (Si)Ge discussed in Sec. III A 3 a utilizes shear distortion to change the symmetry of the crystal, hence the band structure. Essentially, shear distortion along {111} planes changes the ABCABC stacking from regular diamond cubic structure into ABAB stacking in the hexagonal structure. Therefore, a potentially promising approach to implement direct gap (Si)Ge directly on Si substrates would be deliberately introducing stacking faults. Local ABAB stacking faults are identical to nanoscale hexagonal phases, which have a smaller bandgap than the diamond cubic matrix.[139] Therefore, these planar ABAB stacking faults can naturally be considered as QW regions. Furthermore, unlike dislocations, stacking faults are planar defects without any dangling bonds—it only changes the stacking sequence of (111) planes. This characteristic avoids the formation of trap states. Previous nanoscale selective area growth studies have shown that stacking faults spontaneously form when Ge grown from two selective areas impinge on each other, leading to at a stacking fault density of $\sim 10^8/cm^2$ with a low TD density $<10^6/cm^2$.[157] A similar phenomenon has also been observed in Ge/Si ART growths.[66,67] Since hexagonal Ge has a much smaller bandgap than cubic ones (0.28 eV direct gap vs 0.67 eV indirect gap),[139] it could well be that previous studies had never investigated photoluminescence (PL) at the MWIR regime from these samples. We thereby suggest to revisit the potential application of Ge stacking faults in nanoscale selective area growth or ART growths in order to test if it would be a feasible approach to monolithically integrate hexagonal Ge and SiGe into Si PICs.

Last but not least, we note that in addition to the Type I QW depths for stronger carrier confinement, having *direct gap barriers* is also highly desirable for Group IV QW lasers. Otherwise, a case opposite to that of Fig. 13(a) could occur, i.e., the indirect bandgap barrier layers could provide stronger confinement of Γ valley electrons in the QWs and raise their energy level relative to the indirect L valleys, driving the QW material toward the indirect gap again. This phenomenon has indeed been experimentally demonstrated when direct gap GaAs or GaSb QWs/QDs below ∼2 nm are confined in indirect gap barriers,[158–160] This issue is also exactly why the SiGeSn/GeSn MQWs in Ref. 141 adopted thick wells with thin barriers in order to mitigate the adverse effect of indirect gap SiGeSn barriers, at the cost of not fully benefiting from lower density of states in QWs compared to DH structures. Again, engineering atomic ordering in SiGeSn could potentially address this challenge, as shown in Fig. 2 and Ref. 41.

In conclusion of Sec. III A, Table II summarizes the monolithic laser performance and emerging technologies for Si PICs. We envision that InAs QD/QDash lasers will dominate optical I/O and data communication in the near future. Their major competitor will be high-efficiency external lasers coupled with on-chip frequency comb generation. GaSb-based lasers on Si will most likely be applied to the SWIR and MWIR spectral regimes earlier than (Si)GeSn lasers due to a much higher level of technical readiness. Currently, the threshold current density of GeSn DH lasers is already lower than early GaAs homojunction lasers at low temperatures <140 K [Fig. 14(b)]. Sufficient directness of the bandgap has been achieved at 13 at. % Sn composition with almost complete strain relaxation. The major bottleneck is insufficient carrier confinement in QWs at elevated temperatures. Further engineering atomic ordering in SiGeSn alloys offers a promising new path to drastically enhance carrier confinement in lattice-matched Type I QWs toward on-chip SiGeSn laser sources for applications such as LiDAR and on-chip biosensing. Other emerging approaches, such as hexagonal (Si)Ge and strain-doping of Ge, will need further studies to increase the optical gain and decrease the threshold current density for practical applications. Revisiting the optical properties of stacking faults in epitaxial Ge/Si from nanoscale selected area growth and ART growth may provide valuable insight into scalable fabrication of hexagonal (Si)Ge on Si, because local ABAB stacking faults are structurally identical to nanoscale hexagonal phases.

TABLE II. Summary of monolithic lasers and emerging technologies for Si PICs.

	Monolithic III–V on Si				Monolithic Group IV on Si		
	InAs QD[96,118,119]	InAs QDash[123]	Nano-ridge InGaAs MQW[124]	GaSb-based[111,125]	(Si)GeSn[35,36]	Tensile strained Ge[11,12]	Hexagonal Ge and SiGe[139,140]
Spectral range (nm)	O band	C + L bands	1020	2000–3500	2000–2700	C + L bands	1900–2100
Threshold (kA/cm^2)	~0.1 @ 300 K	4 kW/cm^2 @300 K, optically pumped	0.6–0.7 @300 K	0.3–0.4@ 293 K	0.76 @ 77 K 3.6 @140 K	280 @ 280 K; 500 @300 K;	…
WPE (%)	38 for F–P (both facets) 9.4 for DFB	…	1.33%	~6 (both facets)	<1%	<1%	…
Max. temperature (K)	373	323	328	353	140	300 K with n^+ doping	Amplified spontaneous emission (ASE) observed at 6 K
Future work	Pocket growth and wafer-scale process optimization; MOCVD QD growth	Material quality optimization for electrical pumping	Thermal management; passivation; metal plug optimization	Device structure optimization and defect mitigation	Engineering atomic ordering, including SRO and δ-DA	Nanoscale local stressor and/or "strain dopants" for strain-induced QDs	Transfer to Si substrate (e.g., by engineering stacking faults in nanoscale selective area Ge epitaxy)

B. Photonic modulators

While directly modulating vertical cavity surface emitting lasers (VCSELs) coupled with multimode fibers are widely used in short-distance photonic datalinks, it requires increasingly higher injection current at higher data rate in order to decrease the stimulated emission lifetime.[161] Therefore, external modulators are preferred at >50 Gb/s data rate to reduce the power consumption for integrated photonic circuits. Another advantage compared to direct modulation of lasers is that there is no perturbation to the laser cavity itself, which reduces the noise in modulated optical signals.

Photonic modulators encode electrical signals onto optical waves, including phase and/or intensity modulation based on changes in the real (Δn) and/or imaginary part (Δk) of the refractive index. Conventionally, photonic modulators primarily based on Δn are called electro-optical modulators (EOMs), while those primarily utilize Δk are called EAMs considering the absorption coefficient change $\Delta\alpha = 4\pi\Delta k/\lambda_0$, where λ_0 is the wavelength in vacuum. Modulators are the key components in the transmitter subassembly of transceiver products, and they are indispensable elements to realize reconfigurable unitary matrices in quantum computing.[162] Phase modulation by utilizing free-carrier plasma dispersion (FCPD) effect and LEO (Pockels) effect,[163] or amplitude modulation by employing Franz–Keldysh (FK) effect[7,164] and quantum-confined Stark effect (QCSE),[165,166] have been implemented on Si PICs through monolithic heterogeneous and hybrid integration.

The optimal solution for high-speed modulators is dependent on the applications of Si photonics. This section will briefly discuss the recent progress of FCPD Si modulators and potential improvements utilizing existing strained Si technology in CMOS electronics, then overview the rapid development of LEO modulators based on TFLN and ferroelectric oxides for microwave photonics, and GeSi FK/QCSE EAMs for ultralow energy photonic datalinks on Si PICs. We also envision that synergistically utilizing both Δn and Δk may lead to new mechanisms for highly efficient modulation, with an example of hybrid plasmonic QCSE EAM[167] toward fJ/bit ultralow power modulation.

1. FCPD modulators

a. Current status and challenges of Si FCPD modulators. The lack of LEO effect in bulk Si, due to its centrosymmetric crystal lattice, directs Si modulators into the FCPD effect[168] by carrier injection, depletion[169] or accumulation[6] implemented in device configurations of p-i-n/p-n junctions or metal–oxide–semiconductor (MOS) structures. The biggest advantage of Si modulators is facile and large-scale integration, which helps them dominate optical modulation in Si PICs. A complete review of Si FCPD modulators can be found in Ref. 170. With tremendous efforts of research and development, Si FCPD modulators are now commercially available as standard components in Si PICs and included in PDK libraries of Si photonics foundries. The best performance of Si FCPD modulators offers data rates exceeding 100 Gb/s, $V_\pi \cdot L < 0.3$ V cm and energy consumption of ~pJ/bit for Mach–Zehnder modulators (MZMs), and tens of fJ/bit for typical Si microring modulators (MRMs, without considering the power for thermal tuning).[170] The co-optimization of

driver-modulator design may offer a single-channel data rate beyond 100 Gb/s while preserving a good modulation efficiency.[171]

However, the performance of Si modulators is limited by the FCPD effect itself, which tends to be less efficient in terms of speed and power consumption than field-effect modulation mechanisms such as LEO, FK, or QCSE. Another major disadvantage is that the FCPD is tightly linked to a spurious amplitude change $\Delta\alpha$, based on Kramers–Kronig relation, which leads to poor linearity at high modulation frequencies >100 GHz. This factor, together with TPA at telecommunication wavelengths discussed earlier, makes it challenging for Si FCPD modulators to compete in microwave/RF photonics applications.

b. Perspectives of future development of FCPD modulators. To further enhance the FCPD effect in Si while best leveraging existing resources and fabrication in CMOS electronics, we envision that the most convenient solution would be utilizing strained Si. Note that FCPD is largely based upon semi-classical Drude model, where the Δn is inversely proportional to the conductivity effective mass.[168] For TE mode in Si waveguides, which is the most commonly used configuration due to a higher optical confinement factor, the FCPD depends on the in-plane *conductivity* effective mass. Under ~1% tensile strain commonly used in strained Si CMOS transistors, the energy degeneracy of the 6 Δ valleys in $\langle 100 \rangle$ directions are broken. Two out-of-plane Δ_2 valleys in [001] direction are now lower in energy than the four in-plane Δ_4 valleys. Therefore, under biaxial tensile strain, electrons will occupy the out-of-plane Δ_2 valleys in k-space, and they sample the smaller transverse effective mass ($m_t = 0.19\, m_0$) upon in-plane transport under TE polarization [Fig. 15(a)]. Correspondingly, the conductivity effective mass of electrons will decrease from $0.26\, m_0$ to $0.19\, m_0$.[172] Similarly, the light and heavy-hole bands also become non-degenerate, reducing the conductivity effective mass of holes from 0.28 to $0.18\, m_0$ under tensile strain [Fig. 15(b)].[173] The reduction in the conductivity effective mass of electrons and holes alone would lead to ~1.5× improvement in refractive index change Δn for the same change in free-carrier density.

We also note that the FCPD effect of holes in Si is stronger than the prediction of Drude model,[168] suggesting the actual impact on Δn from holes in strained Si can be even larger than the estimation above. Furthermore, both the electron and hole mobility increase by 2×,[172] facilitating carrier depletion under reverse bias to enhance the transit-time limited bandwidth of Si FCPD modulators. Therefore, the same stressor approach applied to enhance the mobility of Si CMOS transistors can well be transferred to strain-enhanced Si or SiGe FCPD modulators.[174] Indeed, recessed SiN_x stressors have been demonstrated for spectral extension of Ge-on-Si waveguide photodetectors,[175] which can be easily transferred to strain-enhanced Si modulators on Si PICs.

Another emerging path of improving Si modulator performance is coupling with high-mobility transparent conductive oxide (TCO) as a high-efficiency, low-loss gate material for Si MRMs. These high-mobility gating materials enhance the FCPD effect at the TCO/gate oxide interface (i.e., TCO also being part of the active modulator material), and enable Q factor optimization to achieve sub-1 V modulation and high (photon-lifetime limited) bandwidth simultaneously. Low-resistivity TCO also enables higher RC-limited bandwidth. For example, recently, a high-mobility Ti-doped indium tin oxide (ITiO) has been heterogeneously integrated with a Si MOS capacitor (MOSCAP) microring resonator to achieve 0.8 V operation at 25 Gb/s data rate and ~50 fJ/bit power consumption.[176] Similar device structures incorporating better TCO materials on strained-enhanced Si MRMs may achieve further improvement in modulator performance.

2. Pockels effect (LEO) modulators

Beyond Si FCPD modulators, in recent years, other high-performance LEO materials have been integrated on the Si platform for high-speed, high-linearity optical modulation,[177] especially for integrated microwave/RF photonics, where linearity requirement at high input optical power is much more critical than data communication. The ultrafast intrinsic response of field-induced Pockels

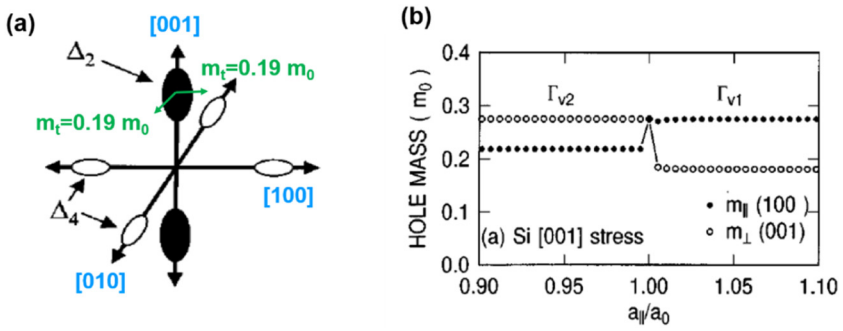

FIG. 15. Schematics showing the mechanism of enhanced FCPD effect in tensile strained Si. (a) Conduction band occupation of the Δ valleys under in-plane biaxial tension. Electrons fill the lower energy Δ_2 valleys (symbolized by the solid ovals) and experience the smaller transverse effective mass m_t upon in-plane transport under TE polarization. Here, m_0 is the static mass of an electron. (b) Effective mass of holes vs lattice strain for Si (001). Reproduced and adapted from M. L. Lee, E. A. Fitzgerald, M. T. Bulsara, M. T. Currie, and A. Lochtefeld, J. Appl. Phys. **97,** 011101 (2005). Copyright 1995 AIP Publishing LLC, and M. V. Fischetti and S. E. Laux, J. Appl. Phys. **80**, 2234 (1996). Copyright 1996 AIP Publishing LLC.

effect enables a modulation rate of several hundred Gb/s for EOMs, superior to that of Si FCPD modulators.

a. Recent progress of LEO modulators. Strain-gradient SiNx. In principle, strain gradient in Si can break the perfect inversion symmetry and induce $\chi^{(2)}$ nonlinearity for the Pockels effect in Si. While early experimental work demonstrated promising results for Si with SiN_x stressors,[178] it was later found out that strain alone could not explain the observed magnitude of the Pockels effect.[179] It turns out that the observed LEO enhancement largely came from the charge centers and/or strain gradient in the amorphous SiN_x stressor instead.[179,180] Therefore, recently, electrical poling of SiN_x is becoming a new direction of research for monolithic, highly scalable LEO modulators on Si,[181,182] especially considering the remarkable success of low-loss SiN waveguides in recent years. LEO in low-loss SiN_x could also potentially overcome the TPA limitation in Si modulators. This work is still at an early stage, though, with demonstrated $\chi^{(2)}$ of the order of 1 pm/V and potentials to reach tens of pm/V.[182]

TFLN. For decades, the Pockels effect has been exploited in discrete bulk $LiNbO_3$ modulators for long-haul telecommunication. This success drives the integration of thin film LN modulator on Si, benefiting from the small device dimensions that enables low-voltage operation (for the same applied electric field) as well as strong mode confinement when coupled with SiN or SOI waveguides.[177] The breakthroughs in high-quality TFLN on insulator (TFLNOI) material fabrication rapidly advanced TFLNOI modulators in recent years.[183–187] By 2020, the best TFLNOI modulator already achieved an on-chip IL of 2.5 dB, $V_\pi \cdot L \sim 2.2$ V cm, on-off keying (OOK) modulation rate of 100 Gb/s and high linearity by exploiting vertical adiabatic couplers to transfer the optical power fully between Si waveguides and LN modulators.[188]

To further enhance the performance at higher bandwidth, the novel electrode design plays a critical role. Conventionally, reducing V_π requires either decreasing the gap between electrodes or elongating the device length, yet both also increase RF losses and reduce the 3 dB bandwidth. Very recent work has been focusing on improving these electrode design, e.g., using micro-structured traveling wave electrodes to reduce RF losses[189] or shifting the waveguides closer to the signal electrodes in ground-signal-ground (GSG) configuration in order to increase the electric field in the active LN regions. This approach has achieved a 2 dB bandwidth of 100 GHz, and the extrapolated 3 dB bandwidth reaches 170 GHz, one of the highest reported on silicon photonics platform so far, with $V_\pi \cdot L \sim 3.3$ V cm.[190] Single-channel OOK modulation up to 100 Gb/s and eight-level pulse-amplitude modulation (PAM-8) at 240 Gb/s have been demonstrated, at a power consumption of ~120 fJ/bit in the latter case. Furthermore, the propagation loss of dry etched TFLNOI waveguides with high optical confinement in the active LN region has been improved to the order of 0.1 dB/cm.[191] The material-limited loss in ion-sliced LN is as low as 0.015/cm, while the Q factor of the TFLNOI micro-resonator could potentially reach 10^8 with post-fabrication annealing.[192] These results suggest that it is also promising to achieve low-power, high-speed TFLNOI MRMs.

BTO. A limitation to the existing TFLNOI LEO modulators, though, is the scalability. Most of the device demonstrations are achieved on a small fabrication area at low throughput. Lithium is also incompatible with CMOS as a mobile ion. Therefore, for practical applications, it has to be integrated using BEOL processing as the last step.[193] For significantly higher LEO performance and more facile integration, other ferroelectric oxide-based thin film modulators, such as BTO on Si,[194–196] are also being investigated intensively. BTO can be grown epitaxially on Si/SOI.[194] BTO thin film modulators on SiO_2 demonstrate a data modulation up to 50 Gb/s and a large Pockels coefficient of $r_{42} \sim 923$ pm/V (i.e., nearly 30× higher than LN) using a combination of epitaxy and direct wafer bonding.[196] The low defect density in single-crystalline film and low surface roughness of epitaxy BTO films are beneficial for obtaining high yield of BTO bonding on top of the interlayer dielectric front-end-of-line (FEOL) structure.

In recent years, plasmonic BTO modulators integration with SiN waveguides have achieved rapid progress. These devices synergistically utilize large LEO effect of BTO, strong optical and RF confinement/overlapping offered by plasmonic slot waveguides [see the comparison with TFLN in Figs. 16(a)–16(d)], as well as low-loss, low TPA SiN waveguides to enable high-power, high-linearity microwave photonics.[197,201,202] The Au/BTO/Au slot waveguide phase shifter also benefits from the slow light effect (i.e., slow group velocity due to large dispersion) to enhance light–matter interaction, such that the confinement factor in BTO can approach unity (~0.96 in Ref. 197). A very low $V_\pi \cdot L \sim 0.014$ V cm and >200 Gb/s data rate have been demonstrated, showing superiority in both modulation efficiency and bandwidth. These features are especially desirable for high-performance integrated microwave photonics. A trade-off common to all plasmonic slot waveguides, though, is the metal-induced IL of ~0.3 dB/μm, which can amount to >6 dB in plasmonic BTO MZM structures.[197] This is hard to avoid for microwave photonics applications since MZM is required for linearity. When used for data communication, on the other hand, the IL due to the inherent ohmic loss in Au can be reduced by coupling with microresonator structures for modulation. Since the incident light hardly couples into the microresonator in the "on" state, it does not see the loss in the plasmonic phase shifter as part of the resonator structure. While there is still trade-off in the Q factor of the resonator due to the plasmonic loss, a BTO plasmonic racetrack modulator did reduce the IL to 2 dB while maintaining 200 GBd.[198]

AlN and ferroelectric ScAlN. An emerging competitor of LEO material for Si photonics is AlN-based ferroelectric nitrides such as ScAlN. AlN itself has a Pockels coefficient of the order of 1 pm/V,[203] similar to strain-gradient SiN_x discussed earlier, but it also offers transparency all the way to the UV spectrum. Furthermore, a recent study has shown that ferroelectric ScAlN has potentials to catch up or exceed the performance of TFLN.[204] Interestingly, atomic SRO also plays an important role in high Sc composition ScAlN to boost the LEO coefficients,[204] in addition to a significant impact on the band structures of SiGeSn discussed in Sec. II A. The integration of wide bandgap nitride semiconductors on Si platform is further accelerated by the needs of power electronics in recent years. There is a good chance that Si photonics could also benefit from this surge in nitride semiconductor integration.

Temperature-resistant EO polymers. Beyond inorganic LEO materials, EO polymers with large LEO coefficients have been actively investigated in the past two decades, yet long-term stability

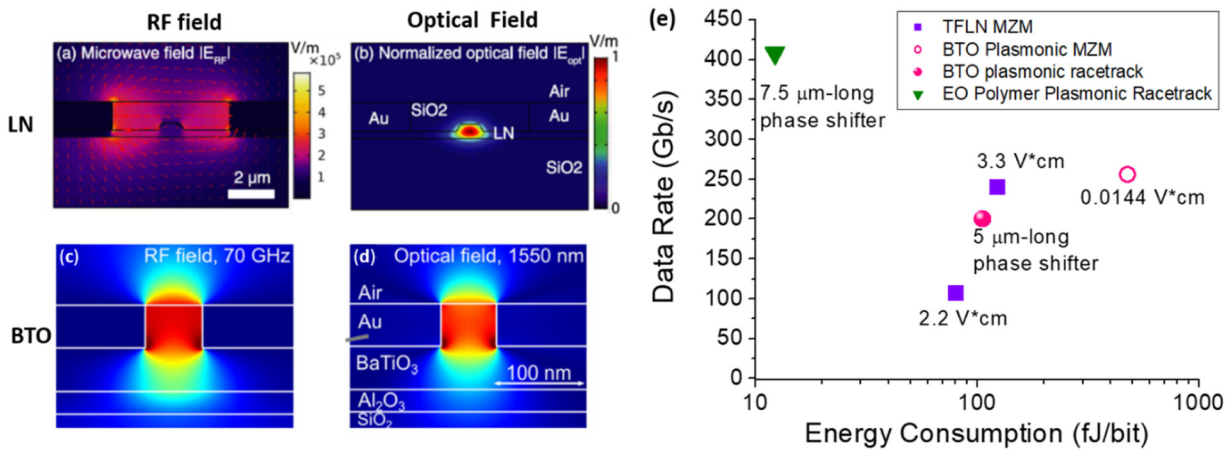

FIG. 16. (a)–(d) Comparison of RF and optical field confinement between TFLN and plasmonic BTO phase shifters. (a) and (b) have been reproduced with permission from Di Zhu, Linbo Shao, Mengjie Yu, Rebecca Cheng, Boris Desiatov, C. J. Xin, Yaowen Hu, Jeffrey Holzgrafe, Soumya Ghosh, Amirhassan Shams-Ansari, Eric Puma, Neil Sinclair, Christian Reimer, Mian Zhang, and Marko Lončar, Adv. Opt. Photon. **13**, 242–352 (2021). Copyright 2021 Optical Society of America. (c) and (d) have been reproduced with permission from A. Messner *et al.*, J. Lightwave Technol. **37**(2), 281–290 (2019). Copyright 2019 Author(s), licensed under a Creative Commons Attribution (CC BY) license. (e) Summary of data rate vs energy/bit of some start-of-the-art TFLN, BTO, and E-O polymer modulators (Refs. 190 and 197–200). Energy/bit for BTO modulators is estimated using phase shifter geometry and a microwave dielectric constant of $\epsilon_{RF} \sim 1000$ (measured at 20 GHz)[197,201] considering that the RF field is well confined in the Au/BTO/Au slots. Values of $V_\pi \cdot L$ are labeled for MZMs, while phase shifter lengths are labeled for racetrack modulators.

of organic materials in photonic circuits has been a persistent concern. Recently, plasmonic EO polymer race track modulators with a record data rate of 408 Gb/s at a low-power consumption of 12.3 fJ/bit was achieved on Si PIC for the first time.[199] The device also showed high thermal stability up to 85 °C, running at 100 GBd non return to zero (NRZ) for more than 5 h without degradation in eye diagram. The thermal fluctuation tolerance is also nearly 30× better than Si MRM references. This remarkable demonstration shows the potential of EO polymers for high-performance modulators in the future.

b. Future directions and applications of LEO modulators. Figure 16(e) summarizes some of the best-performance LEO modulators demonstrated recently. The performance of TFLN and BTO modulators is clearly superior to that of Si FCPDs in both bandwidth and energy consumption. In the near future, though, it is likely that Si FCPD modulators and their enhanced versions (e.g., via strain engineering as mentioned earlier) will still dominate data communication applications due to their maturity and high scalability. It is in high-performance microwave photonics that LEO modulators become indispensable. Therefore, we envision that major applications of LEO modulators will be integrated microwave Si PICs in the near future. With improvement and cost reduction in fabrication and integration, LEO modulators may be applied to some high-end data communication applications where modulators capable of hundreds of Gb/s are needed.

Another interesting factor to consider is the application of plasmonic LEO modulator structures. As discussed earlier, this approach is advantageous for data communication applications to minimize the modulation power consumption using plasmonic racetrack resonator structures. However, for MZMs in RF photonic applications, this could be an issue in terms of optical loss from plasmonic waveguides. Note that the RF power delivered is proportional to the square of photocurrent, I_{ph}^2, while I_{ph} is proportional to the input optical power from the modulator. Therefore, 1 dB IL will translate to 2 dB RF loss. At the current level of ~6 dB IL from plasmonic modulators MZMs, the corresponding RF loss would be >10 dB. In this case, one would rather trade-off $V_\pi \cdot L$ for lower IL. Overall system performance needs to be taken into account for device design and optimization based on its applications.

From the data in Fig. 16(e), we can also see that BTO plasmonic MZMs are indeed much more compact than TFLN with orders of magnitude lower $V_\pi \cdot L$. On the other hand, the energy/bit is actually on the same order as TFLN, seemingly a bit counterintuitive. This is mostly due to the ultrahigh microwave dielectric constant ϵ_{RF} ~1000 for ferroelectric BTO.[201] A great advantage of high ϵ_{RF} is that the RF field is extremely well confined and almost perfectly overlaps the optical field compared to TFLN [Figs. 16(a)–16(d)],[197,202] which greatly enhances the effective LEO coefficient of the phase shifter and enables very small $V_\pi \cdot L$. The disadvantage is that the capacitance/unit length is also drastically increased, so the power consumption is higher per unit length in charging/discharging the capacitive phase shifter at a given V_{pp}. One could consider increasing the phase shifter length to some extent while reducing the V_{pp} to decrease the overall power consumption, since energy/bit scales with linearly with C but quadratically with V_{pp}^2. For plasmonic slot waveguide phase shifters, though, the length is also limited by the plasmonic loss on the order of 0.3 dB/μm. All these trade-offs could be further explored and optimized for ferroelectric modulators.

For EO polymer modulators, there is no doubt that they can provide some of the best modulation performance on Si PIC so far, as discussed earlier. The major concern is long-term stability when operating on chip with temperatures up to 80 °C, leading to

reservations from the photonics industry. One of the key factors is to increase the glass transition temperature, T_g, yet such efforts do not necessarily align with the optimization of LEO coefficients. There has also been relatively few studies on the long-term aging performance of EO polymers, even though 2000 h operation at 85 °C has been demonstrated for some high T_g EO polymers.[205] The optical power density threshold for damaging also needs to be determined. Since most of the experts in integrated photonics are not able to develop new EO polymer materials themselves, close collaborations between the photonics community, the organic chemists, and industrial partners will be needed to push EO polymers into the mainstream Si PIC fabrication process. Overall, we consider EO polymers a promising candidate for ultrafast, low-power modulation for data communication. They are probably not suitable for high-power microwave photonics due to damage threshold concerns, though.

For all these high-performance LEO materials, facilitating wafer-scale integration will be the key factor for their future success. BEOL integration is much preferred over FEOL since it does not modify the CMOS electronics processing flow. To this end, local heaters in the SuMMIT HI approach discussed in Sec. II B may provide an effective solution. For example, local heating enhanced crystallization of BTO could be achieved without affecting surrounding regions, as has already been applied to on-chip garnet magneto-optical isolators.[63] As sputtered and pulse-laser deposited BTO has already demonstrated a high LEO coefficient,[195,206] this approach seems highly feasible for large-scale BEOL integration of BTO modulators toward microwave Si PICs. Therefore, we envision that BTO will surpass TFLN over time for integrated LEO modulators due to a much higher Pockels coefficient, a more compact device footprint, and better scalability for integration.

3. Semiconductor FK/QCSE modulators for Si PICs

Compared to EOMs, EAMs based on FK or QCSE induce an extinction/absorption coefficient change ($\Delta k \sim 0.01$–0.1 or $\Delta\alpha \sim 10^3$–$10^4\ \mathrm{cm}^{-1}$) by applying an electric field of the order of 50–100 kV/cm to tilt/shift the direct band edge of semiconductors. QCSE further benefits from the exciton peak shift to achieve an even larger $\Delta\alpha$. In fact, Δn at photon energies near the direct gap can also reach 0.01–0.1 according to Kramers–Kronig relation, although EAMs mostly utilize Δk. Such large Δk and Δn opens the possibility of synergistically utilizing both for energy-efficient modulation, as will be further discussed in III B 3 b. The FK/QCSE induced refractive index change (Δn) appears notably larger than those of the FCPD or LEO effect because of the proximity of photon energies to the resonant transition of the direct gap. By comparison, the working wavelengths of FCPD and LEO modulators are far from the resonance in order to minimize the absorption losses. For the same reason, the device length of FK/QCSE EAMs is typically much shorter than most of the EOMs, comparable to plasmonic EOMs or Si MRMs of the order of 10 μm, with relatively broadband operation (~30 nm spectral width near the band edge). This small footprint leads to lower capacitance, higher bandwidth, and lower power consumption for Si PICs, especially for photonic data communications. EAMs typically need a more elaborate design for linear modulation since the transfer function depends on both the material and the device structure;[207] therefore, they are less investigated for microwave photonic applications.[208]

a. Recent progress of FK/QCSE modulators. Figure 17(a) summarizes the development of GeSi EAMs over the past decade in terms of bandwidth and energy efficiency, while Fig. 17(b) summarizes the corresponding evolution in system performance. Since the first demonstration of tensile strain-enhanced, butt-coupled GeSi FK EAMs (0.8 at. % Si, 1.2 GHz bandwidth at 25 fJ/bit OOK)[7] and strong direct gap QCSE in Ge/SiGe MQWs,[165] system integration of Ge/GeSi EAMs has also gained more momentum in the past decade, driven by bandwidth and energy efficiency requirements in data communications. The first commercialization effort was made by Kotura (later acquired by Mellanox Technologies) in 2009–2015, who integrated lateral junction Ge and GeSi EAMs with Si ridge waveguides.[209–211] They also demonstrated the first multi-channel GeSi FK EAM array (9 channels × 10.25 Gb/s) integrated with 40 nm CMOS technology node digital drivers for system-level

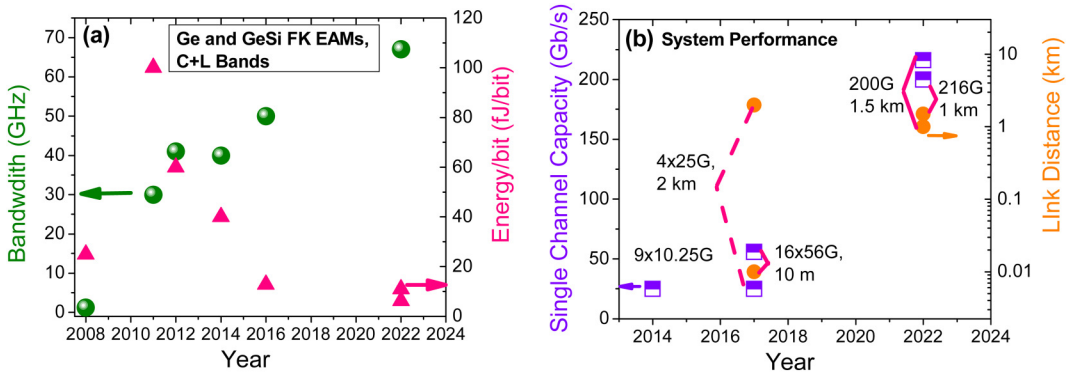

FIG. 17. (a) Evolution of Ge and GeSi FK EAM device performance over time in terms of bandwidth and energy/bit. (b) Evolution of system integration using Ge and GeSi FK EAM in terms of single-channel capacity and distance of the photonic data links. The corresponding multi-channel performance is labeled beside the data points. Data are compiled from the corresponding references discussed in the main text.

integration, with EAM bandwidth >40 GHz at 50 fJ/bit energy consumption and 2 V_{pp}.[212] The total energy consumption was 570 fJ/bit *including* the modulator driver.

Early GeSi FK EAMs adopted butt coupling schemes. In 2015–2016, researchers at IMEC introduced a taper-enhanced, evanescently coupled Ge EAM device structure with a bandwidth/data rate of 50 GHz/56 Gb/s.[213,214] A very low dynamic energy consumption of 12.8 fJ/bit and 30 nm spectral range was achieved at 2 V_{pp}. Built upon this development, they subsequently demonstrated a 16×56 Gb/s GeSi EAM-PD array coupled to multicore fibers to achieve 896 Gb/s for short reach (1–10 m) optical links.[215] The system fully implemented the original device integration scheme proposed in Ref. 216 in 2007, i.e., having a single epitaxial growth with the same GeSi composition for both EAMs and PDs to facilitate their integration. The PDs are simply longer than EAMs in order to absorb almost all input optical power for photocurrent generation. They further demonstrated the first 100 Gb/s NRZ OOK transmission (4×25 Gb/s data streams) using GeSi EAMs on 200 mm SOI platform for up to 2 km through dispersion shifted fiber.[217]

By 2022, Ge L-band FK EAMs have reached >67 GHz bandwidth at 6.3 fJ/bit dynamic power consumption, enabling single channel 80 Gb/s NRZ data transmission.[218] Single-channel C-band GeSi EAMs with >67 GHz bandwidth working at 100 GBd was also demonstrated in 2022, enabling 108 GBd (216 Gb/s) over 1 km and 100 GBd (200 Gb/s) over 1.5 km standard single-mode fiber transmission.[219] These GeSi EAMs were implemented using IMEC's PDK,[17] marking the entry of these devices in to mainstream Si PIC foundries. Recent studies have also demonstrated high reliability of GeSi EAMs with >10 years projected lifetime under accelerated aging tests,[220,221] maintaining 56 Gb/s data rate up to 85 °C.[222] Overall, after a decade of development, GeSi FK EAMs are ready for large-scale deployment for high-speed and low-power Si PICs.

Compared to tensile-strain-enhanced GeSi FK EAMs, Ge/GeSi MQW QCSE modulators are more complicated to fabricate due to the more sophisticated growth of MQWs. Therefore, high speed QCSE modulators were demonstrated later than their FK counterparts. Due to quantum confinement in Ge QWs, the operation wavelength is shorter than Ge (L-band) and GeSi FK EAMs (C-band). The first waveguide-integrated Ge QCSE EAM working at 1450–1470 nm was reported in 2012 with a very compact footprint of $0.8 \times 10\,\mu m^2$ and an ultralow power consumption of 0.75 fJ/bit utilizing the large $\Delta\alpha$ in QCSE. O-band modulation was first demonstrated by increasing the Si composition in the barrier layers to induce even stronger quantum confinement and blue-shift the direct gap of Ge QWs,[223] which matches well with InAs QD lasers discussed earlier for datacom applications. In 2021, IMEC demonstrated the first waveguide-integrated high speed Ge QCSE EAM with 50 GHz bandwidth and 60 Gb/s data rate at $\lambda = 1320$ nm, where 2% Si was introduced to the QW regions in order to blue-shift the bandgap.[166] The capacitance of the device was subsequently decreased below 40 fF with an estimated power consumption of 38 fJ/bit for 2 V_{pp}. The data rate was further improved to 100 Gb/s in 2025.[225,225]

As mentioned earlier, the large Δk near the band edge induced by FK or QCSE can also induce a large Δn for phase modulation. Back in the early days of studying the FK effect in epitaxial Ge/Si, this large field-induced Δn has already been evaluated.[226] On the other hand, at that time, Si FCPD modulators were flourishing, and there was not a strong motivation to invest in FK phase modulators yet. With the ever demanding requirement for bandwidth and energy efficiency in Si PICs, the demand for more efficient and compact phase modulators on Si is also increasing in recent years. In 2024, the large Δn of GeSi MQW QCSE has been applied to achieve an ultralow $V_\pi \cdot L = 0.036$ V cm for phase modulation on 300 mm Si photonics platform for the first time.[227] Considering the maturity of the corresponding QCSE EAMs, we expect high speed modulation of QCSE EOMs at low dynamic power consumption in the near future.

b. Perspectives of future development: Synergistic utilizing Δk and Δn. Clearly, GeSi FK and QCSE EAMs have achieved dramatic progress in the past decade. The major limiting factor for the fabrication of these devices used to be selective area growths and chemical mechanical polishing for surface planarization of GeSi, which were not widely available in photonics foundries back in the early 2010s. With technical development in the past decade, these issues have already been resolved, and GeSi EAMs have already become standard components in the PDK of IMEC's Si photonics foundry.[17] Due to the benefits of small footprint, high speed, and low power consumption, we envision that GeSi EAMs will be more and more widely applied to Si PICs for large-scale, energy-efficient data communications. Based on the direct bandgaps, tensile-strain-enhanced GeSi and Ge FK EAMs will be applied to C + L bands, while GeSi QCSE EAMs will be applied to O-band.

From a device physics point of view, the only remaining challenge to be addressed for GeSi FK/QCSE modulators is the insertion loss due to the indirect gap absorption. While the IL is still comparable to depletion mode Si FCPD modulators, for large-scale integration, the IL and coupling loss at each photonic component could add up to a notable power consumption, adversely affecting the competitiveness of photonic interconnects compared to their electrical counterparts for chip-to-chip or chip-to-memory communications. We envision two solutions to further enhance the performance of GeSi EAMs:

(1) *Tensile strain to enhance the directness of the bandgap*: Based on existing EAM structures, this is a facile approach to reduce the indirect gap absorption. Unlike lasers discussed earlier, EAMs do not need such a large tensile strain for complete conversion into a direct gap; it only needs to further reduce the difference between direct and indirect gaps. Considering that SiNx stressors have already been applied to extend the spectral response of Ge/Si photodetectors in recent years,[175] it will be relatively straightforward to apply similar approaches to reduce the IL of GeSi EAMs.
(2) *Synergistically utilizing both Δk and Δn:* We envision that this approach will further enhance FK and QCSE modulators near the direct band edge of semiconductors.[167,228] As discussed earlier, since FK/QCSE works near the direct gap resonance, very large Δk and $\Delta n \sim 0.01$–0.1 can be achieved. Conventionally, EAMs only utilize Δk, while FK/QCSE EOMs have to work at wavelengths further away from the direct gap in order to avoid absorption losses when utilizing Δn for phase shifting. We have

proposed a new concept of utilizing both, where Δn was utilized to control the coupling between the input optical power and the EAM. For the "ON" state without an applied electric field, there is little optical coupling into the EAM, such that the IL is very low. After an electric field is applied for the "OFF" state, the large Δn induces optical coupling of incident light into the highly absorbing EAM. The extinction ratio (ER) can also be further enhanced if other optical loss mechanisms are introduced to the off-state of the EAM, e.g., plasmonic losses. Note that in this case, the field-induced Δn is utilized in the "OFF" state only; therefore, it does not introduce any additional chirp to the transmitted light in the "ON" state.

An example of utilizing both Δn and Δk has been explored for GaAs QCSE electro-reflective modulators, as shown in Fig. 18. Electroreflective modulators based on QCSE are of interest for optical switching arrays and bidirectional communication systems. However, these conventional devices typically require a high driving voltage (7–10 V) to achieve an adequate ER due to the thickness of the MQW stack. We proposed a reflective modulator based on hybrid plasmonic coupling, synergistically leveraging large changes in both absorption coefficient ($\Delta\alpha \sim 10^4\ cm^{-1}$) and refractive index ($|\Delta n| \sim 0.05$).[167,228] As shown in Fig. 18(a), a large $|\Delta n| \sim 0.05$ at $\lambda = 850–860$ nm under 80 kV/cm electric field was confirmed from electro-reflectance measurements of p-i-n diodes comprising 30 pairs of 3.5 nm $Al_{0.30}Ga_{0.70}As$/10.5 nm GaAs MQWs in the intrinsic region. Theoretically, wavefunction coupling between the QWs leads to coupled QCSE (Co-QCSE) that broadens the Δn spectrum, which indeed showed better agreement with experimental results than QCSE modeling based on isolated QWs. Figure 18(b) schematically shows the electro-reflective modulator structure and its coupling with polymer waveguides and VCSELs. In the "ON" state, the incident light from the input waveguide is mostly reflected by a 20 nm Au thin film to the output waveguide, thereby minimizing the IL. In the "OFF" state, due to the large $|\Delta n| \sim 0.05$ at $\lambda = 850–860$ nm shown earlier in Fig. 18(a), the incident light is coupled to a hybrid plasmonic-MQW slab mode [see the inset of Fig. 18(c)], achieving a high ER with strong absorption from both the Δk of the QCSE MQW and the plasmonic losses. This way, we use both absorption mechanisms only for the "OFF" state, which minimizes the IL and maximizes the ER. This type of electro-reflective EAM can achieve an ER of 35–50 dB at an IL of 1–3 dB, an incident angle tolerance of ~5°, and a spectral bandwidth ~10 nm at 1 V reverse bias. The modulator power consumption is estimated to be ~2 fJ/bit, and the RC-limited bandwidth well exceeds 100 GHz.

This concept of utilizing both Δn and Δk through hybrid plasmonic coupling can be readily applied to GeSi FK and QCSE effects modulators. For integration on Si PICs in data communication applications, the hybrid plasmonic structure can be simply changed into a waveguide version, as has already been utilized in EO polymer and BTO racetrack modulators discussed earlier in Sec. III B 2. The GeSi section in the race track would act both as a phase shifter and an EAM,[229] and it does not necessarily need the plasmonic waveguide structure since the high refractive index of GeSi already provides strong optical confinement in resonator structures. In those cases, we envision that Ge/GeSi QCSE may achieve even better performance than BTO or EO polymer since the magnitude of Δn near the direct band edge (~0.05 at 80 kV/

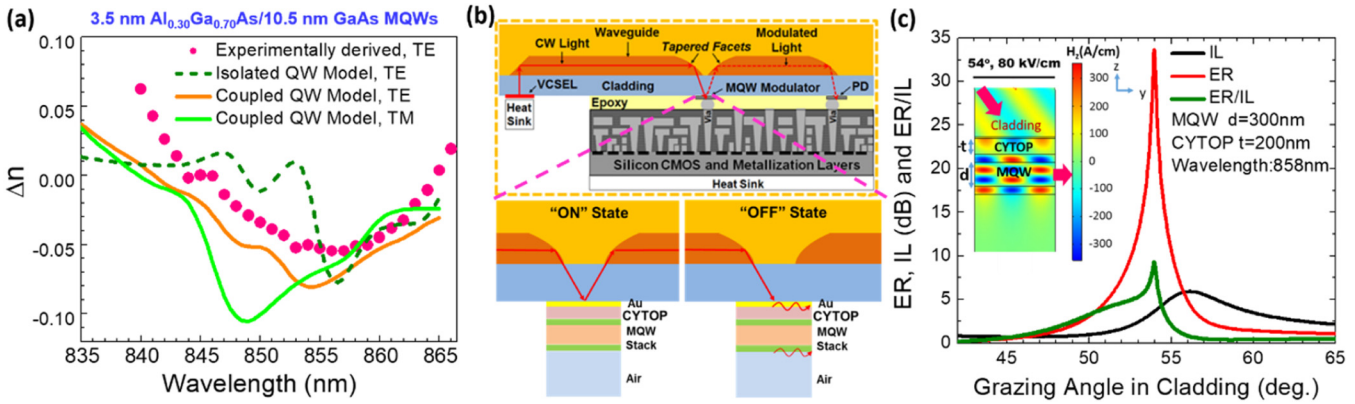

FIG. 18. (a) Comparison of experimentally measured vs theoretically modeled refractive index (real part) change Δn at 80 kV/cm electric field. Here, "TE polarization" means that the electric field of the incident light is parallel to the MQW plane, while "TM polarization" means it is perpendicular to the MQW plane. (b) Schematics of a chip-to-chip optical interconnect layout co-packaged with integrated circuit chips showing the integration of VCSELs, multiple quantum MQW QCSE modulators, and photodetectors (PDs) with polymer waveguides. The modulation principle of the hybrid plasmonic-MQW QCSE modulator is schematically illustrated for "ON" state (0 V) and "OFF" state. In the "ON" state, the incident light from the input waveguide is mostly reflected by a 20 nm Au thin film to the output waveguide. In the "OFF" state, due to the large $|\Delta n| \sim 0.05$ shown in (a), the incident light is coupled to a hybrid plasmonic-MQW slab mode to achieve a high extinction ratio. (c) IL, ER, and ER/IL ratio as a function of grazing angle in the cladding for an optimized structure with MQW thickness d = 300 nm and CYTOP thickness t = 200 nm. The inset shows the corresponding distribution of the z-component of the magnetic field (H_z) under 1 V reverse bias (80 kV/cm) at a grazing angle of 54° for p-polarized light, indicating effective coupling to the hybrid plasmonic-MQW slab mode for the optimal ER/IL ratio. Here, the CYTOP thickness is t = 200 nm, and the MQW thickness is d = 300 nm. Reproduced with permission from X. Wang, S. Yu, H. Zuo, X. Sun, J. Hu, T. Gu, and J. Liu, IEEE J. Sel. Top. Quantum Electron. **27**, 3400108 (2020). Copyright 2020 IEEE.

cm) is comparable, while the additional Δk in GeSi would further enhance the ER at OFF state once the incident light is coupled into the GeSi MQW EAM.

On the other hand, surface-incident GeSi FK/QCSE electro-reflective modulators with hybrid plasmonic coupling could be utilized to form a large array of optical switches and find potential applications in 3D imaging and LiDAR. They are especially relevant for focal plane switch arrays (FPSAs), where switching is implemented by microelectromechanical systems (MEMS) in Si PICs for now.[230] The energy consumption of switching could be drastically reduced using FK/QCSE mechanisms.

4. Summary and outlook

Table III summarizes the current applications of different types of modulators discussed above and potential evolutions under each application. We envision that Si FCPD modulators and their improved versions (e.g., with strain enhancement, integration with TCO MOSCAP structures, etc.) will still dominate Si PICs for data communication applications in the near future. With strain-induced enhancement in both FCPD and carrier mobility discussed earlier, it is expected to support the growth of data rate in the next decade due to high maturity and scalability. The rapid progress in QCSE/FK modulators, including those synergistically using Δn and Δk discussed earlier, will be highly attractive for the next generation of ultralow power modulators, without requiring extra power for thermal tuning as Si MRMs. These will be best applied in cases where low-power, high-speed, and high-volume integration are needed simultaneous, e.g., for on-board photonics and 2.5D/3D electronic–photonic integrated circuits. Plasmonic BTO and EO polymers are potential competitors in data communication systems, yet for now BTO lags behind in the scale of integration compared to GeSi FK/QCSE modulators, while EO polymers lack industrial acceptance due to reliability concerns. For the latter, increasing glass transition temperature T_g while maintaining a high LEO coefficient will be critical factors for their future deployment in Si PICs. For microwave/RF photonics applications, TFLN, BTO, and other related LEO modulators will take over Si modulators and dominate integrated microwave PICs.

Plasmonic modulator devices help us to enhance light–matter interactions and reduce device footprint/energy consumption. In these cases, a general rule to minimize metal-induced IL and maximize ER would be coupling the light into the plasmonic phase shifter or EAM *only* in the optical "OFF" state. This way, the plasmonic loss is used to our advantage in that it enhances ER at "OFF" state. In addition to applications as high speed modulators, hybrid plasmonic GeSi FK/QCSE or BTO structures discussed earlier are also promising for applications in large-scale FPSA for on-chip LiDAR, potentially competing with MEMS in existing FPSA systems. EOM phase shifters based on materials with large EO effects, such as GeSi QCSE, BTO, or EO polymers, may also be applied to optical phased arrays, competing with mainstream thermo-optical phase shifters currently used in Si OPAs.

C. Photodetectors

1. Perspectives of Ge/Si photodetectors

Since the pioneering work of tensile strained Ge/Si photodetectors[3,75,231–233] and waveguide integration[4,234] in the early and mid 2000s, Ge/Si photodetectors advanced rapidly and became mature by the early 2010s.[235] In the past decade, Ge/Si photodetectors have become standard components in practically all Si photonics foundries by now (e.g., IMEC, AIM Photonics).[16,17,236] For example, AIM photonics PDK provides Ge/Si photodetectors with a responsivity of 1 A/W, a bandwidth of >45 GHz, and dark current of <15 nA at −2 V.[16] A recent review of Ge/Si photodetectors for data communications can be found in Chap. 4 of Ref. 15. Overall, waveguide-integrated Ge/Si p-i-n photodetector performance is comparable to their III–V counterparts. The bandwidth has reached as high as 265 GHz,[237] fully satisfying the needs of data communication systems. To further facilitate high-density 3D photonic integration, BEOL processing of Ge detectors is being investigated, as has been discussed in Sec. II B 2 and Fig. 8.

With internal multiplication gain, Ge APDs are vital to drastically improve the detection sensitivity. The state-of-the-art Ge/Si APDs employ a separate absorption-charge-multiplication (SACM) scheme, in which Ge acts as the near infrared (NIR) absorption region and Si as the low-noise multiplication region, respectively. The demonstration of Ge/Si 10×10 APD array with high-sensitivity and large detection area opens the route to the LiDAR application.[238] Overall, Ge/Si APDs exceeded the performance of III–V APDs in bandwidth-gain product, thanks to the low-noise Si multiplication layers (see Chap. 4 of Ref. 15). The Ge/Si single-photon avalanche diode (SPAD) working in the Geiger mode demonstrates a detection efficiency of 38% at 125 K at a wavelength of 1310 nm, offering a route toward large SPAD arrays for use in quantum technology applications.[239] The development of large-

TABLE III. Summary of modulators/phase shifters on Si PICs and their potential future evolutions.

	Data communication			
	O-band	C/L-band	Microwave photonics	LiDAR
Current technology	Si FCPD		Si FCPD; TFLN	Si thermo-optical; MEMS
Further improvement	Strained Si; TCO MOSCAP		Large-scale integration and electrode optimization of TFLN	Si FCPD
Next generation	GeSi QCSE;	GeSi FK	Plasmonic BTO	BTO; GeSi QCSE
Other competitors	Plasmonic BTO, EO polymers		Strained SiNx; AlN; ferroelectric nitrides (e.g., ScAlN)	EO polymers

scale Ge/Si APD/SPAD arrays with robust CMOS fabrication may speed up Ge/Si entering the LiDAR application field dominated by III–V APDs.

There are still two areas of applications where Ge/Si photodetector still cannot catch up with their III–V counterparts:

(1) *Microwave photonics*: This application requires simultaneous achievements of high-linearity, high-saturation photocurrent, and high 3 dB bandwidth under high input optical power. Traveling wave photodetectors (TWPDs) and uni-traveling carrier (UTC) photodetectors are commonly used for this application. UTCs typically use heterojunction band offsets to collect photoelectrons while blocking the holes in order to enhance the speed of the photodetectors. In this area, Ge/Si still lags behind InGaAs/InP in that the bandwidth and the saturation current of UTCs and TWPDs are still notably lower than III–V devices for microwave photonics applications. The bandwidth of Ge/Si TWPDs and UTC is limited to ∼30–40 GHz at a saturation current of 2–8 mA,[240,241] compared to >100 GHz bandwidth at >10 mA saturation current and 60 GHz bandwidth at >40 mA saturation current from their III–V counterparts on InP[242,243]

To address this challenge, we could consider fully utilizing the benefits of Ge/Si photodetectors in large-scale integration on Si platform. For example, the overall microwave photonics system performance could be boosted by splitting the incident optical power among dense Ge/Si detector arrays instead of a single high-performance detector in this case, benefiting from a much higher thermal conductivity of Si compared to InP.

(1) *Photon counting detectors*: This application is mostly limited by the dark current in Ge/Si photodiodes. The dark current density of Ge photodiodes tends to be significantly higher than that of InGaAs. This is because the indirect gap of Ge is only 0.66 eV, nearly 0.1 eV smaller than that of InGaAs photodetectors for telecommunications. Another complication is that, while cyclic annealing is effective in removing TDs in the Ge absorber layer, the Ge/Si interface still has a high density of MDs (average spacing ∼10 nm for fully relaxed Ge), while photoelectrons have to move across this defective interface to reach the Si multiplication layer in APD devices. While these drawbacks are less of an issue for data communication since it is shot noise limited, for weak light detection in LiDAR systems or NIR imaging, the problem will be amplified. Therefore, photon counter Ge/Si APDs tend to suffer from a large dark count rate and need to operate at lower temperatures.[239]

From an integrated photonics point of view, efficient HI of III–V absorbers on Si would be a more ideal solution than Ge/Si SPADs. As discussed in Sec. II B 1 and Fig. 5, III–V "grafted" on Si through a high-quality tunneling oxide layer could potentially integrate the best of both and achieve high-performance SPADs on Si. Nearly ideal junction performance has already been demonstrated, which avoids the highly dislocated interface between Ge and Si. We envision that both Ge/Si and grafted III–V/Si SPAD approaches will be developed in the near future, and they may cater for different applications depending on how stringent the requirement is on dark counts vs cost and scalability.

2. Perspectives of GeSn photodetectors

As discussed earlier, alloying Ge with Sn pushes the optical response to SWIR and MWIR range for optical sensing and imaging applications. The development over the past two decades or so increased Sn concentration in GeSn from ∼1% up to ∼30%, extended the detection cut-off wavelength from 1650 to 4600 nm and reduced the dark current density from 10 A/cm^2 to 1 mA/cm^2 for <10 at. % Sn composition [see Fig. 19(a)].[244–247] At $\lambda = 2400$ nm, the maximal detectivity D* was 1.1×10^{10} cm Hz$^{1/2}$ W^{-1} at 77 K and

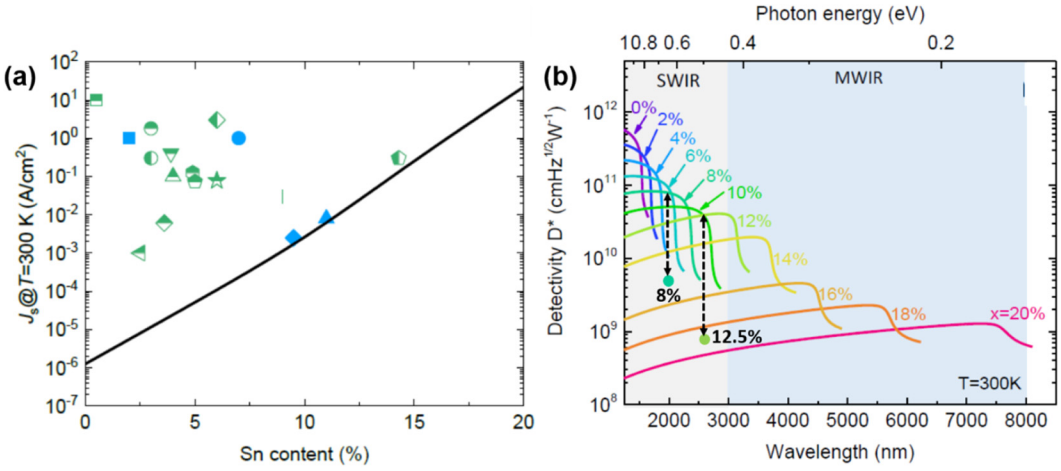

FIG. 19. Comparison of theoretical limit vs experimental data for (a) dark current density vs Sn content and (b) spectral detectivity at different Sn compositions. The arrows show the gaps between theoretical and experimental detectivities for 8 at. % Sn[248] and 12 at. % Sn.[249] Reproduced and adapted from G.-E. Chang, S.-Q. Yu, and G. Sun, Sensors **23**, 7386 (2023). Copyright 2023 Author(s), licensed under a Creative Commons Attribution (CC BY) license.

$\sim 1 \times 10^9$ cm· $Hz^{1/2}$·W^{-1} at 300 K, respectively, for 12.5 at. % Sn composition, slightly higher than smaller bandgap PbSe but still more than an order of magnitude lower than extended InGaAs (with a similar cut-off wavelength of 2600 nm) or PbS detectors (with a longer cut-off wavelength at ~3600 nm).[249]

High-speed GeSn photodetectors are also being developed toward SWIR optical communications systems based on Thulium-doped fiber amplifiers at 2000 nm wavelengths.[250] All the best specifications are not yet fulfilled in a single GeSn photodiode. For example, a GeSn detector with a bandwidth of 7.5 GHz at a bias of 5 V has a 2600 nm cut-off wavelength, a 0.3 A/W responsivity, and a dark current density of 10 A/cm^2 at room temperature.[251] The highest bandwidth reported so far, on the other hand, was 30 GHz at 2000 nm wavelength under −3 V bias, yet with an optical responsivity of only 14 mA/W and a dark current density of 125 mA/cm^2 in a $Ge_{0.96}Sn_{0.04}$ alloy.[252]

Recently, the theoretical limit of GeSn photodiodes was analyzed and proposed as "Rule 23."[247] A recent summary of GeSn detector performance can be found in Ref. 253. Therefore, we will not further extend the literature review here but focus on discussing the dark current density hurdle due to the GeSn film quality. As shown in Fig. 19, most of the experimentally reported dark current at −1 V are significantly higher than the theoretical values. In fact, even the best detectivity values reported in Ref. 248 for 8 at. % Sn and Ref. 249 for 12 at. % Sn at 300 K are still ~20× lower than the theoretical values of "Rule 23" [Fig. 19(b)]. As discussed earlier, a major challenge is that the Sn segregation at elevated temperatures does not allow conventional cyclic annealing to help remove TDs and point defects to mitigate dark current. To address this fundamental barrier, we envision the following strategies for SWIR and MWIR detectors, respectively:

(1) *SWIR*: In this case, the most feasible approach would be pseudomorphic GeSn thin films and MQWs enhanced by photon management. For SWIR detection at <2700 nm wavelength, a Sn composition <12 at. % is sufficient. In this case, the lattice mismatch between GeSn and the Ge buffer is within ~1.5%, such that pseudomorphic growth below the critical thickness is still feasible to provide notable SWIR absorption and prevent MD/TD formation at the same time. Furthermore, GeSn/Ge QWs in this temperature range can sustain RTA up to 400 °C to reduce point defects and improve the responsivity.[152]

This strategy is especially suitable for waveguide-integrated detectors for SWIR communication applications, since the GeSn photodetector can simply be made long enough in the longitudinal direction to absorb all the input optical power from the waveguide, while carrier collection is implemented in the thin thickness direction to minimize carrier transit time. For GeSn/Ge MQWs, the detection spectrum can also be redshifted using QCSE, thereby covering a larger spectral range.

For surface-incident detectors, e.g., for LiDAR or image sensing, we could utilize photon management to greatly enhance GeSn absorption. For example, high refractive index Ge nanohole array metasurface has been applied to Ge/GeSn MQW photodetectors and achieved a detectivity of 5×10^9 cm $Hz^{1/2}$ W^{-1} at $\lambda = 2000$ nm at 300 K,[248] one of the highest for room-temperature GeSn SWIR detectors reported so far. Interestingly, beyond high refractive index Ge ($n \sim 4$), Sn itself has an ultrahigh refractive index of $n \sim 9$ at SWIR wavelengths of 2000–3000 nm,[254] which has been utilized to significantly enhance the responsivity of Ge[255] and graphene photodetectors by up to 20×[254,256] based on synergistic near-field enhancement and antenna coupled cavity enhancement. Compared to Ge nanoholes, Sn nanodots can be self-assembled into pseudo-periodic structures by controlling deposition conditions,[257] thereby facilitating fabrication and offering broadband photon management. Furthermore, self-assembled Sn/SnO nano-needle structured TCO thin films can serve as a tensile stressor and an electrode simultaneously, which is especially suitable for synergistic band engineering and photon management.[258] We envision that a similar approach

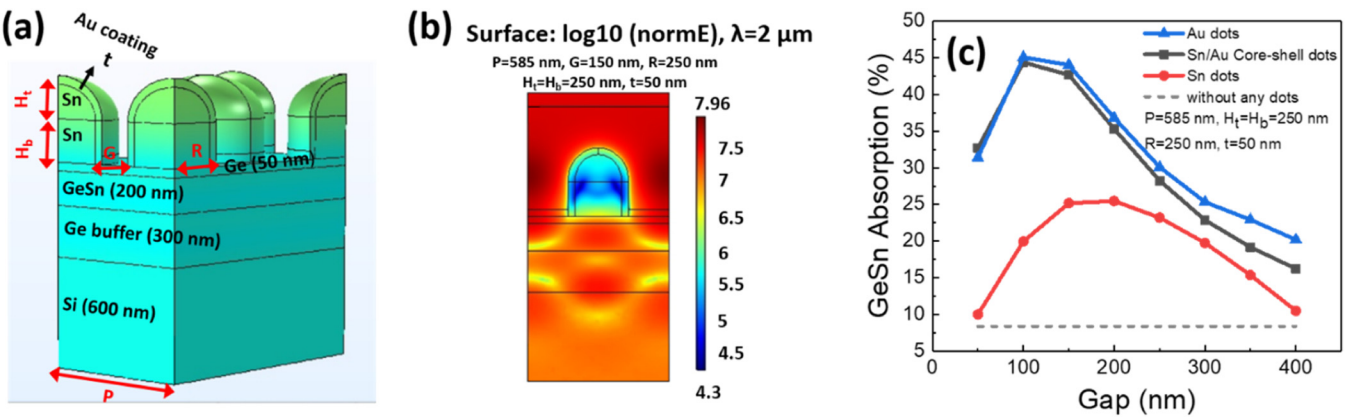

FIG. 20. (a) Schematic structure of Sn/Au core–shell dots on vertical GeSn/Si (8% Sn) photodetector to enhance GeSn absorption, (b) surface plot of norm electric field (V/cm, log scale) of Sn/Au dot on the GeSn/Si photodetector, and (c) comparison of GeSn absorption as a function of gap between Au dots, Sn/Au core–shell dots, Sn dots, and no dots. A 50 nm-thick Au coating on 250 nm radius Sn dots enables a maximum GeSn absorption similar to the case of Au dots, i.e., 5 times of the case without light trapping structures.

can be adapted for surface-incident GeSn photodetectors in SWIR regimes. Figure 20 shows such an example. Here, Sn nanodots alone can enhance the absorption of GeSn by 3× at $\lambda = 2000$ nm, while adding a thin Au coating on the surface of Sn nanodots will lead to ∼6× absorption enhancement. In the latter case, self-assembled Sn nanodots themselves serve as a template such that there is no need to conduct lithography on Au on ∼100 nm scale.

To further increase optical absorption, we can also consider using a GeSn absorber thickness somewhat larger than the critical thickness and adopt lateral junction photodiode structures to avoid the defective GeSn/Ge interface compared to vertical junction structures. Since the defective interface is not in the junction region, the dark current could be reduced. It has been shown that a planar lateral GeSn photodiode yields a detectivity an order of magnitude higher than that of the conventional vertical counterpart.[259] We have also shown that dopant ion implantation and dopant activation is feasible for up to 11 at. % Sn composition.[74] Therefore, the lateral junction of thicker GeSn, combined with photon management, is feasible to further increase the detectivity in SWIR regime.

(1) *MWIR*: In this respect, we envision that the community will need to shift the focus from increasing Sn composition to engineering atomic ordering for spectral extension. Based on recent studies of spontaneous intermixing of Sn into Ge nanoclusters upon room-temperature co-deposition, the metastable solubility of Sn in Ge nanoclusters is estimated to be ∼18 at. % at room-temperature.[260] Increasing Sn composition beyond 20 at. % would deviate too far from the thermodynamic stability range even for GeSn nanostructures, thereby leading to lots of defects in the film. For example, vacancy formation energy tends to decrease with Sn composition because vacancies tend to help accommodate the lattice distortion induced by Sn. Furthermore, as mentioned in Sec. III A 3 b for GeSn lasers, Sn segregation goes hand in hand with TD gliding. If we want to remove TDs by allowing them to glide and annihilate each other, Sn would inevitably diffuse to the surface through these TDs and get dumped along the paths of TD motion. Our annealing testing of CVD epitaxial GeSn sample with 18 at. % Sn also showed dense cross-hatch patterns and strain-field induced surface undulations in the as grown samples, as well as extensive Sn segregation after RTA for 1 min at 300 °C, making it impossible to do any heat treatment to remove TDs.

Based on the discussion above, we can see a fundamental trade-off between Sn segregation and TD removal for Sn composition at 18 at. % and above. We envision that further increasing Sn composition in GeSn alloys would most likely be an effort in vain for practical device applications if we simply continue doing regular dislocation-assisted relaxation of GeSn on Ge buffer layers. Creative ideas that could facilitate elastic strain relaxation through lateral overgrowth without impinging the growth areas, such as 2D material mediated remote hetero-epitaxy[261] or aspect ratio trapping (ART),[67,68] could potentially resolve part of the problem and achieve high Sn composition at higher quality. However, so far, there have been few studies on GeSn selective area growth to implement these attempts. A very recent preliminary investigation on GeSn ART showed improved crystallinity yet relatively low Sn incorporation.[68] Much effort will be needed to fully understand how to incorporate Sn in these lateral elastic strain relaxation processes.

Therefore, the key idea to achieve high detectivity at MWIR regime is red-shifting the direct gap transition with minimal Sn compositions, therefore minimal lattice mismatch with the Ge buffer. The goal can potentially be reached by engineering atomic ordering in the SiGeSn system. Recalling our discussions in Sec. II A, engineering atomic ordering potentially allows us to achieve ∼3 meV bandgap with an average Sn concentration of 8.3% at a GeSn/Ge lattice mismatch of 1.2% using $Ge_{11}Sn_1$ δ-DAs. Therefore, any bandgap in MWIR and even long-wave IR regime can be achieved within 1.2% lattice mismatch by engineering atomic ordering in GeSn, which has a much better promise to implement both MWIR spectral extension and high heteroepitaxy quality. As stated earlier, what matters to a large extent is not the Sn composition, but where to distribute the Sn atoms in order to induce bandgap shrinkage most effectively.

In addition, SRO in SiGeSn ternary alloys provides more degrees of freedom in both composition and SRO for spectral extension. Since the smaller Si atoms help to balance the local lattice distortion induced by the large Sn atoms, overall SiGeSn alloys are more stable thermodynamically and can be better lattice-matched to the Ge buffer layer. With SRO, the stability and defect robustness can be further improved due to better accommodation of lattice distortion through local motifs. In fact, our recent first-principles computation modeling indeed indicates a notably higher vacancy formation energy in R-SRO and E-SRO SiGeSn than random alloys statistically. Details will be published separately. Further considering the strong impact of SRO on band structure engineering shown in Fig. 2 and Ref. 41, we envision that SiGeSn will offer a wide range of choices for high-performance MWIR detection. The minimal bandgap modeled for SiGeSn in Ref. 41 already reached ∼0.2 eV, similar to that of InSb. Lattice-matched Type-II SiGeSn heterostructures may also lead to Type II superlattices (T2SLs) for further spectral extension, as widely applied in their III–V counterparts.[262] Another advantage of these T2SL structures is similar to ICLs discussed in the lasers section, where defect states are outside the photon transition range as shown in Fig. 12. A possible approach to reach desirable SRO is to start with an ordered growth structure (e.g., short-period superlattices) and utilize the interdiffusion to our advantage to reach the desirable SRO, considering that they are thermodynamically favored. As discussed in Sec. II A, we could also control precursors or surfactants *in situ* or use He^+ ion implantation *ex situ* to modify SiGeSn SRO. We envision that this will be an active field of study for SiGeSn devices in the next decade.

Resolving the defect-related dark current density issue in GeSn will also open the door to more practical (Si)GeSn SWIR APDs. While a few reports on GeSn APDs have been published over the past decade, the Sn composition is still quite limited. Self-calibrated avalanche gain has only been demonstrated very recently, where photocurrent saturation after punch-through was used to undoubtedly calibrate the unity gain.[263] Further driving down the dark current will potentially allow high-performance GeSn SWIR APDs to operate under thermoelectric cooling (TEC) (e.g., at −60 °C) for imaging and LiDAR applications.

D. Image sensing

While not typically considered part of "silicon photonics" or "Si PICs," Si CMOS images sensors (CIS) are actually the most successful and the most widely used Si photonic devices. They revolutionized 2D imaging, which is practically incorporated in all mobile devices. Recent progress in quantum image sensor (QIS) further developed the remarkable capability of photon counting at room temperature in the visible spectral regime, representing the next generation of image sensors.[264] Instead of using avalanche gain as SPADs, QIS utilizes the simple principle that an appreciable voltage change (ΔV) can be measured if a single photoelectron (e^-) is transferred to a small capacitor (C) according to $\Delta V = e^-/C$. The small capacitance is naturally enabled by CMOS scaling to more and more advanced technology nodes, a perfect example of electronic–photonic synergy. For example, at 65 nm CMOS node, the capacitance of the n^+ floating diffusion (FD) node can be reduced to as small as C = 400 aF, meaning that a single photoelectron transferred to FD can induce a $\Delta V = 0.4$ mV.[265,266] By comparison, the readout noise at room-temperature is only ~0.1 mV, thanks to the advanced CMOS circuits and readout techniques such as correlated double samples (CDC) to cancel out kTC thermal noises. Therefore, single-photon counting can be achieved using Si QIS at room temperature. Compared to SPADs, QIS has advantages of high pixel resolution, orders of magnitude lower dark count rates ($0.1\ e^-/s$[265,266] vs $\sim 100\ e^-/s$[267] at 300 K), low voltage and power, room temperature operation, and standard foundry process of CMOS image sensors. The first commercial QIS product was debuted in 2021 by Gigajot, with an r.m.s. read noise as low as $0.16\ e^-$.[268] A very recent review on the evolution of Si CIS can be found in Ref. 269.

In addition to CMOS scaling enhanced photon counting sensitivity, another great advantage of CIS is that they can be programmed for sophisticated imaging functionalities. For example, recently high-speed, high signal-to-noise (SNR) ratio fluorescence imaging has been demonstrated using individually programmable pixels to control the sampling speed and phase of each pixel.[270] Such a sophisticated programmable readout is another great example of electronic–photonic synergy on Si CMOS platform, which can well be used in conjunction with machine learning (ML) for unprecedented imaging and analysis capabilities.

Considering the maturity, scalability, and high-performance of existing Si CIS and QIS platform discussed above, it is simply natural to consider riding on the wings of Si CIS/QIS by integrating other absorbing materials to extend the detection wavelength range beyond visible and near infrared regime (limited by the bandgap of Si). All we need to do is to transfer the photoelectrons to n-type storage wells (SWs) of Si CIS, and the rest is implemented by the Si CIS readout platform. Some implementations and visions for x-ray, UV, and infrared "CMOS+X" image sensors will be presented in this section, where "X" refers to the corresponding absorber material in each spectral regime.

Another emerging field for Si photonics is 3D imaging in LiDAR applications, allowing the devices to perceive, map, and interact with the surrounding world. Traditional LiDAR is a large and expensive system including discrete optical and mechanical components, such as sources, scanners, and detectors. In recent years, Si photonics has entered almost every aspect of 3D imaging, from Si modulators,[271] thermos-optic switch array,[272] beam steering module,[273] to Ge/Si SPADs (though low-temperature operation at 100 K)[274] and Ge photodetector arrays for coherent detection.[275] The ultimate goal is to achieve a compact LiDAR system by utilizing on-chip laser control, digital beam steering, and optical signal processing on Si PICs. The on-chip LiDAR will pave the way for large-scale implementation of 3D imaging in the same way that 2D CMOS image sensor disrupts the imaging industry. Such a LiDAR system will require optimization of all active photonic devices on Si PICs for system-level integration. Therefore, we will also discuss 3D imaging based on Si PICs for LiDAR applications at the end of this section.

1. Si CIS with extended wavelength range

To investigate the spectral extension of "CMOS+X" CIS, we have started with hard x-ray detection at photon energies >10 keV.[276,277] Hard x-ray detection has broad applications in biomedical imaging as well as monitoring dynamic processes in laser-assisted additive manufacturing. However, Si itself has very low absorption coefficient at >10 keV. Conventional solutions are (1) using higher atomic weight semiconductors such as CdTe. However, the level of pixel integration is far from that of Si CIS; (2) using x-ray scintillators, especially fast ones such as Lu_2SiO_5 (LSO) and $Lu_2Y_2SiO_5$ (LYSO) with a relatively short luminescence decay time of ~36 ns, to convert hard x ray into visible photons for Si CIS to detect. In this case, relatively thick (hundreds of μm), high-quality single crystals are required to absorb hard x-ray photons and convert them to visible/UV photons efficiently. Such a large thickness induces more crosstalk between Si pixels since light emitted from the thick scintillator could illuminate many pixels, reducing the spatial resolution.

To address these challenges, Fig. 21 shows a successful example of monolithically integrating a Bi_2Te_3 photon energy attenuation layer (PAL) on Si CIS for hard x-ray detection. Different from scintillators that convert incident x-ray photons to visible or UV photons, the high atomic number PAL attenuates the incident photon energy to a few keV on average, such that Si can absorb the downconverted x-ray photons much more efficiently. Consequently, the required thickness of the PAL downconversion layer is much thinner than that of regular scintillators. The high-Z PAL offers three major advantages: (1) Higher spatial resolution. Since the thickness of PAL is of the order of 100 nm to 1 μm, i.e., ~3 orders thinner than LYSO or LSO scintillators, the crosstalk between pixels is drastically reduced when detecting downconverted photons, and the spatial resolution is increased correspondingly; (2) High speed as a result of fast photoelectron generation and Compton scattering within $\ll$10 ns in x-ray photon energy downconversion process in PALs, compare to ~36 ns visible light luminescence decay time in LYSO scintillators; (3) Convenient integration by directly depositing polycrystalline or even amorphous high atomic number PALs on Si CIS pixels. The energy downconversion is mainly attributed to the x-ray photon scattering with inner core electrons of the heavy element atoms in the PAL layer; therefore, crystallinity is no longer required. This is a notable advantage compared to expensive single-crystalline LYSO scintillators.

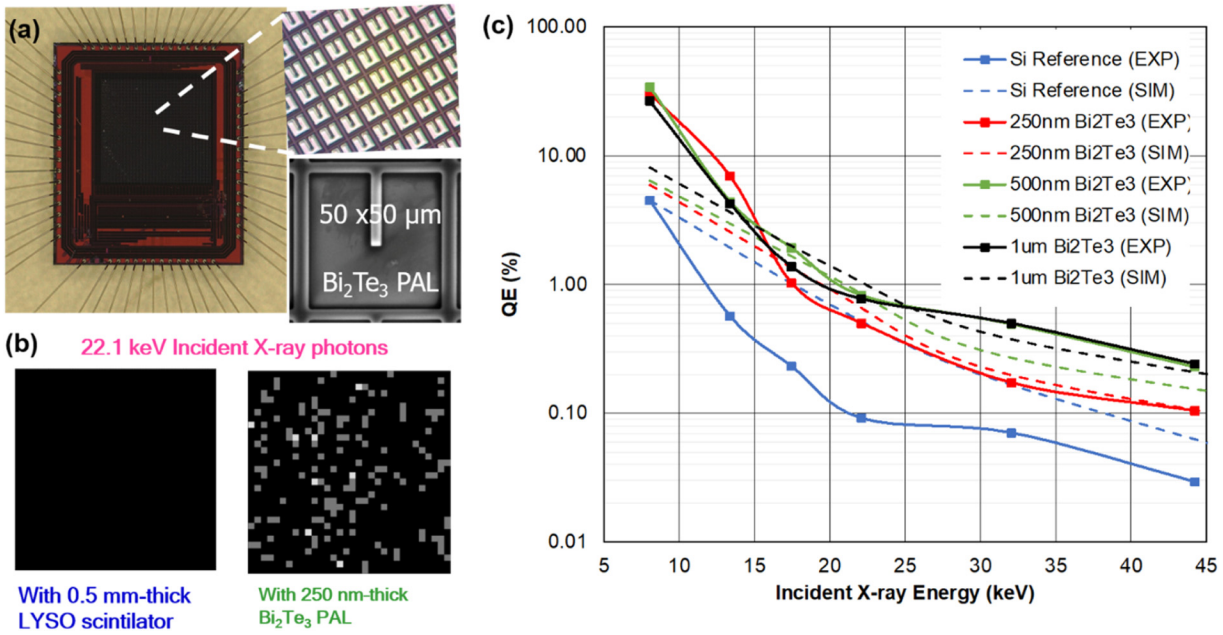

FIG. 21. (a) A photo of a Si CIS chip integrated with a 250 nm-thick Bi_2Te_3 PAL layer for enhanced hard x-ray detection. The corresponding optical microscopy (top right) and scanning electron microscopy (SEM, lower right) images show a 32 × 32 array of 50 × 50 μm^2 pixels in this prototype chip. (b) Comparison of 22.1 keV x-ray photon detection events under the same exposure time for a reference Si CIS chip covered with 0.5 mm-thick LYSO scintillators vs the one in (a) (integrated with a 250 nm-thick Bi_2Te_3 PAL). Each pixel in white detected two x-ray photons, while each gray one detected one x-ray photon. (c) Experimentally measured vs theoretically modeled quantum efficiency as a function of incident photon energy. Figures reproduced and regrouped from Eldred Lee, Kaitlin M. Anagnost, Zhehui Wang, Michael R. James, Eric Fossum, and Jifeng Liu, Instruments **5**, 17 (2021). Copyright 2021 Author(s), and Eldred Lee, Kevin D. Larkin, Xin Yue, Zhehui Wang, Eric R. Fossum, and Jifeng Liu, Instruments **7**, 24 (2023). Copyright 2023 Author(s), licensed under a Creative Commons Attribution (CC BY) license.

As shown in the demonstration in Fig. 21(b),[277] a 250 nm-thick Bi_2Te_3 PAL/Si CIS detected many more x-ray photons at 22.1 keV than a Si CIS reference chip covered with a 0.5 mm-thick LYSO crystal under the same exposure time. Part of the reason is that, while LYSO converts x-ray photons to blue photons at $\lambda = 420$ nm at a yield of ~30 photons/keV, Si tends to have lower quantum efficiency at 420 nm due to very shallow absorption depth and susceptibility to surface recombination. Another issue is the total internal reflection within the thick LYSO crystal, which drastically decreases photon coupling into Si CIS. Therefore, this comparison demonstrates that Bi_2Te_3 PAL is more efficient in boosting hard x-ray detection efficiency of Si CIS than LYSO, and it is much easier to fabricate and integrate on Si CIS chips. Figure 21(c) further shows that Si CIS chips integrated with Bi_2Te_3 PALs exhibit ~10× improvement in external quantum efficiency compared to a reference image sensor without PAL layers at incident x-ray photon energy range of 10–40 keV.

An important implication from the success of hard x-ray Bi_2Te_2 PAL/Si CIS is that the same approach applies to any photon upconversion or downconversion layers that can be directly deposited on Si, thereby greatly extending the spectral response of Si CIS.

In addition to integrating upconversion/downconversion layers, another important approach for spectral extension of Si CIS is to transfer photoelectrons from BEOL integrated UV/IR absorber layers directly to the storage well of Si pixels. As an example, Fig. 22(a) shows device modeling of GeSn (11 at. % Sn)/Si CIS for SWIR and MWIR detection. In this case, GeSn can be directly crystallized on Si using the BEOL processing techniques discussed in Sec. II B 2. The p^+ Si pinning layer is changed into an interdigitated finger structure, such that electrons and holes generated in GeSn will be collected to the p+ Si region (ground) and n-Si storage well, respectively. The modeling in Fig. 22(a) shows the electron and hole concentration distribution in the devices upon 50 mW/cm^2 excitation at $\lambda = 2050$ nm. The photoelectron concentration generated in GeSn can reach 10^{16}–10^{17} cm^{-3}. When a reverse bias of −1 V is applied upon readout between p^+ Si and n-Si lateral junctions, the extraction of photoelectrons from GeSn is even more efficient, as shown by the darker red shades in the GeSn and N–Si regions due to the enhanced transport of photoelectrons from GeSn to N–Si. Similarly, holes can be smoothly transported to p^+ Si regions in the two panels on the right. We also note that we adopted a residual p-doping of 5×10^{17} cm^{-3} in the GeSn region due to defects to model the material quality in practical device fabrication, and the modeling in Fig. 22(a) shows that this does not significantly impact the photoelectron collection. Recently, we have experimentally demonstrated some prototype devices based on the structure in Fig. 22(a), with a low dark current density of 10 μA/cm^2 at room temperature and 60 nA/cm^2 upon TEC cooling to −60 °C.

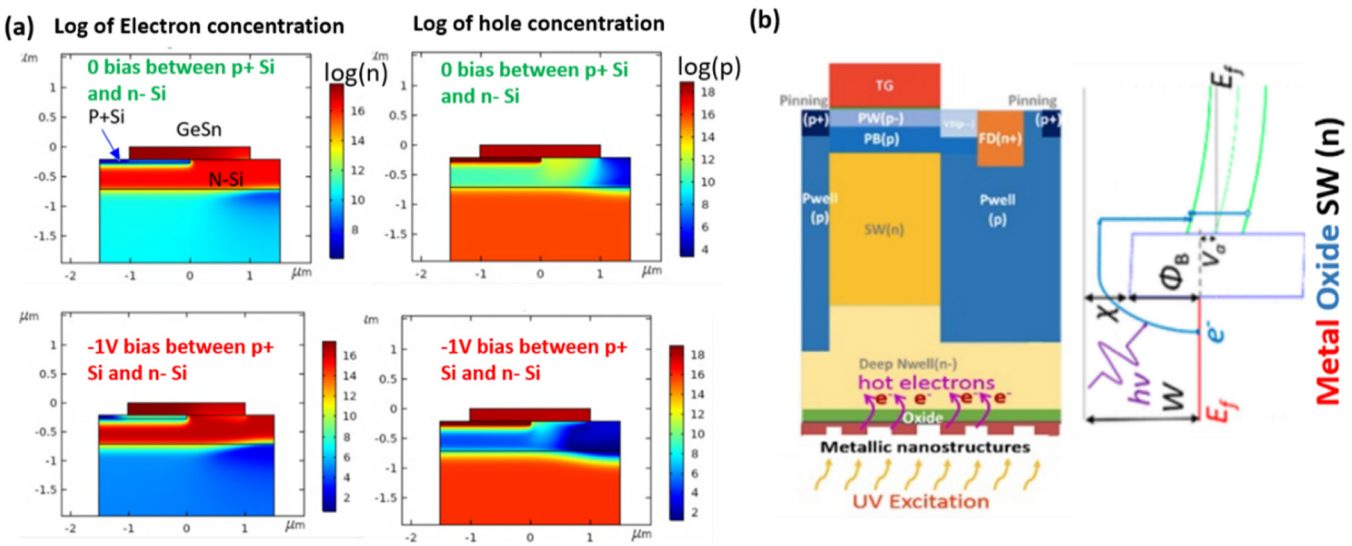

FIG. 22. (a) Device modeling of a GeSn/Si CIS showing electron and hole density distribution in log scale under 50 mW/cm^2 excitation at $\lambda = 2050$ nm. (b) illustrates a nanophotonic metal–oxide–semiconductor (MOS) structures on the backside of QIS for solar-blind UV detection.

Imaging at 1850 nm wavelength has been demonstrated using a 32×32 GeSn/Si CIS pixel array. Details of the results will be reported in a separate paper.

Furthermore, solar-blind UV QIS can be achieved by utilizing UV-excited hot electrons in a nanophotonic metal–oxide–semiconductor (MOS) structure, as shown in Fig. 22(b). The metallic nanostructures act as nano-antennas to concentrate UV light, as well as internal photoemission emitters, where hot electrons are excited by UV photons across the metal/oxide interfacial barrier Φ_B[257] to reach the electron SW in each QIS pixel for readout. The metal/oxide interfacial potential barrier height is used to tune the UV response range and block solar-excited photoelectrons. The metal nanostructures can be fabricated by nanolithography or self-assembly. These implementations are under active investigation and development.

Overall, we envision that the next era of advanced CIS and QIS will provide a universal platform for diverse wavelength ranges through BEOL integration of various photon energy upconversion and downconversion layers, as well as different absorbers that transfer photoelectrons into Si pixels. It potentially represents a paradigm shift in multispectral imaging.

2. Toward 3D LiDAR imaging

The lightweight, compact, and cost-effective on-chip LiDAR should be the ultimate answer to the ubiquitous deployment of 3D imaging, in the same way that the CMOS camera revolutionized 2D imaging. In contrast to widespread 905 nm lasers typically employed in commercial LiDAR systems, 1550 nm lasers exhibit a higher permissible optical power for eye safety and longer range applications, as well as compatibility with readily available Si photonic devices and circuits. In recent years, Si photonics technology has penetrated the LiDAR applications from various integration levels.[278,279] For example, Aeye uses a microelectromechanical systems (MEMS) mirror system made of monocrystalline silicon in its time-of-flight (TOF) measurement architecture, which enables vehicle detection at a distance of 1000 m and finds applications in autonomous driving.[280] The innovation of other start-ups (such as Analog Photonics,[281] Aeva, Voyant Photonics, SiLC,[282] Tower Semiconductors,[283] and Pointcloud[284]) lies in the FMCW approach to capture the depth information, where the frequency of the FMCW source is linearly chirped, and the reflected signal is mixed with the reference local oscillator on the coherent receiver to detect the beat frequency. As summarized in Fig. 23, different combinations of Si PIC technologies have been implemented, yet there is no clear winner so far. The successful technologies to gain market are based on the right combination of existing technologies and alignment with applications and costs (Fig. 23).

In this section, we will briefly discuss and evaluate the current status of active photonic devices in Si PICs for the key technologies for LiDAR applications:

a. Laser wavelength. While lasers around 900 nm provide high power and high efficiency from a pure optical point of view, 1550 nm sources are undoubtedly advantageous in terms of eye safety. In fact, eye safety standard IEC 60825-1[285] limits the power of 905 nm laser and the maximal distance. Longer wavelengths in the SWIR regime (1700–2000 nm) help penetrate through haze and fogs,[108,109] and they also have high reflectivity on dark/black objects in the visible regime. However, the laser efficiency and photodetectors' detectivity both drop at longer wavelengths. Therefore, we envision that an intermediate wavelength at 1550 nm will be the most reasonable choice at least in the near future. Commercial development of high-power 1550 nm pulse laser for the ToF system has also achieved notably progress in recent years.[286] Other relatively eye-safe

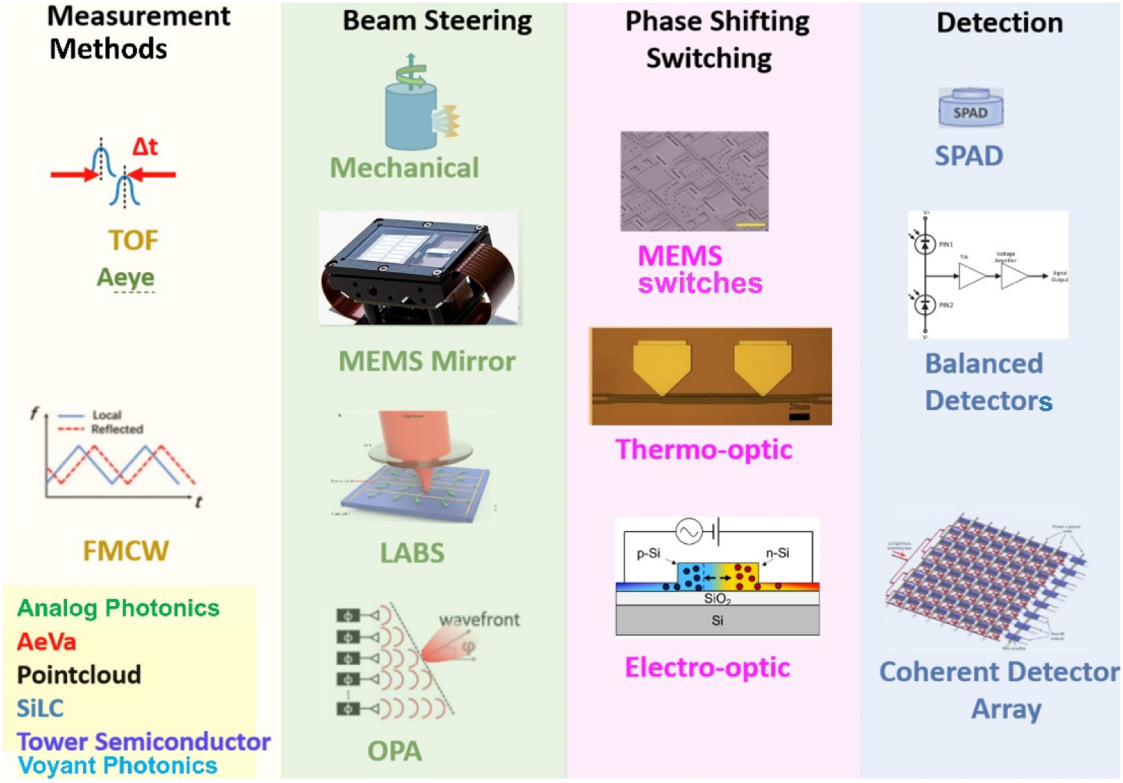

FIG. 23. Summary of available LiDAR systems based on different methods of ranging, beam steering, phase shifting/switching, and detection. Various combinations have been implemented by many companies, some of which are listed in the first column. The MEMS mirror micro-scanner figure was reproduced with permission from https://commons.wikimedia.org/wiki/File:Fraunhofer_IPMS_Mikroscanner-Module.jpg. Copyright 2011 Positiveimpact, licensed under a Creative Commons Attribution (CC BY) license. The LABS and MEMS switches figures were reproduced with permission from Xiaosheng Zhang, Kyungmok Kwon, Johannes Henriksson, Jianheng Luo, and Ming C. Wu, Nature **603**, 253–258 (2022). Copyright 2022 Author(s), licensed under a Creative Commons Attribution (CC BY) license. The thermo-optic phase shifter figure was reproduced with permission from B. Pant, W. Zhang, M. Ebert, X. Yan, H. Du, M. Banakar, D. T. Tran, Y. Qi, D. Rowe, V. Jeyaselvan, C. G. Littlejohns, G. T. Reed, and D. J. Thomson, Opt. Express **29**, 36461–36468 (2021). Copyright 2021 Author(s), licensed under a Creative Commons Attribution (CC BY) license. The electro-optic phase shifter figure was reproduced with permission from Y. Kim, J.-H. Han, D. Ahn, and S. Kim, Micromachines **12**, 625 (2021). Copyright 2021 Author(s), licensed under a Creative Commons Attribution (CC BY) license. The balanced photodetector figure was reproduced with permission from Rui Wang, Lian Chen, Yiming Zhao, and Ge Jin, Rev. Sci. Instrum. **91**, 073101 (2020). Copyright 2020 AIP Publishing LLC. The coherent detector array figure was reproduced with permission from R. Nicolaescu, C. Rogers, A. Y. Piggott, D. J. Thomson, I. E., Opris, S. A. Fortune, A. J. Compston, A. Gondarenko, F. Meng, X. Chen *et al.*, Proc. SPIE **11691**, 116810G (2021). Copyright 2021 SPIE.

wavelengths with lower solar radiation background, e.g., 1350 nm (close to O-band lasers) or 1400 nm (closer to 1480 pump lasers widely used in telecommunications), can also be considered for ToF systems with higher efficiency/lower cost than 1550 nm sources. SWIR lasers may get into the application if both high-performance lasers and high detectivity detectors are achieved.

b. ToF vs FMCW. While there is an on-going debate on which system is better for automobile LiDAR systems, here we focus on which one would benefit more from Si PIC platform. For ToF, the required components are relatively simple, so they can well be implemented using compact packaging of high-performance discrete devices, such as high-power pulsed lasers and high-speed ToF photodetectors. In particular, the development of high-power, high-efficiency, single-mode PCSELs can well cover the needs of ToF LiDAR systems using dually modulated PCSELs (DM-PCSELs).[287] The system comprised a ToF camera, a flash DM-PCSEL for broad angle illumination, and a complementary beam-scanning source simply based on a DM-PCSEL array to enhance the detection of low-reflectivity objects. Low-threshold PCSELs emitting at 1550 nm have also been demonstrated very recently.[288] Overall, there is not a strong motivation to bring all the pulse laser and detector components on the same chip for ToF applications, considering that their fabrication processes are drastically different, and integration on Si does not seem to provide significant advantages.

Therefore, we envision that Si photonics is more suitable for FMCW. FMCWs are sometimes referred to as "Gen 2" in LiDAR systems in that coherent optics provides many advantages, such as higher SNR at longer distance, rejection of background optical noise, direct velocity measurements (in the direction of driving), no

interference from other LiDAR beams, etc.[278] However, the system is also more complicated to implement, with many components for chirp control, beam splitters, optical amplifiers, phase shifters, optical antennas, coherent detectors, etc. This is where dense integration of sophisticated optical components on Si PIC could provide lower cost and higher scalability toward practical commercial applications.[289]

c. Photodetectors. Existing Ge/Si photodetectors, including APDs and waveguide-integrated ones, can well be applied to LiDAR Si PICs. For the 1550 nm laser, waveguide-coupled detectors used in OPA and FPSA systems can also benefit from a long optical absorption path length to achieve high quantum efficiency.[274] On the other hand, Artilux has collaborated with Taiwan Semiconductor Manufacturing Company (TSMC) demonstrating Ge/Si lock-in pixels for indirect ToF systems.[290] In the lock-in pixel approach, the noise is no longer limited by the dark current, but the ambient optical background (sunlight or other laser source), thereby overcoming the disadvantage of Ge/Si detectors in terms of dark current compared to InGaAs. As discussed earlier, the performance of Ge/Si APDs have already exceeded III–V in bandwidth-gain produce for 1310 nm light sources, and it has been investigated for LiDAR applications in recent years.[291] The responsivity at 1550 nm can be enhanced via tensile-strain engineering or a few percent of Sn alloying. In fact, recently, the response of Ge/Si photodetectors in the L-band has already caught up with InGaAs with tensile-strain enhancement.[175] Overall, the development of Ge/Si photodetectors for 2D or 3D imaging applications is in an early stage, lagging behind their deployment in data communications. This could become a promising area of growth in the near future.

d. OPA vs FPSA. As discussed earlier in Table III, OPA[292–294] and FPSA (also known as "lens-assisted beam steering (LABS)"[295,296]) are the two leading beam steering solutions for FMCW systems. A major difference between the two is that the former uses a wave optics approach for beam forming, while the latter is more of a geometrical optics approach similar to the reversal usage of a camera. As discussed at the end of Sec. III B 4, OPA requires phase shifting induced by Δn, while FPSA/LABS only requires intensity switching, which can synergistically utilize both Δn and Δk changes. In both cases, all solid-state beam steering (without moving parts) faces strong competition with integrated MEMS-activated phase shifters for OPA and switches for FPSA.[230,297] Therefore, advancing high-performance EO/EA materials and device structures, as listed in Table III, are the key factors to future success of all solid-state LiDAR systems. For example, the demand of small beam divergence and large beam steering range of on-chip LiDAR systems requires large arrays of closed-packed optical antennas and corresponding phase shifter. This could drastically increase the power consumption to the order of Watts[298,299] based on existing thermo-optical phase shifters. By comparison, the power consumption of 25 600 (160 × 160) MEMS phase shifters is only 69 μw (2.7 nW/component at 12 V driving voltage).[297,300] Replacing thermo-optical phase shifters with high EO coefficient materials for OPAs, and with EAM switches for FPSA systems will not only drop the potential power consumption well below 1 pJ/(phase shifter or switch) but also achieve ultrafast 3D LiDAR imaging at tens of GHz,[301] as has been demonstrated in their respective modulators.

We also envision that FPSA will gain more momentum in the next decade compared to OPAs in beam steering since they are naturally 2D arrays for high scalability. The switching is binary ("on" and "off") similar to EAMs, which facilitates optical calibration and electrical control. As mentioned earlier in Sec. III B 4, ultrafast (tens of GHz), ultralow energy (fJ/switch) can potentially be offered by EAMs utilizing both Δn and Δk to enhance the extinction ratio. FPSA is also a great example transferring the concept of image sensor systems to Si PICs (in the reversed direction of optical path). These two sides of "Si photonics" can greatly support each other. This will be further discussed in the outlook section next.

IV. OUTLOOK: POTENTIAL SYNERGY BETWEEN Si CIS AND Si PICS

While Si CIS and Si PICs are independent of each other in their origins and historical development, we envision future synergies between these two powerful optical technologies on one Si platform. In terms of integration density, Si CIS has already achieved tens of millions of photodetectors (pixels) per chip, far exceeding the level of photonic devices integration on Si PICs so far. Therefore, it is instructive to borrow some concepts from CIS to advance future developments of Si PICs. Some key concepts and technologies from the two can benefit each other. In this outlook, we only raise a few examples hoping to inspire more innovative ideas from the readers in both communities.

A. From megapixel Si CIS to mega-transceiver Si PICs

Most of the Si PICs adopt waveguide-optical fiber edge coupling schemes for photonic I/Os. However, this approach only uses the peripheries of the chips, while the I/O density is limited by the diameter of the optical fibers, typically with a core diameter ~10 μm and core-to-core spacing ~100 μm for single-mode fiber ribbons.[302] Therefore, all four edges can accommodate ~1000 optical fiber I/O at the most for a 1 in. square microchip. While WDM can increase the effective optical I/O density by multiplying the wavelength channels, it also adds more complexity.

Considering that 3D memory stacking via TSV has greatly expanded electronic interconnect capability, we may ask: can we transfer similar ideas to optical I/O by utilizing the entire surface area of Si PICs for ultrahigh capacity chip-to-memory and chip-to-chip photonic data links?

Translating megapixel Si CIS to "megapixel"-transceivers on Si PICs may provide a promising path toward this goal. Considering a transceiver "pixel" footprint on the order of 20 × 20 μm^2, fitting a mega-transceiver array on a microchip (a few cm^2) is perfectly feasible. Even if we only use a relatively low data rate of 1 Gb/s per transceiver pixel, it will offer 1000 Tb/s capability, nearly two orders higher than state-of-the-art optical I/O based on Si PICs with edge coupling.[22,77,78] The data capacity is still remarkable even if we leave a margin of 1 order of magnitude in either transceiver density or data rate per transceiver pixel, which allows us to get a balance between datalink capacity and power consumption.

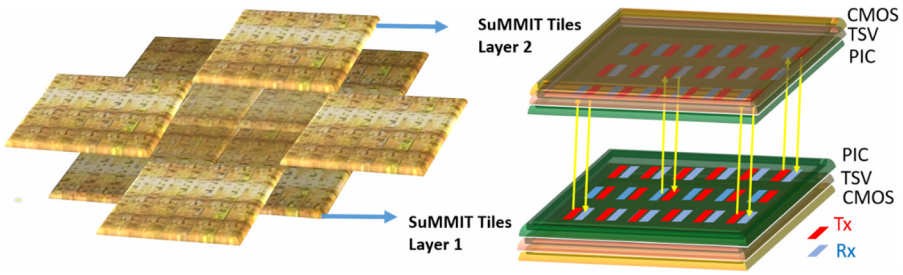

FIG. 24. Schematics of "megapixel"-transceivers on Si PIC based on SuMMIT architecture (see Fig. 6). Each chip in a SuMMIT tile layer (e.g., the one in the center of layer 2) directly communicates with four chips in the other layer through vertically overlapping quarters. Each module in the figure can be considered a computing-cluster accelerated by photonics (CAP), whose edges can be coupled to fibers to communicate with other CAPs.

The SuMMIT electronic–photonic integration platform discussed earlier in Sec. II B 2 can be adapted to implement such "megapixel" transceiver arrays, as schematically shown in Fig. 24. Analogous to the architecture of BSI image sensors, in SuMMIT, the PIC layer is inverted and bonded to the CMOS electronics layer via TSV, enabling high-density optical I/O in the same way as high-density imaging pixels. As mentioned earlier, SuMMIT also leverages existing metal contact layers to enhance optical coupling efficiency from/to grating couplers for 2D vertical optical coupling. Alternatively, optical free-form couplers for high-density integrated photonics (OFFCHIP) could also be applied in this case, which has demonstrated broadband, low-loss vertical coupling 2D fiber arrays.[84,303] In those demonstrations, the density of the free-form coupler array was only limited by the size and spacing of single-mode fibers. Since the free-form coupler design is based on geometrical optics, it can be readily adapted to achieve 2D collimated beams for the transceiver pixels in Fig. 24. For better isolation between transceiver pixels to reduce crosstalks, a layer of microlenses/metalenses could be also added between the two layers of PICs in Fig. 24.

At a relatively low data rate <10 Gb/s per transceiver pixel, one could even consider HI of VCSEL arrays on the SuMMIT platform since the dynamic power consumption is low, of the order of 10 fJ/bit.[304] For higher data rate/pixel, surface-incident EAMs discussed earlier in Sec. III B 3 could be applied due to ultralow power consumption down to a few fJ/bit. Another advantage is that the same EAM structure can also be directly used as the photodetector on the receiver side. In the example in Fig. 24, each chip in a SuMMIT tile layer (e.g., the one in the center of layer 2) directly communicates with four chips in the other layer through vertically overlapping quarters at ~250 Tb/s, based on previous estimation on the transceiver pixel density and 1 Gb/s per transceiver.

The fundamental limiting factor for the scale of the transceiver pixels would be on-chip power density, rather than physical I/O density. For example, at 10 fJ/bit per transceiver, the power consumption per chip would be 10 W at 1 Gb/s for a mega-transceiver array. Further increasing the data rate is perfectly feasible, but it would also require a dramatic reduction in the energy/bit for the transceivers, considering that the power density usually cannot exceed 100 W/cm^2 for microchips (note that this is already equivalent to 1000× solar power concentration).[305]

Each module shown in Fig. 24 can be considered a computing-cluster accelerated by photonics (CAP). Note that the edges of each CAP are still fully available for conventional optical fiber coupling to other CAPs. Therefore, they can be readily organized into a high-performance computing network. We envision that lots of metadata are generated and communicated within each CAP between the microprocessors and memories, such that the densely pixelized photonic I/O can be fully utilized. Between the CAPs, the main data transfer would be final computational results from each subtask undertaken by each CAP; therefore, the total amount of data would be much less than the metadata and can be handed efficiently by edge photonic I/Os. This way, dataflow in the high-performance computing network can be processed in an energy-efficient manner.

B. Transferring data from Si CIS high-speed cameras using to mega-transceiver Si PICs

The progress of ultrafast, ultrahigh resolution imaging may also lead to a synergy between Si CIS and Si PICs. Currently, Si CIS/QIS chips have evolved to ~50 megapixels.[269,306] To capture and monitor ultrafast processes for different biomedical and industrial applications (e.g., laser-assisted additive manufacturing), ultrafast imaging at ~100 Mfps is being investigated.[307] If we want both high-resolution and high-speed simultaneously, we are talking about up to 5000 Tb/s data rate, which is currently the bottleneck for continuous ultrafast imaging. Even though the development of edge computing and in-sensor computing might be able to screen the data and reduce this requirement by 2–3 orders of magnitude, the required data rate is still of the order of Tb/s. Si PIC is the only solution to address this issue. Therefore, if we replace a layer of microprocessor or memory chips with those for ultrafast imaging in Fig. 24, it would be the best solution to get the data off the camera chip. We also note that the data rate offered by a transceiver pixel on Si PIC (10–100 Gb/s) is usually much higher than that from a CIS pixel (<1 Gb/s for hundreds of Mfps). Therefore, a transceiver "pixel" in Fig. 24 can potentially transfer data from multiple CIS pixels. This helps us to relieve some of the footprint constraints on the transceiver side.

C. Si CIS as waveguide-coupled detectors for Si PIC biosensors

Beyond imaging, low-cost megapixel arrays of Si CIS with ultralow noise (e.g., ~0.2e$^-$ read noise and 0.1 e$^-$/s dark count rate for Si QIS, as discussed earlier in Sec. III D) also offer a unique opportunity to integrate with Si PICs for ultrahigh sensitivity molecular sensing through waveguide-enhanced fluorescence and Raman spectroscopy. Coupled with microfluid channels, they

enhance near-field optical coupling with molecules captured on the surface or within the slots of the waveguides, thereby greatly suppressing the background noise from the bulk of the fluid.[308,309] To achieve single molecular detectivity, though, photodetectors with high responsivity and low noise are needed. While Ge/Si photodetectors are the standard components in Si PICs for data communication, their dark current is too large for single molecule sensing. Si CIS/QIS are much better choices since they not only offer photon counting capability at room temperature but also an almost free bank of detectors on the scale of millions, far exceeding the level of integration of any Si PIC demonstrated so far for either communication or biosensing applications. Therefore, a promising solution would be HI of molecular sensing Si PICs with Si CIS/QIS chips via evanescent coupling. In this case, the waveguides carrying the fluorescence or Raman signals on the Si PIC can meander on top of Si CIS for evanescent coupling, utilizing all the pixels along the optical path as low-noise photodetectors for ultrahigh sensitive single-photon detection. Especially for relatively weak Raman signals, such an approach not only uses the photon counting capability of each individual pixel but also hundreds or thousands of them in series to capture any signal transmitted through the waveguide. On-chip optical filters on Si PICs[310] can be utilized to filter out the pump laser and its sidebands, which has already been utilized in microwave integrated photonics. If on-chip spectrometry is available on the Si PIC,[311] different wavelengths can also be coupled to different rows or columns of the Si CIS to generate a full spectrum directly. In fact, Si CIS provides so many pixels that a small fraction of them are already sufficient to detect all signals from a given wavelength. Therefore, it can easily accommodate the resolution scaling of the on-chip spectrometers.

Similarly, once IR absorbers such as GeSn are integrated on Si CIS, they can also be readily applied for IR absorption spectroscopy. A Si CIS chip with both Si and IR absorber pixels would potentially be able to measure fluorescence, Raman, and IR absorption spectra simultaneously, thanks to the huge detector bank provided by Si CIS platform, thereby achieving unprecedented capability in molecular sensing on a small Si PIC/CIS chip module.

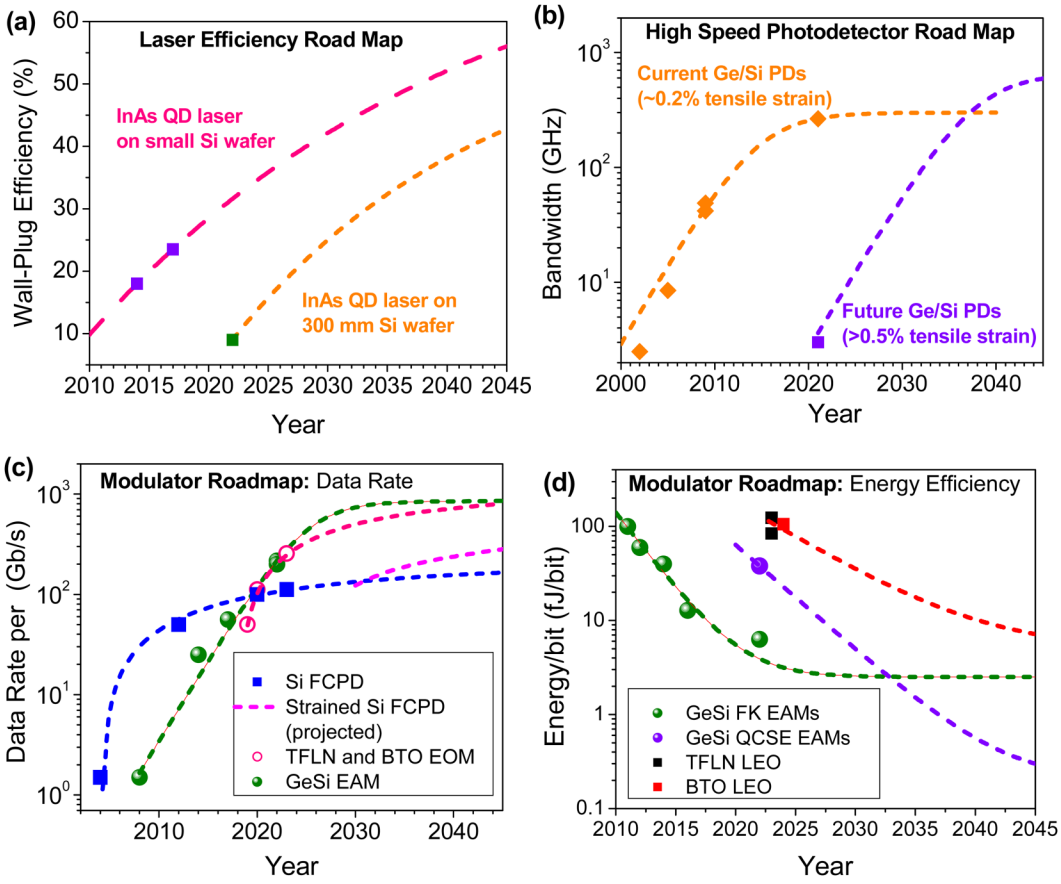

FIG. 25. Roadmaps for (a) on-chip laser WPE; (b) photodetector bandwidth; (c) modulation data rate (per channel); and (d) modulator energy efficiency. The scattered symbols represent existing experimental data. The dashed lines represent the projection of future development, as explained in the main text.

V. ROADMAP OF ACTIVE PHOTONIC DEVICES

Based on the perspectives discussed in Secs. I–IV, in this section, we will present a brief roadmap for some of the emerging active Si photonics devices. The device performance roadmap in Fig. 25 is forecasted by fitting the trend of development over the past two decades. New photonic devices usually experience rapid growth in the first decade or two, then eventually saturate due to physical limitations of a given material system and the corresponding working mechanisms. Depending on whether the initial stage shows an exponential or linear growth behavior, the curve fitting either uses a logistic function or a saturating exponential function (i.e., similar to the ones describing charging/discharging capacitors). For emerging active photonic devices that are still growing rapidly, we project that they will largely mature and approach their physical limits in two decades (i.e., by 2045) based on previous examples such as Si FCPD modulators and Ge/Si photodetectors.

Figure 25(a) shows the roadmap for on-chip laser WPE. As discussed in Sec. III A, this is an important factor to further improve the energy efficiency of photonic chips. Currently, InAs QD lasers have routinely reached ∼25% WPE at room temperature,[312] with excellent thermal stability to maintain >20% WPE up to 85 °C. Considering that 56% WPE has been demonstrated near 1300 nm wavelength for InAs QD lasers on GaAs,[94] the roadmap projects an improvement to >35% WPE in the coming decade and approaching 60% by 2045. For 300 mm wafer-scale QD laser integration, optimization of the pocket growth is projected to improve the WPE beyond 30% by 2035.

Figure 25(b) shows a roadmap of high-speed photodetectors for Si photonics. After an exponential growth between 2000 and 2010, the bandwidth of Ge/Si photodetectors reached 265 GHz by 2021,[237] approaching its physical limit. Further enhancing tensile strain beyond 0.5% using SiN_x stressors[175] is a promising approach to push the bandwidth toward 400 GHz in the next two decades. On one hand, increasing tensile strain will further increase the absorption coefficient of Ge in C and L bands, allowing for shorter waveguide-coupled photodetectors to reach the same quantum efficiency with lower capacitance and higher RC-limited bandwidth. On the other hand, higher tensile-strain lifts the light-hole band above the heavy-hole band such that the hole mobility is enhanced to improve the transit-time limited bandwidth. We, therefore, envision another ∼2× improvement in Ge/Si photodetector bandwidth through strain engineering by 2045, i.e., reaching 400–500 GHz regime. This projection also aligns with the 2024 Integrated Photonics Systems Roadmap International (IPSR-I 2024) for Si photonics[313] suggesting 300–400 GHz bandwidth for p-i-n photodiodes on Si PICs by 2040. While graphene photodetectors have demonstrated >300 GHz bandwidth as a strong competitor,[314] the lack of a bandgap in graphene also dramatically increases the dark current. Therefore, we are not yet incorporating them into the photodetector roadmap for Si PICs.

Figures 25(c) and 25(d) show the modulator roadmaps in terms of modulation data rate (per channel) and energy efficiency. While conventional Si FCPD modulators are reaching a saturation in bandwidth/data rate in the 2020s, strain engineering discussed in Sec. III B 1 b coupled with the slow light effect[315] can potentially further boost the performance toward 200 Gb/s. Notably, GeSi EAMs demonstrated an exponential increase in data rate and decrease in power consumption over the past decade, representing the most promising intensity modulation mechanism on Si platform. LEO modulators based on TFLN and BTO also achieved rapid progress in bandwidth in the past decade. FK/QCSE EAMs as well as LEO modulators are based on field effects with sub-ps intrinsic response time, yet power-efficient high-speed electronics for modulator drivers to reach Tb/s still constitutes a big challenge. While we noted a very recent demonstration of >1 THz bandwidth plasmonic EO modulators by feeding THz sinusoidal waves generated from external sources into the device (similar to microwave photonics),[316] THz sinusoidal wave generators are very different from modulator drivers for photonic datalinks at >1 Tb/s data rate. We, therefore, set an upper limit of 900 Gb/s by 2045 for EAMs and LEO modulators, limited by electronics rather than photonics. The corresponding projection in Fig. 25(c) is also largely consistent with the projection of IPSR-I 2024 for Si photonics,[313] i.e., >800 Gbaud symbol rate by 2040. In terms of energy efficiency in Fig. 25(d), GeSi FK EAMs have already demonstrated low-power consumption on the order of 10 fJ/bit. Further development will push the energy efficiency toward 1 fJ/bit in the coming decade. With enhanced electro-absorption effect in QCSE, sub 1 fJ/bit is expected for high-bandwidth QCSE EAMs within a decade or so. For LEO modulators, the power consumption is expected to drop by one order or magnitude from ∼100 fJ/bit of current devices to ∼10 fJ/bit in the next decade with new material and processing development.

Another note is that the phase modulation efficiency $V_\pi \cdot L$ is evolving faster than the prediction of IPSR-I 2024. The goal of 0.05 V cm for 2030 has already been reached by GeSi QCSE phase modulators ($V_\pi \cdot L = 0.036$ V cm)[227] and plasmonic BTO modulators ($V_\pi \cdot L = 0.014$ V cm).[197] Therefore, we expect 5–10 years ahead of the goals of IPSR-I 2024 for phase modulation efficiency, i.e., achieving $V_\pi \cdot L < 0.01$ V cm by 2030–2035 instead of 2040.

Last but not least, scalability, yield, and uniformity are important factors for Si photonics, especially for the emerging active photonic materials and devices. With the development of photonic foundries (AIM Photonics, IMEC, etc.), key active photonic devices such as Si FCPD modulators and Ge/Si photodetectors are now successfully scaled to 300 mm wafers with high yield and uniformity for routine MPW runs.[16,17] We note that these developments for full integration onto 300 mm Si/SOI platform took approximately 15 years to implement from the first lab demonstration. Emerging devices discussed in this Perspective, such as InAs QD lasers and GeSn photonic devices, are also being demonstrated on 300 mm Si platform in recent years.[110,317] Based on the historical development of photonic integration, we expect that they will become mature to a similar level of yield and uniformity as Si modulators and Ge photodetectors nowadays by 2040.

VI. CONCLUSIONS

In conclusion, this paper has discussed recent progress and shared perspectives on future development of active photonic devices on Si PICs, from emerging materials to integration schemes, for data communications and optical sensing applications. We also explored synergies between Si PIC and Si CIS platforms that could mutually benefit each other and provided a roadmap for

future development of major active photonic devices based on the trend of development over the past two decades.

For emerging active photonic materials on Si PICs, we introduced very recent discoveries of atomic SRO engineering in the SiGeSn system in Sec. II A, potentially offering a new degree of freedom for band engineering beyond composition and strain. Interestingly, in the SiGeSn system, what matters to a great extent is not only the average Sn composition but also the distribution of Sn atoms in terms of their atomic neighboring environment. Engineering atomic ordering in SiGeSn potentially offers full-spectral coverage from SWIR to LWIR with a minimal bandgap of several meV at a low average Sn composition <10 at. %. It also enables a variety of lattice-matched, iso-compositional SiGeSn Type-I and Type-II QWs for high-performance MWIR lasers and photodetectors on Si platform for a variety of sensing/imaging applications. We envision that future development in SRO engineering will greatly enrich and enhance the functionalities of SiGeSn active IR photonic devices for Si PICs.

BEOL processing toward 3D Si PICs is at the frontier of research for new integration schemes. Such capability will not only enable large-scale integration of many high-performance active photonic materials (e.g., LN, BTO, PCMs, magneto-optical materials, etc.) but also boost the density and functionality of Si PICs. Under BEOL HI schemes discussed in Sec. II B 1, emerging "grafted" III–V/tunneling oxide/Si heterojunctions exhibit almost ideal I–V, potentially offering the best of both III–V and Si for high-performance photonic devices (e.g., grafted III–V/Si APDs) without lattice-mismatch issues. Furthermore, analogous to the concept of BSI Si CIS, SuMMIT architecture inverts the photonic layer and exposes the active photonic device regions on the surface for facile BEOL integration of novel photonic materials, such as BTO, garnets, PCM, and SiGeSn, leveraging local heating capability provided by standard Si PICs for local processing without affecting the metal contacts in the surrounding area. For monolithic BEOL integration, recent progress in low-temperature epitaxy of Ge/Si photodetectors and direct crystallization of GeSn on Si are both promising to reach the performance of their FEOL processed counterparts, facilitating 3D photonic integration.

We then discussed emerging trends of active photonic devices on Si PICs. For laser sources, we envision two competitive paths: (1) a high-performance off-chip laser efficiently generating an on-chip frequency comb and (2) high-performance QD/QDash on-chip lasers. Both paths have achieved dramatic progress in recent years. For some applications such as wearable photonic chips for biosensing, though, on-chip lasers sources are ideal. III–V/Si QD lasers in O-band have reached 300 mm wafer-scale integration, while the pocket growth approach could be further optimized to improve the material quality and device performance. Recent progress in MOCVD growth of QDs and QDashs also potentially enables a single growth process (without transferring to MBE for QD growths) to enhance the throughput and extend the emission wavelengths to C and L bands. GaSb-based SWIR lasers on Si have also been developing rapidly. Defect-insensitive device designs such as ICLs have demonstrated promising efficiency and service lifetime, which could potentially be transferred to SiGeSn SWIR laser structures to address the lattice mismatch challenges. For Group IV lasers, recent SiGeSn/GeSn heterojunction laser diodes have already demonstrated lower threshold current densities than early homojunction III–V lasers up to 140 K, indicating sufficient directness in bandgap. The remaining challenge of carrier confinement can potentially be addressed by the lattice-matched SRO QWs discussed earlier, enabling room-temperature and higher temperature operation. In terms of band-engineered Ge, we envision that nanoscale local stressors and/or "strain dopants" will be much more effective than straining the entire device structure, potentially leading to "strain-induced QDs" as efficient gain media on Si. Another emerging technology is leveraging direct gap hexagonal SiGe, which could potentially be scaled up by deliberately engineering stacking faults (local hexagonal structured regimes) in (Si)Ge heteroepitaxy via nanoscale selective area growth or ART growth.

For photonic modulators on Si PICs, we envision that strained Si, as already has been widely used in CMOS transistors, could also potentially boost the energy efficiency and bandwidth by ~2× compared to current Si FCPD modulators, thereby continue dominating Si PICs in the near future due to its maturity and facile fabrication process. For ultralow power and ultrahigh bandwidth intensity modulation in data communications, GeSi EAMs, especially those synergistically utilizing both Δn and Δk, are the most promising candidates for the next generation. They have also entered the PDK of some Si PIC foundries such as IMEC. Shifting from Si FCPD to high-performance LEO platforms, such as TFLN and BTO, is necessary for microwave Si PICs due to the requirement of high linearity and low loss. For LiDAR applications, we envision that GeSi EAMs and ferroelectric oxide modulators could, respectively, boost the performance of optical switches in FPSA and phase shifters in OPA systems by orders of magnitude in terms of speed and energy efficiency.

For photodetectors and image sensors, we believe that the existing waveguide-integrated Ge/Si photodetector platform already addresses most of the needs of Si PICs. Remaining challenges in high-power, high-speed TWPDs or UTCs for microwave photonics applications can potentially be addressed by splitting the input power into a dense array of Ge/Si photodetectors, utilizing their advantages in large-scale integration. Techniques such as lock-in pixels can be utilized in ToF LiDAR camera applications to greatly alleviate the dark current challenge of Ge/Si compared to InGaAs photodetectors. We envision that Ge/Si photodetectors for 2D or 3D imaging could become a promising area of growth in the near future. On the other hand, realistic applications of Ge/Si photodetectors in photon counting could still be challenging, which might be better implemented using grafted III–V/Si APDs instead, as discussed earlier. For GeSn SWIR and MWIR detectors, materials quality due to lattice mismatch and thermal stability is the biggest hurdle. In the SWIR regime, this can be addressed by waveguide integration for PICs or photon management for image sensors using existing SiGeSn growth methods. In the MWIR regime, SRO engineering will help us to address this issue through maximal spectral extension with the minimal amount of Sn alloying and, therefore, the minimal lattice mismatch. We also show promising progress in integrating x-ray photon energy attenuation layers and GeSn IR absorbers on standard Si CIS using BEOL processing, opening a path toward wide spectral extension based on "CMOS +X" image sensors by riding on the wings of Si CIS as the highest volume commercial photonics product based on Si so far.

Last but not least, we present a brief outlook on the future synergy between Si PICs and Si CIS toward ultrahigh capacity optical I/O, ultrafast imaging systems, and on-chip molecular sensing applications. We envision that exchanges between these two Si photonics communities will potentially lead to new groundbreaking ideas and applications in the future. We also provide a roadmap for future development of major active photonic devices based on the trend of development over the past two decades, highlighting the projected progress of emerging technologies.

ACKNOWLEDGMENTS

Early theoretical and EXAFS studies of SRO in GeSn alloys, as well as fundamentals of GeSn crystallization process, have been supported by the Air Force Office of Scientific Research under Award No. FA9550-19-1-0341 managed by Dr. Gernot Pomrenke and Dr. Wooddy Miller. GeSn/Si CMOS image sensor device modeling has been supported by Air Force Research Laboratory Small Business Technology Transfer Program under Award No. FA8650-18-C-1638 managed by Dr. Bruce Claflin. In-depth studies on the atomic ordering in SiGeSn alloys as well as GeSn digital alloys have been supported as part of μ-ATOMS, an Energy Frontier Research Center funded by the U.S. Department of Energy (DOE), Office of Science, Basic Energy Sciences (BES), under Award No. DE-SC0023412. Research on the SuMMIT BEOL integration scheme has been supported by the National Science Foundation's (NSF) Future of Semiconductors (FuSe) program under Award Nos. 2328839 and 2328841. The concept of computing-clusters accelerated by photonics (CAP) has been partially supported by NSF FuSe Award No. 2235414. Wang and Liu would also like to thank Professor Eric Fossum for his collaborations on spectrally extended CMOS image sensors, as well as Dr. Wenhui Hu and Dr. Xiaoyi Zhang at Argonne National Laboratory for their support with EXAFS analyses.

AUTHOR DECLARATIONS

Conflict of Interest

The authors have no conflicts to disclose.

Author Contributions

Xiaoxin Wang: Conceptualization (equal); Data curation (equal); Investigation (equal); Writing – original draft (equal). **Tianshu Li:** Conceptualization (equal); Funding acquisition (equal); Investigation (equal); Software (equal); Writing – review & editing (equal). **Juejun Hu:** Conceptualization (equal); Funding acquisition (equal); Investigation (equal); Writing – review & editing (equal). **Jifeng Liu:** Conceptualization (equal); Data curation (equal); Writing – original draft (equal); Writing – review & editing (equal).

DATA AVAILABILITY

The data that support the findings of this study are available from the corresponding authors upon reasonable request.

REFERENCES

[1]N. Margalit, C. Xiang, S. M. Bowers, A. Bjorlin, R. Blum, and J. E. Bowers, "Perspective on the future of silicon photonics and electronics," Appl. Phys. Lett. **118**, 220501 (2021).
[2]R. A. Soref and J. P. Larenzo, "All-silicon active and passive guided-wave components for λ = 1.3 and 1.6 μm," IEEE J. Quantum Electron. **22**, 873–879 (1986).
[3]J. Liu, J. Michel, W. Giziewicz, D. Pan, K. Wada, D. D. Cannon, S. Jongthammanurak, D. T. Danielson, L. C. Kimerling, J. Chen, F. Ömer Ilday, F. X. Kärtner, and J. Yasaitis, "High-performance, tensile-strained Ge p-i-n photodetectors on a Si platform," Appl. Phys. Lett. **87**, 103501 (2005).
[4]D. Ahn, C.-y. Hong, J. Liu, W. Giziewicz, M. Beals, L. C. Kimerling, J. Michel, J. Chen, and F. X. Kärtner, "High performance, waveguide integrated Ge photodetectors," Opt. Express **15**, 3916–3921 (2007).
[5]Y. Kang, H.-D. Liu, M. Morse, M. J. Paniccia, M. Zadka, S. Litski, G. Sarid, A. Pauchard, Y.-H. Kuo, H.-W. Chen, and W. S. Zaoui, "Monolithic germanium/silicon avalanche photodiodes with 340 GHz gain-bandwidth product," Nat. Photonics **3**, 59–63 (2009).
[6]A. Liu, R. Jones, L. Liao, D. samara-Rubio, D. Rubin, O. Cohen, R. Nicolaescu, and M. Paniccia, "A high-speed silicon optical modulator based on a metal–oxide–semiconductor capacitor," Nature **427**, 615–618 (2004).
[7]J. Liu, M. Beals, A. Pomerene, S. Bernardis, R. Sun, J. Cheng, L. C. Kimerling, and J. Michel, "Waveguide-integrated, ultralow-energy GeSi electro-absorption modulators," Nat. Photonics **2**, 433–437 (2008).
[8]A. W. Fang, H. Park, O. Cohen, R. Jones, M. J. Paniccia, and J. E. Bowers, "Electrically pumped hybrid AlGaInAs-silicon evanescent laser," Opt. Express **14**, 9203–9210 (2006).
[9]T. Wang, H. Liu, A. Lee, F. Pozzi, and A. Seeds, "1.3-μm InAs/GaAs quantum-dot lasers monolithically grown on Si substrates," Opt. Express **19**, 11381–11386 (2011).
[10]J. Liu, X. Sun, R. Camacho-Aguilera, L. C. Kimerling, and J. Michel, "Ge-on-Si laser operating at room temperature," Opt. Lett. **35**, 679–681 (2010).
[11]R. E. Camacho-Aguilera, Y. Cai, N. Patel, J. T. Bessette, M. Romagnoli, L. C. Kimerling, and J. Michel, "An electrically pumped germanium laser," Opt. Express **20**, 11316–11320 (2012).
[12]R. Koerner, M. Oehme, M. Gollhofer, M. Schmid, K. Kostecki, S. Bechler, D. Widmann, E. Kasper, and J. Schulze, "Electrically pumped lasing from Ge Fabry-Pérot resonators on Si," Opt. Express **23**, 14815–14822 (2015).
[13]S. Wirths, R. Geiger, N. von den Driesch, G. Mussler, T. Stoica, S. Mantl, Z. Ikonic, M. Luysberg, S. Chiussi, J. M. Hartmann, H. Sigg, J. Faist, D. Buca, and D. Grützmacher, "Lasing in direct-bandgap GeSn alloy grown on Si," Nat. Photonics **9**, 88–92 (2015).
[14]Y. Zhou, Y. Miao, S. Ojo, H. Tran, G. Abernathy, J. M. Grant, S. Amoah, G. Salamo, W. Du, J. Liu, J. Margetis, J. Tolle, Y.-h. Zhang, G. Sun, R. A. Soref, B. Li, and S.-Q. Yu, "Electrically injected GeSn lasers on Si operating up to 100 K," Optica **7**, 924–928 (2020).
[15]*Integrated Photonics for Data Communication Applications*, Series: Integrated Photonics Apps Specific Design & Manufacturing, edited by M. Glick, L. Liao, and K. Schmidtke (Elsevier, 2023), pp. 123–157, ISBN: 9780323912242.
[16]N. M. Fahrenkopf, C. McDonough, G. L. Leake, Z. Su, E. Timurdogan, and D. D. Coolbaugh, "The AIM photonics MPW: A highly accessible cutting edge technology for rapid prototyping of photonic integrated circuits," IEEE J. Sel. Top. Quantum Electron. **25**(5), 1–6 (2019).
[17]See https://www.imec-int.com/en/what-we-offer/development/photonics for the available silicon photonics foundry services.
[18]S. Y. Siew, B. Li, F. Gao, H. Y. Zheng, W. Zhang, P. Guo, S. W. Xie, A. Song, B. Dong, L. W. Luo, C. Li, X. Luo, and G.-Q. Lo, "Review of silicon photonics technology and platform development," J. Lightwave Technol. **39**, 4374–4389 (2021).
[19]C. Doerr, L. Chen, D. Vermeulen, T. Nielsen, S. Azemati, S. Stulz, G. McBrien, X.-M. Xu, B. Mikkelsen, M. Givehchi, C. Rasmussen, and S.-Y. Park, "Single-chip silicon photonics 100-Gb/s coherent transceiver," in *Optical Fiber*

Communication Conference: Postdeadline Papers (Optica Publishing Group, 2014), p. Th5C.1.
[20]See https://www.intel.com/content/www/us/en/architecture-and-technology/silicon-photonics/400g-dr4-qsfp-dd-optical-transceiver.html for information about "Intel® Silicon Photonics 400G DR4+ QSFP-DD Optical Transceiver."
[21]Y. Wang, K. Al-hemyari, O. I. Dosunmu, S. Fathololoumi, P. Doussiere, K. Nguyen, S. Burmeister, D. Patel, A. Liu, P. Wen, C. Wang, S. Priyadarshi, and J. Zhou, "A 224 Gb/s per channel PAM4 DR4-Tx optical sub-system based on Si micro-ring modulator with hybrid integrated laser and SOA," in *2023 IEEE Silicon Photonics Conference (SiPhotonics)*, Washington, DC, USA (IEEE, 2023), pp. 1–2.
[22]See https://community.intel.com/t5/Blogs/Tech-Innovation/Artificial-Intelligence-AI/Intel-Shows-OCI-Optical-I-O-Chiplet-Co-packaged-with-CPU-at/post/1582541 for information about Intel's Optical Compute Interface (OCI).
[23]J. Sun, E. Timurdogan, A. Yaacobi, E. S. Hosseini, and M. R. Watts, "Large-scale nanophotonic phased array," Nature **493**, 195–199 (2013).
[24]See https://www.analogphotonics.com/technology/ for information about LiDAR technologies being developed at Analog Photonics, Inc.
[25]A. Rizzo, A. Novick, V. Gopal, B. Y. Kim, X. Ji, S. Daudlin, Y. Okawachi, Q. Cheng, M. Lipson, A. L. Gaeta, and K. Bergman, "Massively scalable Kerr comb-driven silicon photonic link," Nat. Photonics **17**, 781–790 (2023).
[26]T. Sharma, J. Wang, B. K. Kaushik, Z. Cheng, R. Kumar, Z. Wei, and X. Li, "Review of recent progress on silicon nitride-based photonic integrated circuits," IEEE Access **8**, 195436–195446 (2020).
[27]X. Wang, A. Cuervo Covian, L. Je, S. Fu, H. Li, J. Piao, and J. Liu, "GeSn on insulators (GeSnOI) toward mid-infrared integrated photonics," Front. Phys. **7**, 134 (2019).
[28]M. E. Kurdi, A. Bjelajac, M. Gromovyi, E. Sakat, Z. Ikonic, V. Reboud, A. Chelnokov, N. Pauc, V. Calvo, J.-M. Hartmann, and D. Buca, "GeSnOI technology enabling room temperature lasing with GeSn alloys," Proc. SPIE **PC12426**, PC1242606 (2023).
[29]G. Poberaj, H. Hu, W. Sohler, and P. Günter, "Lithium niobate on insulator (LNOI) for micro-photonic devices," Laser Photonics Rev. **6**, 488–503 (2012).
[30]W. Bogaerts, D. Pérez, J. Capmany, D. A. B. Miller, J. Poon, D. Englund, F. Morichetti, and A. Melloni, "Programmable photonic circuits," Nature **586**, 207–216 (2020).
[31]M. Dong, G. Clark, A. J. Leenheer, M. Zimmermann, D. Dominguez, A. J. Menssen, D. Heim, G. Gilbert, D. Englund, and M. Eichenfield, "High-speed programmable photonic circuits in a cryogenically compatible, visible–near-infrared 200 mm CMOS architecture," Nat. Photonics **16**, 59–65 (2022).
[32]D. M. Kita, B. Miranda, D. Favela, D. Bono, J. Michon, H. Lin, T. Gu, and J. Hu, "High-performance and scalable on-chip digital Fourier transform spectroscopy," Nat. Commun. **9**, 4405 (2018).
[33]D. Marpaung, J. Yao, and J. Capmany, "Integrated microwave photonics," Nat. Photonics **13**, 80–90 (2019).
[34]B. Marzban, L. Seidel, T. Liu, K. Wu, V. Kiyek, M. H. Zoellner, Z. Ikonic, J. Schulze, D. Grützmacher, G. Capellini, M. Oehme, J. Witzens, and D. Buca, "Strain engineered electrically pumped SiGeSn microring lasers on Si," ACS Photonics **10**(1), 217–224 (2023).
[35]Y. Zhou, S. Ojo, C.-W. Wu, Y. Miao, H. Tran, J. M. Grant, G. Abernathy, S. Amoah, J. Bass, G. Salamo, W. Du, G.-E. Chang, J. Liu, J. Margetis, J. Tolle, Y.-H. Zhang, G. Sun, R. A. Soref, B. Li, and S.-Q. Yu, "Electrically injected GeSn lasers with peak wavelength up to 2.7 μm," Photonics Res. **10**, 222–229 (2022).
[36]S. Acharya, H. Stanchu, R. Kumar, S. Ojo, M. Alher, M. Benamara, G.-E. Chang, B. Li, W. Du, and S.-Q. Yu, "Electrically injected Mid-infrared GeSn laser on Si operating at 140 K," IEEE J. Sel. Top. Quantum Electron. **31**(1), 1–7 (2025).
[37]Y.-D. Hsieh, J.-H. Lin, R. Soref, G. Sun, H.-H. Cheng, and G.-E. Chang, "Electro-absorption modulation in GeSn alloys for wide-spectrum mid-infrared applications," Commun. Mater. **2**, 40 (2021).
[38]B. Cao, S. Chen, X. Jin, J. Liu, and T. Li, "Short-range order in GeSn alloy," ACS Appl. Mater. Interfaces **12**, 57245–57253 (2020).
[39]M. A. Mircovich, C. Xu, D. A. Ringwala, C. D. Poweleit, J. Menéndez, and J. Kouvetakis, "Extended compositional range for the synthesis of SWIR and LWIR Ge1-ySny alloys and device structures via CVD of SnH4 and Ge3H8," ACS Appl. Electron. Mater. **3**(365), 3451–3460 (2021).
[40]X. Jin, S. Chen, and T. Li, "Coexistence of two types of short-range order in Si–Ge–Sn medium-entropy alloys," Commun. Mater. **3**, 66 (2022).
[41]X. Jin, S. Chen, and T. Li, "Enabling type I lattice-matched heterostructures in SiGeSn alloys through engineering composition and short-range order: A first-principles perspective," IEEE J. Sel. Top. Quantum Electron. **31**(1), 1–10 (2025).
[42]J. Zach Lentz, J. C. Woicik, M. Bergschneider, R. Davis, A. Mehta, K. Cho, and P. C. McIntyre, " Local ordering in Ge/Ge–Sn semiconductor alloy core/shell nanowires revealed by extended x-ray absorption fine structure (EXAFS)," Appl. Phys. Lett. **122**(6), 062103 (2023).
[43]W. Dou, M. Benamara, A. Mosleh, J. Margetis, P. Grant, Y. Zhou, S. Al-Kabi, W. Du, J. Tolle, B. Li, M. Mortazavi, and S.-Q. Yu, Sci. Rep. **8**, 5640 (2018).
[44]S. Liu, A. C. Covian, X. Wang, C. T. Cline, A. Akey, W. Dong, S.-Q. Yu, and J. Liu, "3D nanoscale mapping of short-range order in GeSn alloys," Small Methods **6**(5), 2200029 (2022).
[45]S. Liu, S. Chen, X. Jin, J.-H. Bae, I. Bikmukhametov, D. Jaeger, O. Concepcion, A. C. Covian, X. Wang, C. T. Cline, A. Akey, L. M. Vogl, H. Zhao, Y. Zeng, A. M. Minor, S.-Q. Yu, D. Buca, T. Li, and J. Liu, "Atomic short-range order in SiGeSn alloys," preprint available at Research Square (unpublished), available at https://doi.org/10.21203/rs.3.rs-4909892/v1.
[46]L. M. Vogl, P. Schweizer, S. Chen, X. Jin, S.-Q. Yu, D. O. Byrne, F. I. Allen, J. Liu, T. Li, and A. M. Minor, "Exploring short-range ordering in semiconducting materials," Microsc. Microanal. **30**(Suppl 1), 1137–1138 (2024).
[47]L. M. Vogl, S. Chen, P. Schweizer, X. Jin, S.-Q. Yu, J. Liu, T. Li, and A. M. Minor, "Identification of short-range order motifs in semiconductors" Science (in press) (2025).
[48]S. Liu, Y. Liang, H. Zhao, N. M. Eldose, J.-H. Bae, O. Concepcion, X. Jin, S. Chen, I. Bikmukhametov, A. Akey, C. T. Cline, A. C. Covian, X. Wang, T. Li, Y. Zeng, D. Buca, S.-Q. Yu, G. J. Salamo, S. Zhang, and J. Liu, "Comparison of short-range order in GeSn grown by molecular beam epitaxy and chemical vapor deposition."
[49]A. A. Corley-Wiciak, O. Concepción, M. H. Zoellner, G. Sfruncia, F. Bärwolf, G. Nicotra, D. Grützmacher, D. Buca, G. Capellini, and D. Spirito, "Polarization-resolved Raman spectroscopy reveals the atomic local ordering in silicon germanium tin epitaxial alloys," Phys. Rev. Mater. **8**, 104601 (2024).
[50]E. Rudkevich, F. Liu, D. E. Savage, T. F. Kuech, L. McCaughan, and M. G. Lagally, "Hydrogen induced Si surface segregation on Ge-covered Si (001)," Phys. Rev. Lett. **81**, 3467 (1998).
[51]Y. Liang, D. West, S. Chen, J. Liu, T. Li, and S. Zhang, "Semiconductor-compatible topological digital alloys," Mater. Today **86**, 115–125 (2025).
[52]D. Z.-Y. Ting, A. Soibel, L. Höglund, J. Nguyen, C. J. Hill, A. Khoshakhlagh, and S. D. Gunapala, "Type-II superlattice infrared detectors," in *Semiconductors and Semimetals*, edited by S. D. Gunapala, D. R. Rhiger, and C. Jagadish (Elsevier, 2011), Chap. 1, Vol. 84, pp. 1–57.
[53]S. J. Maddox, S. D. March, and S. R. Bank, "Broadly tunable AlInAsSb digital alloys grown on GaSb," Cryst. Growth Des. **16**(7), 3582–3586 (2016).
[54]H. Li, X. Wang, and J. Liu, "Highly effective strain-induced band-engineering of (111) oriented, direct-gap GeSn crystallized on amorphous SiO_2 layers," Appl. Phys. Lett. **108**, 102101 (2016).
[55]W. Wegscheider, K. Eberl, U. Menczigar, and G. Abstreiter, "Single-crystal Sn/Ge superlattices on Ge substrates: Growth and structural properties," Appl. Phys. Lett. **57**, 875–877 (1990).
[56]G. Roelkens, J. Zhang, L. Bogaert, M. Billet, D. Wang, B. Pan, C. J. Kruckel, E. Soltanian, D. Maes, T. Vanackere, T. Vandekerckhove, S. Cuyvers, J. De Witte, I. L. Lufungula, X. Guo, H. Li, S. Qin, G. Muliuk, S. Uvin, B. Haq, C. Op de Beeck, J. Goyvaerts, G. Lepage, P. Verheyen, J. Van Campenhout, G. Morthier, B. Kuyken, D. Van Thourhout, and R. Baets, "Micro-transfer printing for

heterogeneous Si photonic integrated circuits," IEEE J. Sel. Top. Quantum Electron. **29**(3), 1–14 (2023).
[57]D. Liu, S. J. Cho, J.-H. Seo, K. Kim, M. Kim, J. Shi, X. Yin, W. Choi, C. Zhang, J. Kim, M. A. Baboli, J. Park, J. Bong, I.-K. Lee, J. Gong, S. Mikael, J. H. Ryu, P. K. Mohseni, X. Li, S. Gong, X. Wang, and Z. Ma, "Lattice-mismatched semiconductor heterostructures," arXiv:1812.10225 (2018).
[58]H. N. Abbasi, S. Lee, H. Jung, N. Gajowski, Y. Lu, L. Wang, D. Kim, J. Zhou, J. Gong, C. Chae, J. Hwang, M. Muduli, S. Nookala, Z. Ma, and S. Krishna, "Structural and electrical properties of grafted Si/GaAsSb heterojunction," Appl. Phys. Lett. **125**, 101107 (2024).
[59]J. Zhou, J. Gong, S. Lal, J. Kim, W. Lin, C. Chen, C. Li, Y. Lu, S. Qiu, Y. Dong, L. German, X. Wang, F. Xia, and Z. Ma, "Characteristics of native oxides-interfaced GaAs/Ge np diodes," IEEE Electron Device Lett. **45**(9), 1669–1672 (2024).
[60]J. Liang, L. Chai, S. Nishida, M. Morimoto, and N. Shigekawa, "Investigation on the interface resistance of Si/GaAs heterojunctions fabricated by surface-activated bonding," Jpn. J. Appl. Phys. **54**, 030211 (2015).
[61]C. Renard, T. Molière, N. Cherkashin, J. Alvarez, L. Vincent, A. Jaffré, G. Hallais, J. P. Connolly, D. Mencaraglia, and D. Bouchier, "High current density GaAs/Si rectifying heterojunction by defect free epitaxial lateral overgrowth on tunnel oxide from nano-seed," Sci. Rep. **6**, 25328 (2016).
[62]L. Ranno, J. X. B. Sia, K. P. Dao, and J. Hu, "Multi-material heterogeneous integration on a 3-D photonic-CMOS platform," Opt. Mater. Express **13**, 2711–2725 (2023).
[63]K. Hayashi, K. P. Dao, M. J. Gross, L. Ranno, J. X. B. Sia, T. Fakhrul, Q. Du, N. Chatterjee, J. Hu, and C. A. Ross, "Magneto-optical Bi-substituted yttrium and terbium iron garnets for on-chip crystallization via microheaters," Adv. Opt. Mater. **12**, 2400708 (2024).
[64]S. E. Marzen, E. Postelnicu, J. Michel, K. Wada, and L. C. Kimerling, "High performance germanium on silicon photodiodes for back-end-of-line photonic integration," Appl. Phys. Lett. **123**, 111105 (2023).
[65]J. Michel, J. Liu, and L. C. Kimerling, "High-performance Ge-on-Si photodetectors," Nat. Photonics **4**(8), 527–534 (2010).
[66]T. A. Langdo, C. W. Leitz, M. T. Currie, E. A. Fitzgerald, A. Lochtefeld, and D. A. Antoniadis, "High quality Ge on Si by epitaxial necking," Appl. Phys. Lett. **76**(25), 3700–3702 (2000).
[67]J. G. Fiorenza, J.-S. Park, J. Hydrick, J. Li, J. Li, M. Curtin, M. Carroll, and A. Lochtefeld, "Aspect ratio trapping: A unique technology for integrating Ge and III–Vs with silicon CMOS," ECS Trans. **33**, 963 (2010).
[68]H. Stanchu, G. Abernathy, J. Grant, F. M. de Oliveira, Y. I. Mazur, J. Liu, W. Du, B. Li, G. J. Salamo, and S.-Q. Yu, "Development of aspect ratio trapping growth of GeSn on Si for midwave infrared applications," J. Vac. Sci. Technol. B **42**(4), 042802 (2024).
[69]S. Q. Lim, L. Q. Huston, L. A. Smillie, G. J. Grzybowski, X. Huang, J. S. Williams, and B. B. Claflin, " Remote plasma-enhanced chemical vapor deposition of GeSn on Si: Material and defect characterization," J. Appl. Phys. **133**(23), 235302 (2023).
[70]K. McComber, X. Duan, J. Liu, L. C. Kimerling, and J. Michel, "Single-crystal germanium growth on amorphous silicon," Adv. Funct. Mater. **22**(5), 1049–1057 (2012).
[71]B. S. Pearson, L. C. Kimerling, and J. Michel, "Germanium photodetectors on amorphous substrates for electronic-photonic integration," in *2016 IEEE 13th International Conference on Group IV Photonics (GFP)* (IEEE, 2016), pp. 20–21.
[72]M. Klingenstein, J. Kuhl, J. Rosenzweig, C. Moglestue, A. Hülsmann, J. Schneider, and K. Köhler, "Photocurrent gain mechanisms in metal-semiconductor-metal photodetectors," Solid-State Electron. **37**(2), 333–340 (1994).
[73]H. Li, J. Brouillet, A. Salas, X. Wang, and J. Liu, "Low temperature growth of high crystallinity GeSn on amorphous layers for advanced optoelectronics," Opt. Mater. Express **3**, 1385–1396 (2013).
[74]S. Li, S. Liu, H. Stanchu, G. Abernathy, B. Li, S.-Q. Yu, X. Wang, J. Liu, and J. Liu, "Ion implantation damage recovery in GeSn thin films," IEEE J. Sel. Top. Quantum Electron. **31**(1), 8100208 (2025).
[75]J. Liu, D. D. Cannon, K. Wada, Y. Ishikawa, S. Jongthammanurak, D. T. Danielson, J. Michel, and L. C. Kimerling, "Tensile strained Ge p-i-n photodetectors on Si platform for C and L band telecommunications," Appl. Phys. Lett. **87**(1), 011110 (2005).
[76]H. Tran, T. Pham, W. Du, Y. Zhang, P. C. Grant, J. M. Grant, G. Sun, R. A. Soref, J. Margetis, J. Tolle, B. Li, M. Mortazavi, and S.-Q. Yu, "High performance Ge0.89Sn0.11 photodiodes for low-cost shortwave infrared imaging," J. Appl. Phys. **124**(1), 013101 (2018).
[77]K. Muth, "Co-packaged and linear optics for AI networks" *Integrated Photonics System Roadmap (IPSR)-International 2024 Spring Meeting*, Cambridge, MA (Microphotonics Center, Massachusetts Institute of Technology, 2024).
[78]See https://opticalconnectionsnews.com/2024/03/ofc-2024-new-51-2t-cpo-switch-delivers-70-power-reduction/ for information about Broadcom's co-packaged optics (CPO) Ethernet switch.
[79]B. Stern, X. Ji, Y. Okawachi, A. L. Gaeta, and M. Lipson, "Battery-operated integrated frequency comb generator," Nature **562**, 401–405 (2018).
[80]P. Marin-Palomo, J. N. Kemal, T. J. Kippenberg, W. Freude, S. Randel, and C. Koos, "Performance of chip-scale optical frequency comb generators in coherent WDM communications," Opt. Express **28**, 12897–12910 (2020).
[81]Z. Sun, Y. Li, B. Bai, Z. Zhu, and H.-B. Sun, "Silicon nitride-based Kerr frequency combs and applications in metrology," Adv. Photonics **4**(6), 064001 (2022).
[82]J. M. C. Boggio, D. Bodenmüller, S. Ahmed, S. Wabnitz, D. Modotto, and T. Hansson, "Efficient Kerr soliton comb generation in micro-resonator with interferometric back-coupling," Nat. Commun. **13**, 1292 (2022).
[83]See https://picmagazine.net/article/116262/Vector_Photonics_to_commercialise_an_uncooled_1_Watt_1310nm_CW_PCSEL for information about high power single-mode photonic crystal surface emitting lasers (PCSELs).
[84]S. Yu, H. Zuo, X. Sun, J. Liu, T. Gu, and J. Hu, "Optical free-form couplers for high-density integrated photonics (OFFCHIP): A universal optical interface," J. Lightwave Technol. **38**, 3358–3365 (2020).
[85]ÓB Helgason, M. Girardi, Z. Ye, F. Lei, J. Schröder, and V. Torres-Company, "Surpassing the nonlinear conversion efficiency of soliton microcombs," Nat. Photonics **17**, 992–999 (2023).
[86]Y. Nakatsu, Y. Nagao, T. Hirao, K. Kozuru, T. Kanazawa, S. Masui, E. Okahisa, T. Yanamoto, and S.-i. Nagahama, "Edge-emitting blue laser diode with high CW wall-plug efficiency of 50%," Proc. SPIE **12001**, 1200109 (2022).
[87]See https://www.ushio.com/product/638nm-multi-mode-high-power-long-life-red-laser-diode/ for information about wall plug efficiency of commercial red laser diodes.
[88]P. Crump, J. Wang, T. Crum, S. Das, M. DeVito, W. Dong, J. Farmer, Y. Feng, M. Grimshaw, D. Wise, and S. Zhang, ">360 W and >70% efficient GaAs-based diode lasers," Proc. SPIE **5711**, 21 (2005).
[89]L. Wang, H. Qu, A. Qi, X. Zhou, and W. Zheng, "High-power laser diode at 9xx nm with 81.10% efficiency," Opt. Lett. **47**, 3231–3234 (2022).
[90]C. M. Schultz, P. Crump, H. Wenzel, O. Brox, A. Maaßdorf, G. Erbert, and G. Tränkle, "11 W broad area 976 nm DFB lasers with 58% power conversion efficiency," Electron. Lett. **46**, 580 (2010).
[91]H. Fujita, K. Ueno, O. Morohara, E. Camargo, H. Geka, Y. Shibata, and N. Kuze, "AlInSb mid-infrared LEDs of high luminous efficiency for gas sensors," Phys. Status Solidi A **215**, 1700449 (2018).
[92]T. H. Gfroerer, L. P. Priestley, M. F. Fairley, and M. W. Wanlass, "Temperature dependence of nonradiative recombination in low-band gap $In_xGa_{1-x}As/InAs_yP_{1-y}$ double heterostructures grown on InP substrates," J. Appl. Phys. **94**(3), 1738–1743 (2003).
[93]B. Wang, L. Zhou, S. Tan, W. Liu, G. Deng, and J. Wang, "71% wall-plug efficiency from 780 nm-emitting laser diode with GaAsP quantum well," Opt. Laser Technol. **168**, 109867 (2024).
[94]S. S. Mikhrin, A. R. Kovsh, I. L. Krestnikov, A. V. Kozhukhov, D. A. Livshits, N. N. Ledentsov, Y. M. Shernyakov, I. I. Novikov, M. V. Maximov, V. M. Ustinov, and Z. I. Alferov, "High power temperature-insensitive 1.3 μm InAs/InGaAs/GaAs quantum dot lasers," Semicond. Sci. Technol. **20**, 340 (2005).

[95]J. Bowers, A. Gossard, S. Liu, J. Norman, Y. Wan, C. Zhang, R. Zheng, B. Herrick, W. Chao, and F. Grillot, "Reflection insensitive quantum dot lasers grown on silicon substrates," in *2019 Enlightened Annual Meeting* (Advanced Research Projects Agency-Energy, 2019), see https://arpa-e.energy.gov/sites/default/files/UCSB_Bowers_ENLITENED_Annual_Meeting.pdf.
[96]D. Jung, J. Norman, M. J. Kennedy, C. Shang, B. Shin, Y. Wan, A. C. Gossard, and J. E. Bowers, "High efficiency low threshold current 1.3 μm InAs quantum dot lasers on on-axis (001) GaP/Si," Appl. Phys. Lett. **111**(12), 122107 (2017).
[97]T. Garrod, D. Olson, M. Klaus, C. Zenner, C. Galstad, L. Mawst, and D. Botez, "50% continuous-wave wallplug efficiency from 1.53 μm-emitting broad-area diode lasers," Appl. Phys. Lett. **105**(7), 071101 (2014).
[98]W. Zhou, Y. Zhu, J. Wang, M. Moewe, R. Zhu, W. Zhao, V. Rossin, H. Liu, J. Wang, T. Zhu, P. Yalamanchili, T. Pham, R. Chen, V. Zeng, and J. Stewart, "High power CW laser for Co-packaged optics," in *Conference on Lasers and Electro-Optics, Technical Digest Series* (Optica Publishing Group, 2022), p. SS2D.3.
[99]See https://www.semiconductor-today.com/news_items/2023/mar/alfalume-060323.shtml for information about wall plug efficiency of single-mode 1310 nm laser diodes.
[100]J. R. Vaskasi, N. Singh, J. Van Kerrebrouck, J. Bauwelinck, G. Roelkens, and G. Morthier, "High wall-plug efficiency and narrow linewidth III-V-on-silicon C-band DFB laser diodes," Opt. Express **30**, 27983–27992 (2022).
[101]S. Yu, H. Zuo, X. Wang, X. Sun, J. Liu, J. Hu, and T. Gu, "Seamless Hybrid-integrated Interconnect NEtwork (SHINE)," in *Optical Fiber Communication Conference (OFC) 2019, OSA Technical Digest* (Optica Publishing Group, 2019), p. M4D.5.
[102]S. Matsuo, "Heterogeneously integrated III–V photonic devices on Si," in *Semiconductors and Semimetals*, edited by S. Lourdudoss, J. E. Bowers, and C. Jagadish (Elsevier, 2019), Chap. 2, Vol. 101, pp. 43–89.
[103]A. Dhakal, P. C. Wuytens, F. Peyskens, K. Jans, N. L. Thomas, and R. Baets, "Nanophotonic waveguide enhanced Raman spectroscopy of biological submonolayers," ACS Photonics **3**(11), 2141–2149 (2016).
[104]J. Ma, S. Chan, and E. R. Fossum, "Review of quanta image sensors for ultralow-light imaging," IEEE Trans. Electron Devices **69**(6), 2824–2839 (2022).
[105]M. Mahmud-Ul-Hasan, P. Neutens, R. Vos, L. Lagae, and P. Van Dorpe, "Suppression of bulk fluorescence noise by combining waveguide-based near-field excitation and collection," ACS Photonics **4**(3), 495–500 (2017).
[106]A. Malik, C. Xiang, L. Chang, W. Jin, J. Guo, M. Tran, and J. Bowers, "Low noise, tunable silicon photonic lasers," Appl. Phys. Rev. **8**, 031306 (2021).
[107]See https://legacy.www.sbir.gov/node/1932887 for information about application of 1550 nm lasers in LiDAR systems.
[108]V. Sivaprakasam, D. Lin, M. K. Yetzbacher, H. E. Gemar, J. M. Portier, and A. T. Watnik, "Multi-spectral SWIR lidar for imaging and spectral discrimination through partial obscurations," Opt. Express **31**, 5443–5457 (2023).
[109]K. M. Judd, M. P. Thornton, and A. A. Richards, "Automotive sensing: Assessing the impact of fog on LWIR, MWIR, SWIR, visible, and lidar performance," Proc. SPIE **11002**, 110021F (2019).
[110]C. Shang, K. Feng, E. T. Hughes, A. Clark, M. Debnath, R. Koscica, G. Leake, J. Herman, D. Harame, P. Ludewig, Y. Wan, and J. E. Bowers, "Electrically pumped quantum-dot lasers grown on 300 mm patterned Si photonic wafers," Light Sci. Appl. **11**, 299 (2022).
[111]M. Rio Calvo, L. Monge Bartolomé, M. Bahriz, G. Boissier, L. Cerutti, J.-B. Rodriguez, and E. Tournié, "Mid-infrared laser diodes epitaxially grown on on-axis (001) silicon," Optica **7**, 263 (2020).
[112]O. Moutanabbir, S. Assali, X. Gong, E. O'Reilly, C. A. Broderick, B. Marzban, J. Witzens, W. Du, S.-Q. Yu, A. Chelnokov, D. Buca, and D. Nam, "Monolithic infrared silicon photonics: The rise of (Si)GeSn semiconductors," Appl. Phys. **118**, 110502 (2021).
[113]C. Shang, Y. Wan, J. Selvidge, E. Hughes, R. Herrick, K. Mukherjee, J. Duan, F. Grillot, W. W. Chow, and J. E. Bowers, "Perspectives on advances in quantum dot lasers and integration with Si photonic integrated circuits," ACS Photonics **8**, 2555–2566 (2021).
[114]C. Hantschmann, Z. Liu, M. Tang, S. Chen, A. J. Seeds, H. Liu, I. H. White, and R. V. Penty, "Theoretical study on the effects of dislocations in monolithic III-V lasers on silicon," J. Lightwave Technol. **38**, 4801 (2020).
[115]C. Shang, E. Hughes, Y. Wan, M. Dumont, R. Koscica, J. Selvidge, R. Herrick, A. C. Gossard, K. Mukherjee, and J. E. Bowers, "High-temperature reliable quantum-dot lasers on Si with misfit and threading dislocation filters," Optica **8**, 749–754 (2021).
[116]K. H. Lee, S. Bao, B. Wang, C. Wang, S. F. Yoon, and J. Michel, "Reduction of threading dislocation density in Ge/Si using a heavily As-doped Ge seed layer," AIP Adv. **6**, 025028 (2016).
[117]J. Selvidge, J. Norman, E. T. Hughes, C. Shang, D. Jung, A. A. Taylor, M. J. Kennedy, R. Herrick, J. E. Bowers, and K. Mukherjee, "Defect filtering for thermal expansion induced dislocations in III–V lasers on silicon," Appl. Phys. Lett. **117**, 122101 (2020).
[118]D. Jung, J. Norman, Y. Wan, S. Liu, R. Herrick, J. Selvidge, K. Mukherjee, A. C. Gossard, and J. E. Bowers, "Recent advances in InAs quantum dot lasers on on-axis (001) silicon by molecular beam epitaxy," Phys. Status Solidi A **216**, 1800602 (2019).
[119]D. Liang, S. Srinivasan, A. Descos, C. Zhang, G. Kurczveil, Z. Huang, and R. Beausoleil, "High-performance quantum-dot distributed feedback laser on silicon for high-speed modulations," Optica **8**, 591–593 (2021).
[120]W.-Q. Wei, Q. Feng, J.-J. Guo, M.-C. Guo, J.-H. Wang, Z.-H. Wang, T. Wang, and J.-J. Zhang, "InAs/GaAs quantum dot narrow ridge lasers epitaxially grown on SOI substrates for silicon photonic integration," Opt. Express **28**, 26555–26563 (2020).
[121]J.-Z. Huang, W.-Q. Wei, J.-J. Chen, Z.-H. Wang, T. Wang, and J.-J. Zhang, "P-doped 1300 nm InAs/GaAs quantum dot lasers directly grown on an SOI substrate," Opt. Lett. **46**, 5525–5528 (2021).
[122]W.-Q. Wei, J.-Y. Zhang, J.-H. Wang, H. Cong, J.-J. Guo, Z.-H. Wang, H.-X. Xu, T. Wang, and J.-J. Zhang, "Phosphorus-free 1.5 μm InAs quantum-dot microdisk lasers on metamorphic InGaAs/SOI platform," Opt. Lett. **45**, 2042–2045 (2020).
[123]L. Lin, Y. Xue, W. Luo, J. Huang, and K. M. Lau, "C and L band room-temperature continuous-wave InP-based microdisk lasers grown on silicon," Opt. Lett. **46**, 2836–2839 (2021).
[124]Y. De Koninck, C. Caer, D. Yudistira, M. Baryshnikova, H. Sar, P.-Y. Hsieh, C. I. Özdemir, S. K. Patra, N. Kuznetsova, D. Colucci, A. Milenin, A. A. Yimam, G. Morthier, D. Van Thourhout, P. Verheyen, M. Pantouvaki, B. Kunert, and J. Van Campenhout, "GaAs nano-ridge laser diodes fully fabricated in a 300-mm CMOS pilot line," Nature **637**, 63–69 (2025).
[125]L. Cerutti, D. A. Díaz Thomas, J.-B. Rodriguez, M. R. Calvo, G. Patriarche, A. N. Baranov, and E. Tournié, "Quantum well interband semiconductor lasers highly tolerant to dislocations," Optica **8**, 1397–1402 (2021).
[126]B. Song, B. Shi, S. Zhu, S. Šuran Brunelli, and J. Klamkin, "Highly reliable and high speed InGaAs PIN photodetector on Si by heteroepitaxy," in *2021 Asia Communications and Photonics Conference (ACP)* (Optica Publishing Group, 2021), Paper No. W1F.2.
[127]H. Kim, S. Lee, Y.-H. Ko, J. T. Ahn, K.-J. Kim, D.-J. Kim, D.-M. Geum, and W. S. Han, "High-temperature and continuous wave-operation of all-MOCVD grown InAs/GaAs quantum dot laser diodes with highly strained layer and low temperature p-AlGaAs cladding layer," J. Alloys Compd. **983**, 173823 (2024).
[128]M. Yamaguchi, M. Tachikawa, M. Sugo, S. Kondo, and Y. Itoh, "Analysis for dislocation density reduction in selective area grown GaAs films on Si substrates," Appl. Phys. Lett. **56**(1), 27–29 (1990).
[129]H.-C. Luan, D. R. Lim, K. K. Lee, K. M. Chen, J. G. Sandland, K. Wada, and L. C. Kimerling, "High-quality Ge epilayers on Si with low threading-dislocation densities," Appl. Phys. Lett. **75**(19), 2909–2911 (1999).
[130]E. Y. Chang, G. T. Cibuzar, and K. P. Pande, "Passivation of GaAs FET's with PECVD silicon nitride films of different stress states," IEEE Trans. Electron Devices **35**(9), 1412–1418 (1988).
[131]N. A. DiLello, D. K. Johnstone, and J. L. Hoyt, "Characterization of dark current in Ge-on-Si photodiodes," J. Appl. Phys. **112**(5), 054506 (2012).

[132]Y. Okada, H. Shimomura, and M. Kawabe, "Low dislocation density GaAs on Si heteroepitaxy with atomic hydrogen irradiation for optoelectronic integration," J. Appl. Phys. **73**(11), 7376–7384 (1993).
[133]C.-W. Cheng, G. Apostolopoulos, and E. A. Fitzgerald, "The effect of interface processing on the distribution of interfacial defect states and the C-V characteristics of III–V metal-oxide-semiconductor field effect transistors," J. Appl. Phys. **109**(2), 023714 (2011).
[134]X. Wang, H. Li, R. Camacho-Aguilera, Y. Cai, L. C. Kimerling, J. Michel, and J. Liu, "Infrared absorption of n-type tensile-strained Ge-on-Si," Opt. Lett. **38**, 652–654 (2013).
[135]F. T. Armand Pilon, A. Lyasota, Y.-M. Niquet, V. Reboud, V. Calvo, N. Pauc, J. Widiez, C. Bonzon, J. M. Hartmann, A. Chelnokov, J. Faist, and H. Sigg, "Lasing in strained germanium microbridges," Nat. Commun. **10**, 2724 (2019).
[136]Y. Cai, Z. Han, X. Wang, R. E. Camacho-Aguilera, L. C. Kimerling, J. Michel, and J. Liu, "Analysis of threshold current behavior for bulk and quantum-well germanium laser structures," IEEE J. Sel. Top. Quantum Electron. **19**, 1901009 (2013).
[137]See https://www.nextnano.com/ for information about nextnano software.
[138]Y. Bai, M. T. Bulsara, and Eugene A. Fitzgerald, "Photoluminescence and secondary ion mass spectrometry investigation of unintentional doping in epitaxial germanium thin films grown on III–V compound by metal-organic chemical vapor deposition," J. Appl. Phys. **111**(1), 013502 (2012).
[139]E. M. T. Fadaly, A. Dijkstra, J. R. Suckert, D. Ziss, M. A. J. van Tilburg, C. Mao, Y. Ren, V. T. van Lange, K. Korzun, S. Kölling, M. A. Verheijen, D. Busse, C. Rödl, J. Furthmüller, F. Bechstedt, J. Stangl, J. J. Finley, S. Botti, J. E. M. Haverkort, and E. P. A. M. Bakkers, "Direct-bandgap emission from hexagonal Ge and SiGe alloys," Nature **580**, 205–209 (2020).
[140]M. A. J. van Tilburg, R. Farina, V. T. van Lange, W. H. J. Peeters, S. Meder, M. M. Jansen, M. A. Verheijen, M. Vettori, J. J. Finley, E. P. A. M. Bakkers, and J. E. M. Haverkort, "Stimulated emission from hexagonal silicon-germanium nanowires," Commun. Phys. **7**, 328 (2024).
[141]L. Seidel, T. Liu, O. Concepción, B. Marzban, V. Kiyek, D. Spirito, D. Schwarz, A. Benkhelifa, J. Schulze, Z. Ikonic, J.-M. Hartmann, A. Chelnokov, J. Witzens, G. Capellini, M. Oehme, D. Grützmacher, and D. Buca, "Continuous-wave electrically pumped multi-quantum-well laser based on group-IV semiconductors," Nat. Commun. **15**, 10502 (2024).
[142]D. Stange, S. Wirths, R. Geiger, C. Schulte-Braucks, B. Marzban, N. von den Driesch, G. Mussler, T. Zabel, T. Stoica, J.-M. Hartmann, S. Mantl, Z. Ikonic, D. Grützmacher, H. Sigg, J. Witzens, and D. Buca, "Optically pumped GeSn microdisk lasers on Si," ACS Photonics **3**, 1279–1285 (2016).
[143]J. Margetis, S. Al-Kabi, W. Du, W. Dou, Y. Zhou, T. Pham, P. Grant, S. Ghetmiri, A. Mosleh, B. Li, J. Liu, G. Sun, R. Soref, J. Tolle, M. Mortazavi, and S.-Q. Yu, "Si-based GeSn lasers with wavelength coverage of 2–3 μm and operating temperatures up to 180 K," ACS Photonics **5**, 827–833 (2018).
[144]Q. M. Thai, N. Pauc, J. Aubin, M. Bertrand, J. Chrétien, V. Delaye, A. Chelnokov, J.-M. Hartmann, V. Reboud, and V. Calvo, "GeSn heterostructure micro-disk laser operating at 230 K," Opt. Express **26**, 32500 (2018).
[145]D. Stange, N. von den Driesch, T. Zabel, F. Armand-Pilon, D. Rainko, B. Marzban, P. Zaumseil, J.-M. Hartmann, Z. Ikonic, G. Capellini, S. Mantl, H. Sigg, J. Witzens, D. Grützmacher, and D. Buca, "GeSn/SiGeSn heterostructure and multi quantum well lasers," ACS Photonics **5**, 4628–4636 (2018).
[146]J. Chrétien, N. Pauc, F. A. Pilon, M. Bertrand, Q.-M. Thai, L. Casiez, N. Bernier, H. Dansas, P. Gergaud, E. Delamadeleine, R. Khazaka, H. Sigg, J. Faist, A. Chelnokov, V. Reboud, J.-M. Hartmann, and V. Calvo, "GeSn lasers covering a wide wavelength range thanks to uniaxial tensile strain," ACS Photonics **6**, 2462–2469 (2019).
[147]Y. Zhou, W. Dou, W. Du, S. Ojo, H. Tran, S. A. Ghetmiri, J. Liu, G. Sun, R. Soref, J. Margetis, J. Tolle, B. Li, Z. Chen, M. Mortazavi, and S.-Q. Yu, "Optically pumped GeSn lasers operating at 270 K with broad waveguide structures on Si," ACS Photonics **6**, 1434–1441 (2019).
[148]A. Elbaz, D. Buca, N. von den Driesch, K. Pantzas, G. Patriarche, N. Zerounian, E. Herth, X. Checoury, S. Sauvage, I. Sagnes, A. Foti, R. Ossikovski, J.-M. Hartmann, F. Boeuf, Z. Ikonic, P. Boucaud, D. Grützmacher, and M. El Kurdi, "Ultra-low-threshold continuous-wave and pulsed lasing in tensile-strained GeSn alloys," Nat. Photonics **14**, 375–382 (2020).
[149]A. Bjelajac, M. Gromovyi, E. Sakat, B. Wang, G. Patriarche, N. Pauc, V. Valvo, P. Boucaud, F. Boeuf, A. Chelnokov, V. Reboud, M. Frauenrath, J.-M. Hartmann, and M. El Kurdi, "Up to 300 K lasing with GeSn-on-insulator microdisk resonators," Opt. Express **30**, 3954–3961 (2022).
[150]J. Chrétien, Q. M. Thai, M. Frauenrath, L. Casiez, A. Chelnokov, V. Reboud, J. M. Hartmann, M. El Kurdi, N. Pauc, and V. Calvo, "Room temperature optically pumped GeSn microdisk lasers," Appl. Phys. Lett. **120**, 051107 (2022).
[151]H. Groiss, M. Glaser, M. Schatzl, M. Brehm, D. Gerthsen, D. Roth, P. Bauer, and F. Schäffler, "Free-running Sn precipitates: An efficient phase separation mechanism for metastable $Ge_{1-x}Sn_x$ epilayers," Sci. Rep. **7**, 16114 (2017).
[152]H. Zhao, G. Lin, C. Han, R. Hickey, T. Zhama, P. Cui, T. Deroy, X. Feng, C. Ni, and Y. Zeng, "Improving the short-wave infrared response of strained GeSn/Ge multiple quantum wells by rapid thermal annealing," Vacuum **210**, 111868 (2023).
[153]G. Burns and M. I. Nathan, "P-N junction lasers," Proc. IEEE **52**(7), 770–794 (1964).
[154]J. Liu, R. Camacho-Aguilera, J. T. Bessette, X. Sun, X. Wang, Y. Cai, L. C. Kimerling, and J. Michel, "Ge-on-Si optoelectronics," Thin Solid Films **520**(8), 3354–3360 (2012).
[155]L. D. Yuan, S. S. Li, and J. W. Luo, "Direct bandgap emission from strain-doped germanium," Nat. Commun. **15**, 618 (2024).
[156]M. Shamim Reza, T. Dey, A. W. Arbogast, A. J. Muhowski, M. W. Holtz, C. A. Stephenson, S. R. Bank, D. Wasserman, and M. A. Wistey, "Growth of tin-free germanium carbon alloys using carbon tetrabromide (CBr_4)," J. Appl. Phys. **134**(18), 183103 (2023).
[157]D. Leonhardt, J. Sheng, J. G. Cederberg, M. S. Carroll, Q. Li, M. J. Romero, D. Kuciauskas, D. J. Friedman, and S. M. Han, "Removal of stacking faults in Ge grown on Si through nanoscale openings in chemical SiO_2," Thin Solid Films **519**(22), 7664–7671 (2011).
[158]A. J. Williamson, A. Franceschetti, H. Fu, L. W. Wang, and A. A. Zunger, "Indirect band gaps in quantum dots made from direct-gap bulk materials," J. Electron. Mater. **28**(5), 414–425 (1999).
[159]J.-W. Luo, A. Franceschetti, and A. Zunger, "Quantum-size-induced electronic transitions in quantum dots: Indirect band-gap GaAs," Phys. Rev. B **78**, 035306 (2008).
[160]U. Cebulla, A. Forchel, G. Tränkle, G. Griffiths, S. Subbanna, and H. Kroemer, "Direct-indirect band gap crossover in two-dimensional GaSb/AlSb-quantum-well-structures," Superlattices Microstruct. **3**(4), 429–434 (1987).
[161]S. M. Sze and K. K. Ng, *Physics of Semiconductor Devices*, 3rd ed. (John Wiley & Sons, Inc., 2007).
[162]A. A. Demkov, C. Bajaj, J. G. Ekerdt, C. J. Palmstrøm, and S. J. Ben Yoo, "Materials for emergent silicon-integrated optical computing," J. Appl. Phys. **130**, 070907 (2021).
[163]G. Sinatkas, T. Christopoulos, O. Tsilipakos, and E. E. Kriezis, "Electro-optic modulation in integrated photonics," J. Appl. Phys. **130**, 010901 (2021).
[164]X. Hu, D. Wu, Y. Zhang, H. Zhang, D. Chen, M. Liu, J. Liu, L. Wang, X. Xiao, and S. Yu, "110 Gbit/s NRZ and 160 Gbit/s PAM-4 GeSi electro-absorption modulator," in *2022 Optical Fiber Communications Conference and Exhibition (OFC)* (Optica Publishing Group, 2022), paper Th3C.4.
[165]Y. Kuo, Y. K. Lee, Y. Ge, S. Ren, J. E. Roth, T. I. Kamins, D. A. B. Miller, and J. S. Harris, "Strong quantum-confined Stark effect in germanium quantum-well structures on silicon," Nature **437**, 1334–1336 (2005).
[166]S. A. Srinivasan, C. Porret, S. Balakrishnan, Y. Ban, R. Loo, P. Verheyen, J. Van Campenhout, and M. Pantouvaki, "60 Gb/s waveguide-coupled O-band GeSi quantum-confined stark effect electro-absorption modulator," in *Optical Fiber Communication Conference (OFC)* (Optica Publishing Group, 2021), paper Tu1D.3.
[167]X. Wang, S. Yu, J. Qin, A. Cuervo-Covian, H. Zuo, X. Sun, J. Hu, T. Gu, and J. Liu, "Low-voltage, coupled multiple quantum well electroreflective modulators

towards ultralow power inter-chip optical interconnects," J. Lightwave Technol. **38**, 3414–3421 (2020).
[168]R. Soref and B. Bennett, "Electrooptical effects in silicon," IEEE J. Quantum Electron. **23**(1), 123–129 (1987).
[169]F. Y. Gardes, G. T. Reed, N. G. Emerson, and C. E. Png, "A sub-micron depletion-type photonic modulator in silicon on insulator," Opt. Express **13**, 8845–8854 (2005).
[170]A. Rahim, A. Hermans, B. Wohlfeil, D. Petousi, B. Kuyken, D. Van Thourhout, and R. Baets, "Taking silicon photonics modulators to a higher performance level: State-of-the-art and a review of new technologies," Adv. Photonics **3**, 024003 (2021).
[171]G. T. Reed, S. Liu, D. J. Thomson, W. Zhang, F. Meng, X. Yan, C. G. Littlejohns, H. Du, W. Cao, M. Banakar, M. Ebert, V. Jeyaselvan, D. Tran, P. Petropoulos, and L. Ke, "Beyond 100 Gb/s from a single silicon MZI modulator," in *Conference on Lasers and Electro-Optics, Technical Digest Series* (Optica Publishing Group, 2022), p. SM5G.1.
[172]M. L. Lee, E. A. Fitzgerald, M. T. Bulsara, M. T. Currie, and A. Lochtefeld, "Strained Si, SiGe, and Ge channels for high-mobility metal-oxide-semiconductor field-effect transistors," J. Appl. Phys. **97**, 011101 (2005).
[173]M. V. Fischetti and S. E. Laux, "Band structure, deformation potentials, and carrier mobility in strained Si, Ge, and SiGe alloys," J. Appl. Phys. **80**, 2234 (1996).
[174]Y. Kim, M. Takenaka, T. Osada, M. Hata, and S. Takagi, "Strain-induced enhancement of plasma dispersion effect and free-carrier absorption in SiGe optical modulators," Sci. Rep. **4**, 4683 (2014).
[175]Y. Lin, D. Ma, K. H. Lee, R.-T. Wen, G. Syaranamual, L. C. Kimerling, C. S. Tan, and J. Michel, "PIC-integrable, uniformly tensile-strained Ge-on-insulator photodiodes enabled by recessed SiN_x stressor," Photonics Res. **9**, 1255–1263 (2021).
[176]W. C. Hsu, N. Nujhat, B. Kupp, J. F. Conley, H. Rong, R. Kumar, and A. X. Wang, "Sub-volt high-speed silicon MOSCAP microring modulator driven by high-mobility conductive oxide," Nat. Commun. **15**, 826 (2024).
[177]C. Wang, M. Zhang, X. Chen, M. Bertrand, A. Shams-Ansari, S. Chandrasekhar, P. Winzer, and M. Lončar, "Integrated lithium niobate electro-optic modulators operating at CMOS-compatible voltages," Nature **562**, 101–104 (2018).
[178]R. S. Jacobsen, K. N. Andersen, P. I. Borel, J. Fage-Pedersen, L. H. Frandsen, O. Hansen, M. Kristensen, A. V. Lavrinenko, G. Moulin, H. Ou, C. Peucheret, B. Zsigri, and A. Bjarklev, "Strained silicon as a new electro-optic material," Nature **441**, 199–202 (2006).
[179]J. B. Khurgin, T. H. Stievater, M. W. Pruessner, and W. S. Rabinovich, "On the origin of the second-order nonlinearity in strained Si–SiN structures," J. Opt. Soc. Am. B **32**, 2494–2499 (2015).
[180]P. Damas, M. Berciano, G. Marcaud, C. A. Ramos, D. Marris-Morini, E. Cassan, and L. Vivien, "Comprehensive description of the electro-optic effects in strained silicon waveguides," J. Appl. Phys. **122**, 153105 (2017).
[181]B. Zabelich, E. Nitiss, A. Stroganov, and C.-S. Brès, "Linear electro-optic effect in silicon nitride waveguides enabled by electric-field poling," ACS Photonics **9**(10), 3374–3383 (2022).
[182]Y. Zhang, J. Nauriyal, M. Song, M. G. Baez, X. He, T. Macdonald, and J. Cardenas, "Engineered second-order nonlinearity in silicon nitride," Opt. Mater. Express **13**(1), 237 (2023).
[183]A. N. R. Ahmed, S. Shi, A. Mercante, S. Nelan, P. Yao, and D. W. Prather, "High-efficiency lithium niobate modulator for K band operation," APL Photonics **5**, 091302 (2020).
[184]X. Huang, Y. Liu, Z. Li, Z. Fan, and W. Han, "High-performance and compact integrated photonics platform based on silicon rich nitride-lithium niobate on insulator," APL Photonics **6**, 116102 (2021).
[185]D. Zhu, L. Shao, M. Yu, R. Cheng, B. Desiatov, C. J. Xin, Y. Hu, J. Holzgrafe, S. Ghosh, A. Shams-Ansari, E. Puma, N. Sinclair, C. Reimer, M. Zhang, and M. Lončar, "Integrated photonics on thin-film lithium niobate," Adv. Opt. Photonics **13**, 242–352 (2021).
[186]N. Boynton, H. Cai, M. Gehl, S. Arterburn, C. Dallo, A. Pomerene, A. Starbuck, D. Hood, D. C. Trotter, T. Friedmann, C. T. DeRose, and A. Lentine, "A heterogeneously integrated silicon photonic/lithium niobate travelling wave electro-optic modulator," Opt. Express **28**, 1868–1884 (2020).
[187]A. N. R. Ahmed, S. Nelan, S. Shi, P. Yao, A. Mercante, and D. W. Prather, "Subvolt electro-optical modulator on thin-film lithium niobate and silicon nitride hybrid platform," Opt. Lett. **45**, 1112–1115 (2020).
[188]M. He, M. Xu, Y. Ren, J. Jian, Z. Ruan, Y. Xu, S. Gao, S. Sun, X. Wen, L. Zhou, L. Liu, C. Guo, H. Chen, S. Yu, L. Liu, and X. Cai, "High-performance hybrid silicon and lithium niobate Mach–Zehnder modulators for 100 $Gbits^{-1}$ and beyond," Nat. Photonics **13**, 359–364 (2019).
[189]P. Kharel, C. Reimer, K. Luke, L. He, and M. Zhang, "Breaking voltage–bandwidth limits in integrated lithium niobate modulators using micro-structured electrodes," Optica **8**, 357–363 (2021).
[190]F. A. Juneghani, M. G. Vazimali, J. Zhao, X. Chen, S. T. Le, H. Chen, E. Ordouie, N. K. Fontaine, and S. Fathpour, "Thin-film lithium niobate optical modulators with an extrapolated bandwidth of 170 GHz," Adv. Photonics Res. **4**, 2200216 (2023).
[191]L. Cai, A. Mahmoud, and G. Piazza, "Low-loss waveguides on Y-cut thin film lithium niobate: Towards acousto-optic applications," Opt. Express **27**, 9794–9802 (2019).
[192]A. Shams-Ansari, G. Huang, L. He, Z. Li, J. Holzgrafe, M. Jankowski, M. Churaev, P. Kharel, R. Cheng, D. Zhu, N. Sinclair, B. Desiatov, M. Zhang, T. J. Kippenberg, and M. Lončar, "Reduced material loss in thin-film lithium niobate waveguides," APL Photonics **7**, 081301 (2022).
[193]D. Zhu, L. Shao, M. Yu, R. Cheng, B. Desiatov, C. J. Xin, Y. Hu, J. Holzgrafe, S. Ghosh, A. Shams-Ansari, E. Puma, N. Sinclair, C. Reimer, M. Zhang, and M. Lončar, "Integrated photonics on thin-film lithium niobate," Adv. Opt. Photonics **13**, 242–352 (2021).
[194]F. Eltes, C. Mai, D. Caimi, M. Kroh, Y. Popoff, G. Winzer, D. Petousi, S. Lischke, J. E. Ortmann, L. Czornomaz, L. Zimmermann, J. Fompeyrine, and S. Abel, "A $BaTiO_3$-based electro-optic Pockels modulator monolithically integrated on an advanced silicon photonics platform," J. Lightwave Technol. **37**, 1456–1462 (2019).
[195]A. B. Posadas, H. Park, M. Reynaud, W. Cao, J. D. Reynolds, W. Guo, V. Jeyaselva, I. Beskin, G. Z. Mashanovich, J. H. Warner, and A. A. Demkov, "Thick $BaTiO_3$ epitaxial films integrated on Si by RF sputtering for electro-optic modulators in Si photonics," ACS Appl. Mater. Interfaces **13**, 51230–51244 (2021).
[196]S. Abel, F. Eltes, J. E. Ortmann, A. Messner, P. Castera, T. Wagner, D. Urbonas, A. Rosa, A. M. Gutierrez, D. Tulli, P. Ma, B. Baeuerle, A. Josten, W. Heni, D. Caimi, L. Czornomaz, A. A. Demkov, J. Leuthold, P. Sanchis, and J. Fompeyrine, "Large Pockels effect in micro- and nanostructured barium titanate integrated on silicon," Nat. Mater. **18**, 42–47 (2019).
[197]M. Kohli, D. Chelladurai, A. Messner, Y. Horst, D. Moor, J. Winiger, T. Blatter, T. Buriakova, C. Convertino, F. Eltes, M. Zervas, Y. Fedoryshyn, U. Koch, and J. Leuthold, "Plasmonic ferroelectric modulator monolithically integrated on SiN for 216 GBd data transmission," J. Lightwave Technol. **41**(12), 3825–3831 (2023).
[198]M. Kohli, D. Chelladurai, L. Kulmer, A. Messner, K. Keller, T. Blatter, J. Winiger, D. Moor, T. Buriakova, M. Zervas, C. Convertino, F. Eltes, Y. Fedoryshyn, U. Koch, and J. Leuthold, "Barium titanate racetrack modulator on silicon nitride for 200 GBd data communication in the O-band," in *CLEO 2024, Technical Digest Series* (Optica Publishing Group, 2024), p. SW4R.4.
[199]M. Eppenberger, A. Messner, B. I. Bitachon, W. Heni, T. Blatter, P. Habegger, M. Destraz, E. De Leo, N. Meier, N. Del Medico, C. Hoessbacher, B. Baeuerle, and J. Leuthold, "Resonant plasmonic micro-racetrack modulators with high bandwidth and high temperature tolerance," Nat. Photonics **17**, 360–367 (2023).
[200]F. Eltes, W. Li, E. Berikaa, M. S. Alam, S. Bernal, C. Minkenberg, D. V. Plant, and S. Abel, "Thin-film BTO-based modulators enabling 200 Gb/s data rates with sub 1 Vpp drive signal," in *2023 Optical Fiber Communications Conference and Exhibition (OFC)*, San Diego, CA, USA (Optica Publishing Group, 2023), p. Th4A.2.

[201]A. Rosa, D. Tulli, P. Castera, A. M. Gutierrez, A. Griol, M. Baquero, B. Vilquin, F. Eltes, S. Abel, J. Fompeyrine, and P. Sanchis, "Barium titanate ($BaTiO_3$) RF characterization for application in electro-optic modulators," Opt. Mater. Express **7**, 4328–4336 (2017).
[202]A. Messner, F. Eltes, P. Ma, S. Abel, B. Baeuerle, A. Josten, W. Heni, D. Caimi, J. Fompeyrine, and J. Leuthold, "Plasmonic ferroelectric modulators," J. Lightwave Technol. **37**(2), 281–290 (2019).
[203]J. Shen, Y. Zhang, Y. Chen, W. Zhou, X. Zhang, M. Sun, X. Wang, L. Zhang, X. Li, J. Li, and Y. Su, "Integrated Pockels modulators on silicon photonics platform," Adv. Phys. Res. **4**, 2400096 (2025).
[204]G. Yang, H. Wang, S. Mu, H. Xie, T. Wang, C. He, M. Shen, M. Liu, C. G. Van de Walle, and H. X. Tang, "Unveiling the Pockels coefficient of ferroelectric nitride ScAlN," Nat. Commun. **15**, 9538 (2024).
[205]H. Miura, F. Qiu, A. M. Spring, T. Kashino, T. Kikuchi, M. Ozawa, H. Nawata, K. Odoi, and S. Yokoyama, "High thermal stability 40 GHz electro-optic polymer modulators," Opt. Express **25**, 28643–28649 (2017).
[206]A. Karvounis, F. Timpu, V. V. Vogler-Neuling, R. Savo, and R. Grange, "Barium titanate nanostructures and thin films for photonics," Adv. Opt. Mater. **8**, 2001249 (2020).
[207]X. B. Xie, I. Shubin, W. S. C. Chang, and P. K. L. Yu, "Analysis of linearity of highly saturated electroabsorption modulator link due to photocurrent feedback effect," Opt. Express **15**, 8713–8718 (2007).
[208]Y. Chiu and J. Wu, "High-speed low-driving-power electroabsorption modulator for microwave photonic communications," in *2013 18th OptoElectronics and Communications Conference Held Jointly with 2013 International Conference on Photonics in Switching* (Optica Publishing Group, 2013), p. WK2_1.
[209]N.-N. Feng, D. Feng, S. Liao, X. Wang, P. Dong, H. Liang, C.-C. Kung, W. Qian, J. Fong, R. Shafiiha, Y. Luo, J. Cunningham, A. V. Krishnamoorthy, and M. Asghari, "30 GHz Ge electro-absorption modulator integrated with 3 μm silicon-on-insulator waveguide," Opt. Express **19**, 7062–7067 (2011).
[210]D. Feng, S. Liao, H. Liang, J. Fong, B. Bijlani, R. Shafiiha, B. Jonathan Luff, Y. Luo, J. Cunningham, A. V. Krishnamoorthy, and M. Asghari, "High speed GeSi electro-absorption modulator at 1550 nm wavelength on SOI waveguide," Opt. Express **20**, 22224–22232 (2012).
[211]D. Feng, W. Qian, H. Liang, C.-C. Kung, Z. Zhou, Z. Li, J. S. Levy, R. Shafiiha, J. Fong, B. Jonathan Luff, and M. Asghari, "High-speed GeSi electro-absorption modulator on the SOI waveguide platform," IEEE J. Sel. Top. Quantum Electron. **19**(6), 64–73 (2013).
[212]A. V. Krishnamoorthy, X. Zheng, D. Feng, J. Lexau, J. F. Buckwalter, H. D. Thacker, F. Liu, Y. Luo, E. Chang, P. Amberg, I. Shubin, S. S. Djordjevic, J. H. Lee, S. Lin, H. Liang, A. Abed, R. Shafiiha, K. Raj, R. Ho, M. Asghari, and J. E. Cunningham, "A low-power, high-speed, 9-channel germanium-silicon electro-absorption modulator array integrated with digital CMOS driver and wavelength multiplexer," Opt. Express **22**, 12289–12295 (2014).
[213]S. Gupta, S. A. Srinivasan, M. Pantouvaki, H. Chen, P. Verheyen, G. Lepage, D. Van Thourhout, G. Roelkens, K. Saraswat, P. Absil, and J. Van Campenhout, "50 GHz Ge waveguide electro-absorption modulator integrated in a 220 nm SOI photonics platform," in *2015 Optical Fiber Communications Conference and Exhibition (OFC)*, Los Angeles, CA, USA (Optica Publishing Group, 2015), Paper No. Tu2A.4, pp. 1–3.
[214]S. A. Srinivasan, M. Pantouvaki, S. Gupta, H. T. Chen, P. Verheyen, G. Lepage, G. Roelkens, K. Saraswat, D. V. Thourhout, P. Absil, and J. V. Campenhout, "56 Gb/s germanium waveguide electro-absorption modulator," J. Lightwave Technol. **34**(2), 419–424 (2016).
[215]P. De Heyn, V. I. Kopp, S. A. Srinivasan, P. Verheyen, J. Park, M. S. Wlodawski, J. Singer, D. Neugroschl, B. Snyder, S. Balakrishnan, G. Lepage, M. Pantouvaki, P. Absil, and J. Van Campenhout, "Ultra-dense 16 × 56 Gb/s NRZ GeSi EAM-PD arrays coupled to multicore fiber for short-reach 896 Gb/s optical links," in *Optical Fiber Communication Conference, OSA Technical Digest (Online)* (Optica Publishing Group, 2017), p. Th1B.7.
[216]J. Liu, D. Pan, S. Jongthammanurak, K. Wada, L. C. Kimerling, and J. Michel, "Design of monolithically integrated GeSi electro-absorption modulators and photodetectors on an SOI platform," Opt. Express **15**, 623–628 (2007).
[217]J. Verbist, M. Verplaetse, S. A. Srivinasan, P. De Heyn, T. De Keulenaer, R. Pierco, and J. Bauwelinck, "First real-time 100-Gb/s NRZ-OOK transmission over 2 km with a silicon photonic electro-absorption modulator," in *2017 Optical Fiber Communications Conference and Exhibition (OFC)*, Los Angeles, CA, USA (Optica Publishing Group, 2017), Paper No. Th5C.4.
[218]Y. Liu, J. Sun, R. Song, X. Li, J. Wang, S. Wang, Y. Yu, W. Yue, Y. Cai, and M. Yu, "80 Gb/s NRZ Ge waveguide electro-absorption modulator," Opt. Express **30**, 34276–34286 (2022).
[219]D. W. U. Chan, G. Zhou, X. Wu, Y. Tong, J. Zhang, C. Lu, A. P. T. Lau, and H. K. Tsang, "A compact 112-Gbaud PAM-4 silicon photonics transceiver for short-reach interconnects," J. Lightwave Technol. **40**(8), 2265–2273 (2022).
[220]A. Tsiara, S. A. Balakrishnan, S. Pantouvaki, M. Absil, J. Van Campenhout, and K. Croes, "Electrical and optical reliability analysis of GeSi electro-absorption modulators," in *Proceedings of the Optical Fiber Communication Conference* (Optica Publishing Group, 2020), p. M2A.5.
[221]A. Tsiara, A. Lesniewska, P. Roussel, S. A. Srinivasan, M. Berciano, M. Simicic, M. Pantouvaki, J. Van Campenhout, Croes Kristof, "Degradation mechanisms in germanium electro-absorption modulators," *2022 IEEE International Reliability Physics Symposium (IRPS)*, Dallas, TX, USA (IEEE, 2022), pp. 9A.2-1–9A.2-7.
[222]J. Fujikata, M. Noguchi, R. Katamawari, K. Inaba, H. Ono, D. Shimura, Y. Onawa, H. Yaegashi, and Y. Ishikawa, "High-performance Ge/Si electro-absorption optical modulator up to 85 °C and its highly efficient photodetector operation," Opt. Express **31**, 10732–10743 (2023).
[223]M.-S. Rouifed, D. Marris-Morini, P. Chaisakul, J. Frigerio, G. Isella, and D. Chrastina, "Advances toward Ge/SiGe quantum-well waveguide modulators at 1.3 μm," IEEE J. Sel. Top. Quantum Electron. **20**, 3400207 (2014).
[224]A. Kandeel, G. Hiblot, C. Porret, S. A. Srinivasan, A. Milenin, S. Balakrishnan, M. Berciano, R. Loo, D. Van Thourhout, M. Pantouvaki, F. Ferraro, Y. Ban, and J. Van Campenhout, "Low-Capacitance, high-speed O-band GeSi quantum-confined stark effect electro absorption modulator," in *Frontiers in Optics + Laser Science 2022 (FIO, LS), Technical Digest Series* (Optica Publishing Group, 2022), p. FTu6C.2.
[225]I. Skandalos, T. D. Bucio, L. Mastronardi, G. Yu, A. Zilkie, and F. Y. Gardes, "A 100 Gb/s quantum-confined Stark effect modulator monolithically integrated with silicon nitride on Si," Commun. Eng. **4**, 82 (2025).
[226]S. Jongthammanurak, J. Liu, K. Wada, D. D. Cannon, D. T. Danielson, D. Pan, L. C. Kimerling, and J. Michel, "Large electro-optic effect in tensile strained Ge-on-Si films," Appl. Phys. Lett. **89**(16), 161115 (2006).
[227]C. N. Tseng, A. Kandeel, M. Berciano, D. Malik, H. Kobbi, D. Yudistira, D. Van Thourhout, M. Chakrabarti, D. Velenis, P. Verheyen, Y. Ban, F. Ferraro, and J. Van Campenhout, "Strong phase modulation in integrated O-band GeSi-QCSE waveguide modulators," in *2024 Conference of Laser and Electro-Optics (CLEO 2024), Technical Digest Series* (Optica Publishing Group, 2024), p. SW4R.1.
[228]X. Wang, S. Yu, H. Zuo, X. Sun, J. Hu, T. Gu, and J. Liu, "Design of hybrid plasmonic multi-quantum-well electro-reflective modulators towards <100 fJ/bit photonic links," IEEE J. Sel. Top. Quantum Electron. **27**, 1 (2021).
[229]D. Pan, J. Liu, L. C. Kimerling, J. F. McMillan, M. D. Sockin, and C. W. Wong, "Ultrafast Ge/Si resonator-based modulators for optical data communications in silicon photonics," U.S. Patent US7,840,099 B2 (2010).
[230]X. Zhang, K. Kwon, J. Henriksson, J. Luo, and M. C. Wu, "A large-scale microelectromechanical-systems-based silicon photonics LiDAR," Nature **603**, 253–258 (2022).
[231]Y. Ishikawa, K. Wada, D. D. Cannon, J. Liu, H.-C. Luan, and L. C. Kimerling, "Strain-induced band gap shrinkage in Ge grown on Si substrate," Appl. Phys. Lett. **82**(13), 2044–2046 (2003).
[232]J. Liu, D. D. Cannon, K. Wada, Y. Ishikawa, D. T. Danielson, S. Jongthammanurak, J. Michel, and L. C. Kimerling, "Deformation potential constants of biaxially tensile stressed Ge epitaxial films on Si (100)," Phys. Rev. B **70**, 155309 (2004).
[233]J. Liu, D. D. Cannon, K. Wada, Y. Ishikawa, S. Jongthammanurak, D. T. Danielson, J. Michel, and L. C. Kimerling, "Silicidation-induced band gap shrinkage in Ge epitaxial films on Si," Appl. Phys. Lett. **84**(5), 660–662 (2004).

[234]J. F. Liu, D. Pan, S. Jongthammanurak, D. Ahn, C. Y. Hong, M. Beals, L. C. Kimerling, J. Michel, T. Pomerene, C. Hill, M. Jaso, K. Y. Tu, Y. K. Chen, S. Patel, M. Rasras, A. White, and D. M. Gill, "Waveguide-Integrated Ge p-i-n photodetectors on SOI platform," in *3rd IEEE International Conference on Group IV Photonics, 2006*, Ottawa, ON, Canada (IEEE, 2006), pp. 173–175.
[235]J. Michel, J. Liu, and L. C. Kimerling, "High-performance Ge-on-Si photodetectors," Nat. Photonics **4**, 527–534 (2010).
[236]See https://www.aimphotonics.com/base-active-pic for information about basic active photonic integrated circuits (PIC) at American Institute for Manufacturing Photonics.
[237]S. Lischke, A. Peczek, J. S. Morgan, K. Sun, D. Steckler, Y. Yamamoto, F. Korndörfer, C. Mai, S. Marschmeyer, M. Fraschke, A. Krüger, A. Beling, and L. Zimmermann, "Ultra-fast germanium photodiode with 3-dB bandwidth of 265 GHz," Nat. Photonics **15**, 925–931 (2021).
[238]Y. Li, X. Luo, G. Liang and G. -Q. Lo, "Demonstration of Ge/Si avalanche photodetector arrays for lidar application," in *2019 Optical Fiber Communications Conference and Exhibition (OFC)* (Optica Publishing Group, 2019), Paper No. Tu3E.3.
[239]P. Vines, K. Kuzmenko, J. Kirdoda, D. C. S. Dumas, M. M. Mirza, R. W. Millar, D. J. Paul, and G. S. Buller, "High performance planar germanium-on-silicon single-photon avalanche diode detectors," Nat. Commun. **10**, 1086 (2019).
[240]L. Bogaert, K. Van Gasse, T. Spuesens, G. Torfs, J. Bauwelinck, and G. Roelkens, "Silicon photonics traveling wave photodiode with integrated star coupler for high-linearity mm-wave applications," Opt. Express **26**, 34763–34775 (2018).
[241]M. Piels and J. E. Bowers, "40 GHz Si/Ge uni-traveling carrier waveguide photodiode," J. Lightwave Technol. **32**(20), 3502–3508 (2014).
[242]A. Beling and J. C. Campbell, "InP-based high-speed photodetectors," J. Lightwave Technol. **27**(3), 343–355 (2009).
[243]K. Sun and A. Beling, "High-speed photodetectors for microwave photonics," Appl. Sci. **9**, 623 (2019).
[244]M. R. Atalla, S. Assali, A. Attiaoui, C. Lemieux-Leduc, A. Kumar, S. Abdi, and O. Moutanabbir, "All-group IV transferable membrane mid-infrared photodetectors," Adv. Funct. Mater. **31**, 2006329 (2021).
[245]E. Talamas Simola, V. Kiyek, A. Ballabio, V. Schlykow, F. Frigerio, C. Zucchetti, A. De Lacovo, L. Colace, Y. Yamamoto, G. Capellini, and D. Grützmacher, "CMOS-compatible bias-tunable dual-band detector based on GeSn/Ge/Si coupled photodiodes," ACS Photonics **8**, 2166–2173 (2021).
[246]H. Zhou, L. Zhang, J. Tong, S. Wu, D. Son, Q. Chen, D. H. Zhang, and C. S. Tan, "Surface plasmon enhanced GeSn photodetectors operating at 2 μm," Opt. Express **29**, 8498–8509 (2021).
[247]G.-E. Chang, S.-Q. Yu, and G. Sun, "'GeSn Rule-23'—The performance limit of GeSn infrared photodiodes," Sensors **23**, 7386 (2023).
[248]Q. M. Chen, H. Zhou, S. Q. Xu, Y. C. Huang, S. T. Wu, K. H. Lee, X. Gong, and C. S. Tan, "A route toward high-detectivity and Low-cost short-wave infrared photodetection: GeSn/Ge multiple-quantum-well photodetectors with a dielectric nanohole array metasurface," ACS Nano **17**(13), 12151–12159 (2023).
[249]H. Tran, T. Pham, J. Margetis, Y. Zhou, W. Dou, P. C. Grant, J. M. Grant, S. Al-Kabi, G. Sun, R. A. Soref, J. Tolle, Y.-H. Zhang, W. Du, B. Li, M. Mortazavi, and S.-Q. Yu, "Si-based GeSn photodetectors toward mid-infrared imaging applications," ACS Photonics **6**, 2807–2815 (2019).
[250]Z. Li, A. M. Heidt, J. M. O. Daniel, Y. Jung, S. U. Alam, and D. J. Richardson, "Thulium-doped fiber amplifier for optical communications at 2 μm," Opt. Express **21**, 9289–9297 (2013).
[251]M. R. M. Atalla, S. Assali, S. Koelling, A. Attiaoui, and O. Moutanabbir, "High-bandwidth extended-SWIR GeSn photodetectors on silicon achieving ultrafast broadband spectroscopic response," ACS Photonics **9**(4), 1425–1433 (2022).
[252]Q. M. Chen, H. Zhou, S. Q. Xu, Y. C. Huang, S. T. Wu, K. H. Lee, X. Gong, and C. S. Tan, "A route toward high-detectivity and low-cost short-wave infrared photodetection: GeSn/Ge multiple-quantum-well photodetectors with a dielectric nanohole array metasurface," ACS Nano. **17**(13), 12151–12159 (2023).
[253]J. Zheng, X. Liu, J. Cui, Q. Huang, Z. Liu, Y. Zuo, and B. Cheng, "Research progress of GeSn photodetectors for infrared application," IEEE J. Sel. Top. Quantum Electron. **31**(1), 3800609 (2025).
[254]S. Fu, H. Wang, X. Wang, Y. Song, J. Kong, and J. Liu, "Self-assembled, ultra-high refractive index pseudo-periodic Sn nanostructures for broad-band infrared photon management in single layer graphene," ACS Photonics **6**, 50–58 (2019).
[255]X. Wang, A. Wong, S. Malek, Y. Cai, and J. Liu, "High-performance infrared light trapping in nano-needle structured p^+ SnO_x ($x \leq 1$)/thin film n-Ge photodiodes on Si," Opt. Lett. **40**, 2603–2606 (2015).
[256]S. Fu, X. Wang, H. Wang, X. Gao, K. Broderick, J. Kong, and J. Liu, "An optical slot-antenna-coupled cavity (SAC) framework towards tunable free-space graphene photonic surfaces," Nano Res. **14**(5), 1364–1373 (2021).
[257]Z. Wang, X. Wang, and J. Liu, "An efficient nanophotonic hot electron solar-blind UV detector," ACS Photonics **5**, 3989–3995 (2018).
[258]X. Gao, S. Fu, T. Fang, X. Yu, H. Wang, Q. Ji, J. Kong, X. Wang, and J. Liu, "Synergistic photon management and strain-induced band gap engineering of two-dimensional MoS2 using semimetal composite nanostructures," ACS Appl. Mater. Interfaces **15**(19), 23564 (2023).
[259]K.-C. Lee, M.-X. Lin, H. Li, H.-H. Cheng, G. Sun, R. Soref, J. R. Hendrickson, K.-M. Hung, P. Scajec, and A. Medvids, "Planar GeSn photodiode for high-detectivity photodetection at 1550 nm," Appl. Phys. Lett. **117**, 012102 (2020).
[260]S. Liu, A. C. Covian, J. A. Gardener, A. Akey, B. D. A. Levin, X. Wang, and J. Liu, "Growth of α-Sn on silicon by a reversed β-Sn to α-Sn phase transformation for quantum material integration," Commun. Mater. **3**, 17 (2022).
[261]J. Jeong, Q. Wang, J. Cha, D. K. Jin, D. H. Shin, S. Kwon, B. K. Kang, J. H. Jang, W. S. Yang, Y. S. Choi, J. Yoo, J. K. Kim, C.-H. Lee, S. W. Lee, A. Zakhidov, S. Hong, M. J. Kim, and Y. J. Hong, "Remote heteroepitaxy of GaN microrod heterostructures for deformable light-emitting diodes and wafer recycle," Sci. Adv. **6**, eaaz5180 (2020).
[262]D. O. Alshahrani, M. Kesaria, E. A. Anyebe, V. Srivastava, and D. I. Huffaker, "Emerging type-II superlattices of InAs/InAsSb and InAs/GaSb for Mid-wavelength infrared photodetectors," Adv. Photonics Res. **3**, 2100094 (2022).
[263]J. Rudie, S. Amoah, X. Wang, R. Kumar, G. Abernathy, S. Akwabli, P. C. Grant, J. Liu, B. Li, W. Du, and S.-Q. Yu, "Development of monolithic germanium–tin on Si avalanche photodiodes for infrared detection," IEEE J. Sel. Top. Quantum Electron. **31**, 1 (2025).
[264]E. R. Fossum, J. Ma, S. Masoodian, L. Anzagira, and R. Zizza, "The quantum image sensor: Every photon counts," Sensors **16**, 1260 (2016).
[265]E. R. Fossum, J. Ma, S. Masoodian, L. Anzagira, and R. Zizza, "The quanta image sensor: Every photon counts," Sensors **16**, 1260 (2016).
[266]J. Ma, S. Masoodian, D. A. Starkey, and E. R. Fossum, "Photon-number-resolving megapixel image sensor at room temperature without avalanche gain," Optica **4**, 1474–1481 (2017).
[267]A. Migdall, "Pushing single-photon detection to the limits (and perhaps beyond)," in *IEEE Photonics Society Summer Topical Meeting* (IEEE, 2017) p. MF4.3.
[268]J. Ma, D. Zhang, O. A. Elgendy, and S. Masoodian, "A 0.19e-rms read noise 16.7 Mpixel stacked quanta image sensor with 1.1 μm-pitch backside illuminated pixels," IEEE Electron Device Lett. **42**, 891–894 (2021).
[269]E. R. Fossum, N. Teranishi, and A. J. P. Theuwissen, "Digital image sensor evolution and new frontiers," Ann. Rev. Vision Sci. **10**(1), 171–198 (2024).
[270]J. Zhang, J. Newman, Z. Wang, Y. Qian, P. Feliciano-Ramos, W. Guo, T. Honda, Z. S. Chen, C. Linghu, R. Etienne-Cummings, E. Fossum, E. Boyden, and M. Wilson, "Pixel-wise programmability enables dynamic high-SNR cameras for high-speed microscopy," Nat. Commun. **15**, 4480 (2024).
[271]C. Rogers, A. Y. Piggott, D. J. Thomson, R. F. Wiser, I. E. Opris, S. A. Fortune, A. J. Compston, A. Gondarenko, F. Meng, X. Chen, G. T. Reed, and R. Nicolaescu, "A universal 3D imaging sensor on a silicon photonics platform," Nature **590**, 256–261 (2021).
[272]S. Liu, J. Feng, Y. Tian, H. Zhao, L. Jin, B. Ouyang, J. Zhu, and J. Guo, "Thermo-optic phase shifters based on silicon-on-insulator platform: State-of-the-art and a review," Front. Optoelectron. **15**, 9 (2022).

[273]X. Chen, F. Meng, S. A. Fortune, A. J. Compston, M. Ebert, X. Yan, H. Du, M. Banakar, D. T. Tran, C. G. Littlejohns, D. J. Thomson, R. Nicolaescu, and G. T. Reed, "Silicon photonic beam steering module with backside coupling elements toward dense heterogeneous integration with drive electronics," APL Photonics **6**, 116106 (2021).
[274]K. Kuzmenko, P. Vines, A. Halimi, R. J. Collins, A. Maccarone, A. Mccarthy, Z. M. Greener, J. Kirdoda, D. C. S. Dumas, L. F. Llin, M. M. Mirza, R. W. Millar, D. J. Paul, and G. S. Buller, "3D LiDAR imaging using Ge-on-Si single-photon avalanche diode detectors," Opt. Express **28**, 1330–1344 (2020).
[275]X. Sun, L. Zhang, Q. Zhang, and W. Zhang, "Si photonics for practical LiDAR solutions," Appl. Sci. **9**, 4225 (2019).
[276]E. Lee, K. M. Anagnost, Z. Wang, M. R. James, E. R. Fossum, and J. Liu, "Monte Carlo modeling and design of photon energy attenuation layers for >10× quantum yield enhancement in Si-based hard X-ray detectors," Instruments **5**(2), 17 (2021).
[277]E. Lee, K. D. Larkin, X. Yue, Z. Wang, E. R. Fossum, and J. Liu, "Design of monolithic Bi-layer high-Z PAL-Si hard X-ray CMOS image sensors for quantum efficiency enhancement," Instruments **7**, 24 (2023).
[278]J. K. Doylend and S. Gupta, "An overview of silicon photonics for LIDAR," Proc. SPIE **11285**, 112850J (2020).
[279]P. Bhargava, T. Kim, C. V. Poulton, J. Notaros, A. Yaacobi, E. Timurdogan, C. Baiocco, N. Fahrenkopf, S. Kruger, T. Ngai, Y. Timalsina, M. R. Watts, and V. Stojanovic, "Fully integrated coherent LiDAR in 3D-integrated silicon photonics/65 nm CMOS," in *2019 Symposium on VLSI Circuits* (IEEE, 2019), pp. C262–C263.
[280]See https://optics.org/news/12/7/19 for information about "AEye lidar test confirms 1-kilometer range."
[281]M. R. Watts, C. Poulton, M. Byrd, and G. Smolka, "Lidar on a chip enters the fast lane: Sensors for self-driving cars and robots will be tiny, reliable, and affordable," IEEE Spectr. **60**, 38–43 (2023).
[282]J. Luff and M. Asghari, "Silicon photonics for FMCW LIDAR," Proc. SPIE **PC12006**, PC1200605 (2022).
[283]S. Chung, M. Nakai, S. Idres, Y. Ni, and H. Hashemi, "Optical phased-array FMCW LiDAR with on-chip calibration," *2021 IEEE International Solid- State Circuits Conference (ISSCC)* (IEEE, 2021), pp. 286–288.
[284]R. Nicolaescu, C. Rogers, A. Y. Piggott, D. J. Thomson, I. E. Opris, S. A. Fortune, A. J. Compston, A. Gondarenko, F. Meng, X. Chen, and G. T. Reed, "3D imaging via silicon-photonics-based LIDAR," Proc. SPIE **11691**, 116810G (2021).
[285]See https://www.fda.gov/regulatory-information/search-fda-guidance-documents/laser-products-conformance-iec-60825-1-ed-3-and-iec-60601-2-22-ed-31-laser-notice-no-56 for information about eye safety standard IEC 60825-1.
[286]S. Aboujja, S. Pappas, and D. Chu, "High reliability of 1550 nm triple junction laser diode for long-range automotive LiDAR," Proc. SPIE **12403**, 1240308 (2023).
[287]M. De Zoysa, R. Sakata, K. Ishizaki, T. Inoue, M. Yoshida, J. Gelleta, Y. Mineyama, T. Akahori, S. Aoyama, and S. Noda, "Non-mechanical three-dimensional LiDAR system based on flash and beam-scanning dually modulated photonic crystal lasers," Optica **10**, 264–268 (2023).
[288]Z. Wang, X. Liu, P. Wang, H. Lu, B. Meng, W. Zhang, L. Wang, Y. Wang, and C. Tong, "Continuous-wave operation of 1550 nm low-threshold triple-lattice photonic-crystal surface-emitting lasers," Light Sci. Appl. **13**, 44 (2024).
[289]See https://www.aeva.com/press/aeva-introduces-atlas-the-first-automotive-grade-4d-lidar-sensor-for-mass-production-automotive-applications/ for information about Frequency Modulated Continuous Wave (FMCW) 4D LiDAR technology.
[290]N. Na, S.-L. Cheng, H.-D. Liu, M.-J. Yang, C.-Y. Chen, H.-W. Chen, Y.-T. Chou, C.-T. Lin, W.-H. Liu, C.-F. Liang, C.-L. Chen, S.-W. Chu, B.-J. Chen, Y.-F. Lyu, and S.-L. Chen, "High-performance germanium-on-silicon lock-in pixels for indirect time-of-flight applications," in *2018 IEEE International Electron Devices Meeting (IEDM)*, San Francisco, CA, USA (IEEE, 2018), pp. 32.4.1–32.4.4.
[291]M. Wanitzek, M. Oehme, D. Schwarz, K. Guguieva, and J. Schulze, "Ge-on-Si avalanche photodiodes for LIDAR applications," in *2020 43rd International Convention on Information, Communication and Electronic Technology (MIPRO)*, Opatija, Croatia (IEEE, 2020), pp. 8–12.
[292]S. Guerber, D. Fowler, I. Charlet, P. Grosse, K. Abdoul-Carime, J. Faugier-Tovar, and B. Szelag, "Development, calibration and characterization of silicon photonics based optical phased arrays," Proc. SPIE **11690**, 1169006 (2021).
[293]C.-P. Hsu, B. Li, B. Solano-Rivas, A. R. Gohil, P. H. Chan, A. D. Moore, and V. Donzella, "A review and perspective on optical phased array for automotive LiDAR," IEEE J. Sel. Top. Quantum Electron. **27**, 1 (2021).
[294]Y. Li, B. Chen, Q. Na, Q. Xie, M. Tao, L. Zhang, Z. Zhi, Y. Li, X. Liu, X. Luo, and G. Lo, "Wide steering-angle high-resolution optical phased array," Photonics Res. **9**, 2511–3518 (2021).
[295]X. Cao, G. Qiu, K. Wu, C. Li, and J. Chen, "Lidar system based on lens assisted integrated beam steering," Opt. Lett. **45**, 5816–5819 (2020).
[296]S. J. Spector, "Review of lens-assisted beam steering methods," J. Opt. Microsyst. **2**, 011003 (2022).
[297]Y. Wang, G. Zhou, X. Zhang, K. Kwon, P.-A. Blanche, N. Triesault, K.-s. Yu, and M. C. Wu, "2D broadband beamsteering with large-scale MEMS optical phased array," Optica **6**, 557–562 (2019).
[298]S. Chung, H. Abediasl, and H. Hashemi, "A monolithically integrated large-scale optical phased array in silicon-on-insulator CMOS," IEEE J. Solid-State Circuits **53**, 275–296 (2018).
[299]S. A. Miller, Y.-C. Chang, C. T. Phare, M. C. Shin, M. Zadka, S. P. Roberts, B. Stern, X. Ji, A. Mohanty, O. A. Jimenez Gordillo, U. D. Dave, and M. Lipson, "Large-scale optical phased array using a low-power multi-pass silicon photonic platform," Optica **7**, 3–6 (2020).
[300]H. Qiu, Y. Liu, X. Meng, X. Guan, Y. Ding, and H. Hu, "Energy-efficient integrated silicon optical phased array," Front. Optoelectron. **16**, 23 (2023).
[301]Z. Li, Y. Han, L. Wu, Z. Zang, M. Dai, S. Y. Set, S. Yamashita, Q. Li, and H. Y. Fu, "Towards an ultrafast 3D imaging scanning LiDAR system: A review," Photonics Res. **12**, 1709–1729 (2024).
[302]J. H. Chang, S. H. Bae, H. Kim, C. H. Ouh, C. H. Jung, H. S. Cho, and Y. C. Chung, "Space-efficient fiber ribbon composed of reduced-cladding single-mode fibers," Opt. Fiber Technol. **31**, 178–183 (2016).
[303]S. Yu, L. Ranno, Q. Du, S. Serna, C. McDonough, N. Fahrenkopf, T. Gu, and J. Hu, "Free-form micro-optics enabling ultra-broadband low-loss off-chip coupling," Laser Photonics Rev. **17**, 2200025 (2023).
[304]A. Liu, P. Wolf, J. A. Lott, and D. Bimberg, "Vertical-cavity surface-emitting lasers for data communication and sensing," Photonics Res. **7**, 121–136 (2019).
[305]J. W. Elliott, M. T. Lebon, and A. J. Robinson, "Optimising integrated heat spreaders with distributed heat transfer coefficients: A case study for CPU cooling," Case Stud. Therm. Eng. **38**, 102354 (2022).
[306]J. Ma, D. S. Robledo, L. Anzagira, D. Zhang, K. Shahverdi, and S. Masoodian, "A 1.26-inch 40.7 mega-pixel photon-counting quanta image sensor with 0.35e^- read noise and 95 dB single-exposure dynamic range," in *Imaging and Applied Optics Congress 2022 (3D, AOA, COSI, ISA, pcAOP), Technical Digest Series* (Optica Publishing Group, 2022), p. JW5B.4.
[307]X. Yue and E. R. Fossum, "Design and characterization of a burst mode 20 Mfps low noise CMOS image sensor," Sensors **23**, 6356 (2023).
[308]A. Dhakal, P. C. Wuytens, F. Peyskens, K. Jans, N. L. Thomas, and R. Baets, "Nanophotonic waveguide enhanced Raman spectroscopy of biological submonolayers," ACS Photonics **3**, 2141–2149 (2016).
[309]M. Mahmud-Ul-Hasan, P. Neutens, R. Vos, L. Lagae, and P. Van Dorpe, "Suppression of bulk fluorescence noise by combining waveguide-based near-field excitation and collection," ACS Photonics **4**, 495–500 (2017).
[310]N. Saha, G. Brunetti, A. di Toma, M. N. Armenise, and C. Ciminelli, "Silicon photonic filters: A pathway from basics to applications," Adv. Photonics Res. **5**, 2300343 (2024).
[311]M. R. Bryan, J. N. Butt, J. Bucukovski, and B. L. Miller, "Biosensing with silicon nitride microring resonators integrated with an on-chip filter bank spectrometer," ACS Sens. **8**, 739–747 (2023).

[312]A. V. Krishnamoorthy, "QD lasers: A step toward easier integration with PICs," in *2025 Integrated Photonics Systems Roadmap (IPSR) Meeting*, Cambridge, MA, *6 June 2025* (Microphotonics Center, Massachusetts Institute of Technology, 2025).
[313]See https://photonicsmanufacturing.org/sites/default/files/documents/2024_ipsr-i_silicon_photonics_updated_v2.pdf for information about "2024 Integrated Photonics Systems Roadmap International (IPSR-I) Silicon Photonics" (accessed June 2025).
[314]S. M. Koepfli, M. Baumann, S. Giger, K. Keller, Y. Horst, Y. Salamin, Y. Fedoryshyn, and J. Leuthold, "High-speed graphene photodetection: 300 GHz is not the limit," in *2021 Conference on Lasers and Electro-Optics Europe & European Quantum Electronics Conference (CLEO/Europe-EQEC)*, Munich, Germany (IEEE, 2021), p. 1.
[315]C. Han, Z. Zheng, H. Shu, M. Jin, J. Qin, R. Chen, Y. Tao, B. Shen, B. Bai, F. Yang, Y. Wang, H. Wang, F. Wang, Z. Zhang, S. Yu, C. Peng, and X. Wang, "Slow-light silicon modulator with 110-GHz bandwidth," Sci. Adv. **9**, eadi5339 (2023).
[316]Y. Horst, D. Moor, D. Chelladurai, T. Blatter, S. Fernandes, L. Kulmer, M. Baumann, H. Ibili, C. Funck, K. Keller, M. Destraz, W. Heni, L. Chérix, Y. Liu, H. Wang, S. M. Koepfli, and J. Leuthold, "Ultra-wideband MHz to THz plasmonic EO modulator," Optica **12**, 325–328 (2025).
[317]S. Wu, L. Zhang, R. Wan, H. Zhou, K. H. Lee, Q. Chen, Y.-C. Huang, X. Gong, and C. S. Tan, "$Ge_{0.92}Sn_{0.08}$/Ge multi-quantum-well LEDs operated at 2-μm-wavelength on a 12-inch Si substrate," Photonics Res. **11**, 1606–1612 (2023).